HyperCEST MR Studies of Xenon-129 (^{129}Xe) Biosensors and MRI Detection of ^{129}Xe in the Brain

By Alanna Wade

A thesis submitted in partial fulfillment of the requirements for the degree of

Master of Science in Chemistry

Faculty of Science and Environmental Studies

Department of Chemistry

Lakehead University

April 2019

“The good thing about science is that it's true whether or not you believe in it”.

- Neil deGrasse Tyson

ACKNOWLEDGEMENTS

I would like to thank Dr. Mitchell Albert and Dr. Francis Hane for their mentorship throughout my master's degree program.

I would like to thank my internal thesis committee member, Dr. Alla Reznik and Dr. Stephen Kinrade, for reviewing my thesis.

I would like to thank my external examiner, Dr. Boyd Goodson, for also reviewing my thesis.

I would like to thank Tao Li and Yurii Shepelytskyi for their assistance with the MRI experiments.

I would like to thank Dr. Brenton DeBoef and Ashvin Fernando for synthesizing the ^{129}Xe host molecules and the benzene-appended CB[6] that pertain to chapter 3 and Appendix A.

I would like to thank Dr. Alderson and Trista King for their assistance with animal surgeries and animal utilization protocols.

I would like to thank Dr. Lawrence-Dewar for her assistance with the fMRI data analysis.

I would like to thank TBRHRI for letting me use their MRI facilities and third floor lab.

I would also like to thank my stress ball, which handled my squeezing very well.

TABLE OF CONTENTS

List of Figures

List of Abbreviations

ATP	adenosine triphosphate
BOLD	blood-oxygenated level dependent
CB[6]	cucurbit[6]uril
Cr-A	cryptophane-A
DNP	Dynamic nuclear polarization
DMSO	dimethyl sulfoxide
EGFR	epidermal growth factor receptor
FA	flip angle
FFE	fast field echo
FID	free induction decay
fMRI	functional Magnetic Resonance Imaging
FOV	Field of View
HP	hyperpolarized
Hz	hertz
HyperCEST	Hyperpolarized Xenon Chemical Exchange Saturation Transfer
IV	intravenous
MRI	Magnetic Resonance Imaging
NMR	Nuclear Magnetic Resonance
NSCLC	Non-small cell lung cancer
PBS	phosphate buffer solution
PET	Positron Emission Tomography
ppm	parts per million
RF	Radiofrequency
SNR	Signal-to-Noise Ratio
TE	Echo time

List of Abbreviations (cont'd)

TR	Repetition Time
T1 relaxation	spin-lattice relaxation
T2 relaxation	spin-spin relaxation

List of Symbols

^{1}H	hydrogen-1
^{13}C	carbon-13
^{19}F	fluorine-19
^{129}Xe	xenon-129
Rb	rubidium
γ	gyromagnetic ratio
ms	millisecond
s	second
α-CD	alpha-cyclodextrin
β-CD	beta-cyclodextrin
γ-CD	gamma-cyclodextrin
5-C bar	5-carbon alkyl chain
8-C bar	8-carbon alkyl chain
10-C bar	10-carbon alkyl chain
T	tesla
Å	angstrom
mL	millilitre
L	litre
1-D	one dimension
2-D	two dimensions
3-D	three dimensions

1. Literature Review

The research work presented in this thesis involves ^{129}Xe biosensors, hyperpolarized chemical exchange saturation transfer (HyperCEST), and HP ^{129}Xe fMRI. In order to facilitate the discussion of this research work, it is important to review the concepts of NMR and MRI.

1.1 Nuclear Magnetic Resonance

MRI is based on the principles of NMR. Therefore, this section explains the concepts in NMR, such as nuclear magnetic moments, magnetization of nuclei, magnetic dipole moments in an external magnetic field, along with T1 and T2 relaxation.

1.1.1 Nuclear Magnetic Moment

NMR is based on the principle that nuclei with a non-zero quantum number experience spin angular momentum, as governed by:

$$J = \hbar I \tag{1.1}$$

where I is a spin-quantum number and $\hbar$ is the reduced Planck's constant. Because of this spin angular momentum, the nucleus acts like a spinning charged particle resulting in a magnetic moment. This phenomenon is governed by the following equation:

$$\vec{\mu} = \gamma \vec{J}, \tag{1.2}$$

where γ is the gyromagnetic ratio which is unique to each nucleus.[1]

1.1.2 Magnetization of Nuclei

Magnetization refers to the alignment of nuclei's magnetic moments in an external magnetic field. In the absence of an external magnetic field, there is no net magnetization since there is random arrangement of the nuclei's magnetic dipole moments.[1] Conversely, when nuclei are placed in an external magnetic field, magnetic moments with a positive gyromagnetic ratio

generally align in the same direction as the external magnetic field, leading to a net magnetization:

$$\vec{M} = \lim_{\Delta V \to 0} \frac{\Sigma_i \, \vec{\mu}_i}{\Delta V}, \qquad (1.3)$$

where ΔV is a given volume of sample. Based on equation *(1.3)*, a net sum of magnetic moments is aligned in the same direction as the external magnetic field. In this manner, there is a net magnetization vector that points in the same direction as the external magnetic field, B_0, as shown in figure 1.1.

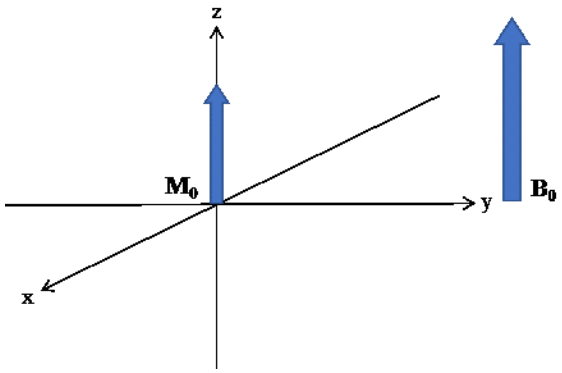

Figure 1.1: The net magnetization of nuclei is aligned in the same direction as the external magnetic field, B_0.

The above situation describes magnetization in the context of classical mechanics. In quantum mechanics, nuclei are split into "lower" and "upper" energy levels within an external magnetic field. This phenomenon results in a population difference between two energy levels. The magnetic moment of each nucleus possesses a potential energy, which is expressed as:

$$E = -\vec{\mu} \overrightarrow{B_0}. \qquad (1.4)$$

To account for the gyromagnetic ratio and spin, I, equation *(1.4)* can be rewritten as:

$$E = -\gamma \, \hbar \, I \, B_0. \qquad (1.5)$$

For nuclei with spin ½ quantum number, nuclei either have a "spin-up" or "spin-down" position, and therefore the nuclei's spin value is either I = + ½ or I = -½. In this manner, the nuclei with I = ½ and I = -½, respectively, have an energy state of

$$E_- = -\frac{\gamma\hbar B_0}{2} \text{ and } E_+ = \frac{\gamma\hbar B_0}{2}. \quad (1.6)^{2}$$

As a result, the potential energy difference between the two energy states, E_+ and E_-, is defined as

$$\Delta E = \hbar\gamma B_0 = \hbar\omega_0, \quad (1.7)^{2}$$

where the lower and higher energy states respectively are populated by magnetic dipole moments that align with and against the external magnetic field. This effect is known as Zeeman splitting.

Slightly more nuclei populate the E_- than an E_+ energy state; therefore, slightly more nuclei possess a + ½ spin state than a -½ spin state (at thermal equilibrium). In this manner, this situation results in a net polarization, which is expressed as:[3]

$$P = \frac{N_+ - N_-}{N_+ + N_-}, \quad (1.8)$$

where N_+ and N_-, respectively, are the number of spins in the lower and upper energy states. Additionally, the Boltzmann distribution, $e^{-E/kT}$, can quantify the probability that a nucleus has a spin +½ quantum number. Therefore, equation *(1.8)* can be rewritten as:

$$P = \frac{e^{\gamma B_0/kT} - e^{-\gamma B_0/kT}}{e^{\gamma B_0/kT} + e^{-\gamma B_0/kT}}, \quad (1.9)$$

where T is the absolute temperature and k is the Boltzmann constant. In the absence of an external magnetic field, there is degeneracy between the two energy states, resulting in no net magnetization and polarization. On the other hand, at a magnetic field strength of 3 T and a temperature at approximately 36 °C, the polarization for ^{1}H nuclei is approximately 9.9 x 10^{-6}, which is low. However, the human body is composed of approximately 70 percent water, which provides a sufficient number of ^{1}H nuclei to conduct proton MR imaging.

1.1.3 Magnetic Moments in an External Magnetic Field

As discussed in section 1.1.2, the magnetic moments are generally aligned in the same direction as the external magnetic field, B_0, at thermal equilibrium. Furthermore, magnetic moments are subjected to torque when placed in an external magnetic field, as governed by[2]

$$\vec{\tau} = \vec{\mu} \times \overrightarrow{B_0}. \tag{1.10}$$

Equation *(1.10)* can be re-written to account for the time derivation of angular momentum, which is equal to torque:

$$\frac{d}{dt}\vec{J} = \vec{\mu} \times \overrightarrow{B_0}. \tag{1.11}$$

When equation *(1.2)* is substituted into equation *(1.11),* then *(1.11)* becomes

$$\frac{d}{dt}\vec{\mu} = \vec{\mu} \times \gamma\overrightarrow{B_0}, \tag{1.12}$$

Thus, equation *(1.12)* shows a correlation between γ and a nucleus' magnetic moment within an external magnetic field.

To account for the ensemble of magnetic moments aligned in the same direction as the external magnetic field, $\vec{\mu}$ in equation *(1.12)* can be replaced by $\vec{M}$:

$$\frac{d}{dt}\vec{M} = \vec{M} \times \gamma\overrightarrow{B_0}. \tag{1.13}$$

If the direction of B_0 is assigned to the z-direction, then equation *(1.13)* can be solved as

$$M_{xy} = (M_0 \sin\theta)\, e^{-i\omega_0 t},\ M_z = M_0 \cos\theta, \tag{1.14}$$

where M_{xy} is a precessional vector in the transverse (xy) plane, M_z is the magnetization component in the positive z-direction, and θ is the polar angle. Based on equation *(1.14)*, the precessional frequency for the net magnetization vector is equal to ω_0, which is also known as the Larmor frequency.

Attaining an NMR signal requires the application of a radio frequency (RF) pulse to a sample already placed an external, magnetic field. During the application of a 90° RF pulse, there is a time-varying magnetic field, indicated as $\overrightarrow{B_1}$, whose direction is perpendicular to the external magnetic field B_0. Therefore, $\overrightarrow{B_1}$ can be assigned as a rotating vector within the xy plane:

$$B_{xy} = \left|\overrightarrow{B_1}\right| \cdot e^{-i\omega t}, \tag{1.15}$$

where ω is the carrier frequency (in rad/s) of the RF pulse. Since $\overrightarrow{B_1}$ is interpreted as a rotating vector, then this system can be simplified where, within a rotating frame, $\overrightarrow{B_1}$ is rotating about the z-direction at the Larmour frequency (see figure 1.2 for a schematic of this rotating reference frame). As a result, we attain an applied field within this rotating reference frame, which is governed by the following expression:

$$\vec{B}_{app} = B_1\hat{\imath} + (B_0 - \frac{\omega}{\gamma})\hat{k}. \tag{1.16}$$

In this manner, the longitudinal component of magnetization appears reduced, and the B_1 field appears to be stationary in the x-direction. Assuming that the RF pulse is rotating exactly at the Larmor frequency, then equation *(1.16)* can be simplified as

$$B_1\hat{\imath} = B_1\hat{\imath} + \left(B_0 - \frac{\omega_0}{\gamma}\right)\hat{k} = \vec{B}_{app}\,. \tag{1.17}$$

It is also feasible to modify equation *(1.13)* to account for the precessional behaviour of the net magnetization vector in a magnetic field $\vec{B}_{app}$:

$$\frac{d}{dt}M = M \times \gamma B_{app} = M \times \gamma B_{app}\hat{\imath}, \tag{1.18}$$

where its solution is

$$\omega_1 = \gamma B_1. \tag{1.19}$$

Equation *(1.19)* shows that a net magnetization vector precesses at a frequency ω_1 in a magnetic field, B_1.

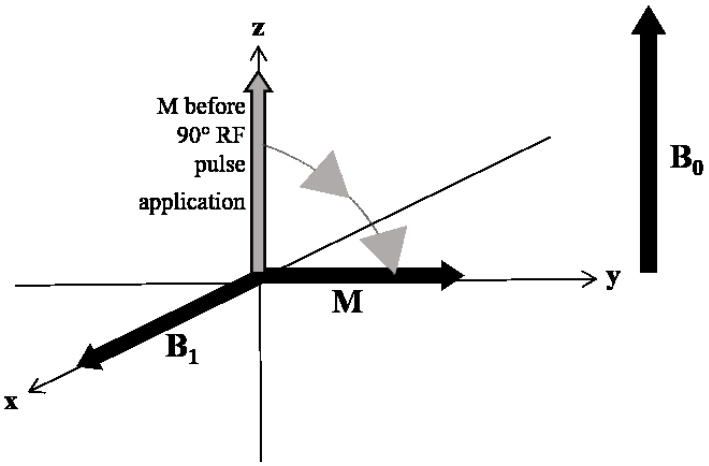

Figure 1.2: Schematic that shows the rotating reference frame after the execution of a 90° RF pulse.

Additionally, a flip angle is the angle between the net magnetization vector and the z-direction upon termination of the RF pulse. In this manner, the flip angle is equal to the integral of equation *(1.19)* (with respect to time):

$$\theta_1 = \int_0^\tau |\omega_1| dt = \gamma \int_0^\tau B_1(t) dt. \qquad (1.20)$$

Upon application of an RF pulse with a flip angle θ in an external magnetic field, the magnitudes for the transverse and longitudinal components of magnetization, respectively, are

$$M_{xy} = M_0 \sin\theta \text{ and } M_z = M_0 \cos\theta. \qquad (1.21)$$

According to equations *(1.21)*, an RF pulse that induces a 90° flip angle produces the highest NMR signal for both the longitudinal and transverse components of magnetization.

After the termination of the RF pulse, the net magnetization vector continues to rotate at the Larmor frequency within the static, external, magnetic field, B_0. After the termination of an RF pulse, transverse magnetization also produces an electromotive force (EMF), which generates

a current in a coil, called an RF coil, placed perpendicular to the external magnetic field B_0. The EMF produced in the RF coil is governed by Faraday's law:

$$S(t) = -\frac{d}{dt}\Phi(t) = -\int_{V_i}^{V_f} dV \left(\frac{d}{dt}\vec{M}(\vec{u},t)\right) \cdot \overrightarrow{B_1}(\vec{u}). \quad (1.22)$$

In this manner, the $\vec{M}(\vec{u},t)$ is the magnitude of magnetization within the transverse plane at a position $\vec{u}$; $\overrightarrow{B_1}(\vec{u})$ is the applied magnetic field produced by an RF pulse at a position $\vec{u}$ per unit current; V_s is the volume of a sample; and $S(t)$ is the signal received by the RF coil in units of volts. $\vec{M}(\vec{u},t)$ is also a precessing vector in the form of $\vec{M}(\vec{u}) \cdot e^{-i\omega_0 t}$; therefore, equation *(1.22)* can be rewritten as

$$S(t) = i\omega_0 e^{-i\omega_0 t} \int_{V_i}^{V_f} dV \cdot \vec{M}(\vec{u}) \cdot \overrightarrow{B_1}\vec{u}, \quad (1.23)$$

which does not include the time derivative. Upon termination of the RF pulse, there is regrowth of the longitudinal component of magnetization (T1 relaxation), and there is decay of the transverse component of magnetization (T2 relaxation).

1.1.4 T1 relaxation

T1 relaxation, also known as "spin-lattice" relaxation, refers to the time constant that governs the nuclear spins to return to their thermal equilibrium. The application of an RF pulse stimulates the nuclei to transition between the E_+ and E_- energy states. T1 relaxation is the interaction of nuclear spins with random, magnetic field fluctuations within the lattice, whose frequency is close to ω_0. Eventually, the magnetic moments return to their lowest energy state and thermal equilibrium. The following differential equation demonstrates this T1 relaxation process:

$$\frac{d}{dt} M_z = -\frac{(M_z - M_0)}{T1}, \quad (1.24)$$

where M_0 is the magnetization at thermal equilibrium, M_z is the magnetization of the longitudinal component, and *T1* is the longitudinal relaxation time. The solution for equation *(1.24)* is

$$M_z(t) = M(0)e^{-\frac{t}{T1}} + M(0)(1 - e^{-\frac{t}{T1}}), \qquad (1.25)$$

where *t* is time in seconds and *M(0)* represents the longitudinal magnetization when t = 0. Upon application of a 90° RF pulse, *M(0)* is assumed to be 0. As a result, the magnitude of longitudinal magnetization (and re-growth of thermal equilibrium) can be determined via

$$M_z(t) = M_0(1 - e^{-\frac{t}{T1}}). \qquad (1.26)$$

According to equation *(1.26)*, at a given time (*t*), a long *T1* relaxation value results in slower recovery in longitudinal magnetization ($M_z(t)$) compared to that with a short *T1* relaxation value. Figure 1.3 demonstrates the inverse correlation between the *T1* value and the rate of recovery in longitudinal magnetization. It is also feasible make the signal expression of equation *(1.23)* account for effects of *T1*:

$$S(t) = i\omega_0 e^{-i\omega_0 t} \int_{V_i}^{V_f} dV \cdot \vec{M}(\vec{u}) \cdot \left(1 - e^{-\frac{t}{T1\ (\vec{u})}}\right) \qquad (1.27)$$

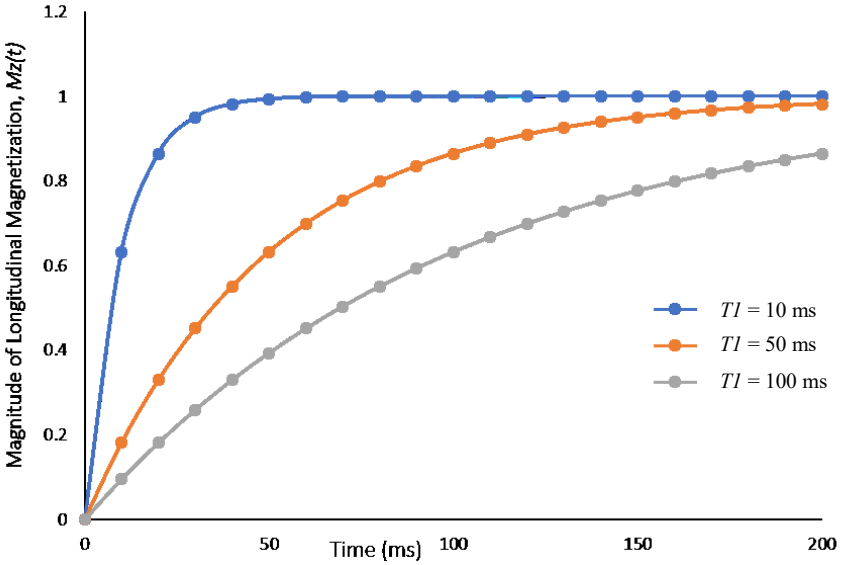

Figure 1.3: Schematic showing T1 relaxation curves for three different T1 values. The curve for the highest T1 value, 100 ms, has the slowest recovery in its longitudinal magnetization.

1.1.5 T_2 relaxation

T_2 relaxation refers to the gradual loss of magnetization within the transverse plane in an external magnetic field. T_2 relaxation involves spin-spin interaction, where a change in the magnetic field produced by one spin affects the motion of neighboring spins. T_2 relaxation can be expressed by the following differential equation:

$$\frac{d}{dt} M_{xy} = -\frac{M_{xy}}{T_2}, \tag{1.28}$$

where T_2 is the transverse relaxation time constant and M_{xy} is the transverse component of magnetization. The solution for equation *(1.28)* is

$$M_{xy}(t) = M_0 e^{-t/T_2}, \tag{1.29}[1]$$

where M_0 is the initial magnetization in the transverse plane after the application of a 90° RF pulse.

T_2^* is the apparent transverse relaxation, which accounts for both spin-spin interaction and external magnetic field inhomogeneities that cause the magnetic moments to dephase within the transverse plane. The following equation demonstrates T_2^*:

$$\frac{1}{T_2^*} = \frac{1}{T_2} + \gamma \Delta B, \tag{1.30}[1]$$

where T_2 is the transverse relaxation resulting from spin-spin interactions, and $\gamma \Delta B$ accounts for inhomogeneities in the external magnetic field. According to equation *(1.30)*, T_2^* is shorter than T_2. Figure 1.4 demonstrates the difference between T_2 and T_2*. Equation *(1.23)* can be modified to account for T_2^* effects:

$$S(t) = i\omega_0 e^{-i\omega_0 t} \int_{V_i}^{V_f} dV \cdot \vec{M}(\vec{u}) \cdot \left(1 - e^{-\frac{t}{T_1(\vec{u})}}\right) \cdot e^{-\frac{t}{T_2^*(\vec{u})}} \tag{1.31}$$

7

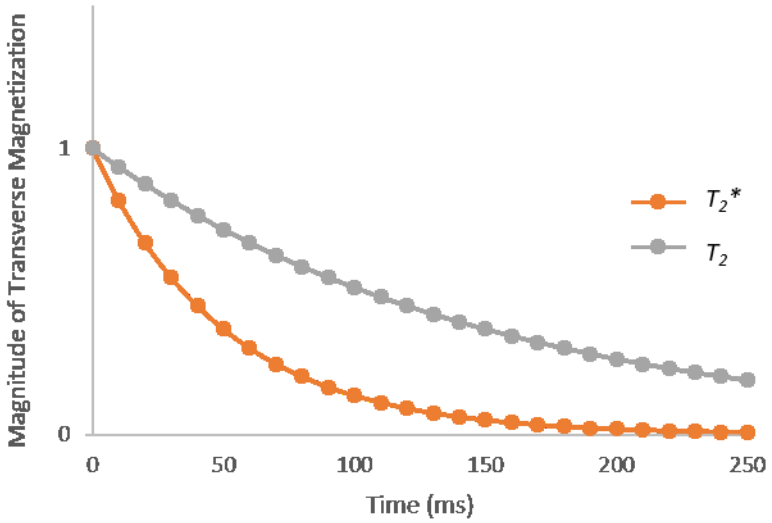

Figure 1.4: Schematic showing T_2 and T_2 relaxation curves. There is faster decay in transverse magnetization signal for T_2* relaxation that that of T_2 relaxation.*

1.2 Magnetic Resonance Imaging

The transition from NMR to MRI involves localization of signal exhibited by the net magnetization vector in 1-, 2-, or 3-D. To facilitate this transition, it is important to spatially localize this signal using slice select, phase encoding, and frequency encoding gradients.

1.2.1 Spatial Localization

To attain an MR image, it is important to spatially localize the received signal by using linear magnetic field gradients and B_0. The net magnetization is aligned in the same direction as the external magnetic field. There is also variation in spatial frequency in the x-, y-, and z-directions because of applied gradients. As a result, the applied magnetic field is governed by

$$\vec{B}(x,y,z) = B_0\hat{k} + (G_x x + G_y y + G_z z)\hat{k}, \qquad (1.32)$$

where $G_x = \frac{dB_0}{dx}$, $G_y = \frac{dB_0}{dy}$, and $G_z = \frac{dB_0}{dz}$. The magnetic field gradients can be a function of position, $\vec{u}$. There is also time variation with the magnetic field gradients. It is feasible to combine the magnetic field gradients into a single vector, as shown by the following equation:

$$\vec{G}(\vec{u},t) = \frac{d}{dx}B_0(t)\vec{\imath} + \frac{d}{dy}B_0(t)\vec{\jmath} + \frac{d}{dz}B_0(t)\vec{k}, \quad (1.33)$$

where $\vec{\imath}$, $\vec{\jmath}$, and $\vec{k}$, respectively, are vectors that represent spatial frequencies in the x-, y-, and z-directions.

When a magnetic field gradient is turned on, the precessional frequencies for all spins in an external magnetic field become inhomogenous. Each spin also acquires an additional linear phase. In this manner, the precessing vector for a spin is $\vec{M}(\vec{u}) \cdot e^{-i\omega_0 t} \cdot e^{-i\Delta(\vec{u},t)}$. Therefore, equation *(1.22)* can be modified to become:

$$S(t) = i\omega_0 e^{-i\omega_0 t} \int_{V_i}^{V_f} dV \cdot \overrightarrow{M_0} \cdot \left(1 - e^{-\frac{t}{T_1(\vec{u})}}\right) \cdot e^{-\frac{t}{T_2^*(\vec{u})}} \cdot B_1(\vec{u}) \cdot e^{-i\Delta\varphi(\vec{u},t)}. \quad (1.34)$$

which also accounts for effects of *T1* and T_2^* relaxation on a signal in MRI.
Furthermore, the phase accumulated during the application of a magnetic field gradient is defined as:

$$\Delta\varphi(\vec{u},t) = \int_0^t dt \cdot \gamma \cdot G(u,t) \cdot u. \quad (1.35)$$

Equation *(1.35)* can be simplified to become:

$$k = \frac{\gamma}{2\pi}\int_0^t dt' \cdot \vec{G}(t'), \text{ where } \Delta\varphi(\vec{u},t) = 2\pi(\vec{k},\vec{u}), \quad (1.36)$$

which introduces the concept of k-space. In general, k-space is a matrix of spatial frequencies for an object in 2D or 3D. The position of a magnetization vector in k-space is determined by the phase accumulated during the application of magnetic field gradients, as governed by equation *(1.36)*.

Spatial localization is important for the recovery of magnetization density, which is moderated by relaxation, B1 field of the RF coil, and a linear phase factor corresponding to the frequency of magnetic moments.

Consider the following equation that expresses magnetization density, which involves relaxation, B_1, and phase effects:

$$\widehat{M}(\vec{u}) = i\omega_0 e^{-i\omega_0 t} \cdot \vec{M}(\vec{u}) \cdot \left(1 - e^{-\frac{t}{T_1(u)}}\right) \cdot e^{-\frac{t}{T_2^*(u)}} \cdot \vec{B}_1(\vec{u}). \quad (1.37)$$

When equations *(1.36)* and *(1.37)* are incorporated into equation *(1.34)*, then we attain

$$S(\vec{k}) = \int_{V_i}^{V_f} dV \cdot \widehat{M}(\vec{u}) \cdot e^{-i2\pi(\vec{k}\cdot\vec{u})}, \quad (1.38)$$

which means that the received MRI signal becomes integrated into image space and becomes a function of position in k-space. After the application of an MRI pulse sequence, an inverse Fourier transform can be used to recover the effective magnetization density:

$$\widehat{M}(\vec{r}) = \int_k dk \cdot S(\vec{k}) \cdot e^{i2\pi(\vec{k}\cdot\vec{u})}, \quad (1.39)$$

where the effective magnetization density gets integrated over image space and becomes a function of position in k-space.

1.2.2 Slice Select Gradient

To excite the magnetization vectors in a 2D slice, both the RF pulse and a slice select gradient need to be simultaneously turned on. In this manner, the slice select gradient further localizes the signal of magnetization within a 2D slice. MR imaging can be conducted in the coronal, axial, or sagittal planes. Both the slice select gradient and the external magnetic field, B_0, are arbitrarily assigned to the z-axis within a given frame of reference.

The following equation can be used to determine the thickness of a 2D slice:

$$\Delta z = \frac{BW_{rf}}{\frac{\gamma}{2\pi} G_z}, \quad (1.40)$$

where Δz is the slice thickness of a 2D slice, G_z is the slice select gradient, and BW_{rf} is the bandwidth of the RF pulse. Bandwidth is a range of frequencies.[1] Equation *(1.40)* shows a direct

correlation between BW_{rf} and Δz, where a narrow bandwidth results in narrow slice thickness.

1.2.3 Phase Encoding Gradient

Once the slice select gradient is turned off, the phase encoding gradient is applied in a direction perpendicular to the external magnetic field, B_0. In this manner, the magnetic moments precess at a frequency with respect to the y-direction of the frame of reference, which is $\omega_y = \gamma B_y$. When the phase encoding gradient is turned off, the magnetic moments return to the same precessional frequency that they possessed before the phase encoding gradient was turned on. However, they retain the phase that was accumulated during the application of the phase encoding gradient. As a result, the accumulated phase for magnetic moments varies in the y-direction of k-space. Once the phase encoding gradient is turned off, then the position in k-space for a given magnetic moment is governed by the following equation:

$$k_y = \frac{\gamma}{2\pi} D_{PE} \cdot G_y, \qquad (1.41)$$

where D_{pe} is the duration of the phase encoding gradient.

1.2.4 Frequency Encoding Gradient

After the application of a phase encoding gradient, the frequency encoding gradient is applied in the x-direction with respect to the frame of reference. Similar to the phenomenon that pertains to the phase encoding gradient, the magnetic moments precess at a frequency $\omega_x = \gamma B_x$ while the frequency encoding gradient is turned on. When it is turned off, the magnetic moments maintain the phase that was acquired during the application of the frequency encoding gradient. Since the frequency encoding gradient is usually turned on after the application of a phase encoding gradient, phase accumulation for magnetic moments varies in both the x- and y-directions of k-space.

During the application of a frequency encoding gradient, data are acquired from the free induction decay (FID), which is the rapid depletion of an MRI signal that appears after the execution of an RF pulse. The time it takes to acquire these data is referred to as the sampling time. Then, these data undergo Fourier transformation to form an image.

1.2.5 T1- and T2-Weighted MRI

The two most common imaging techniques are T1- and T2-Weighted MRI, which are, respectively, based on *T1* and T_2 relaxation mechanisms. T1-weighting is obtained when the repetition period of RF pulses, *TR*, is of the same order as the longitudinal relaxation time.[4] In particular, T1-weighting MRI involves a short repetition time (*TR*) and short echo time (TE) to attain the greatest contrast among tissues with different *T1* relaxation times.[1] In steady-state, the local magnetization is reduced from its thermal equilibrium value, M_{eq}, according to the following equation:[4]

$$M = M_{eq}\frac{1-exp(-\frac{TR}{T_1})}{1-cos\theta exp(-\frac{TR}{T_1})} \qquad (1.42)$$

where θ is the flip angle of the RF pulse. For an appropriate choice of θ and *TR*, tissues with a short *T1* have rapid recovery of longitudinal magnetization, and therefore provide a stronger signal and appear more intense in images than tissues with a long *T1*, whose longitudinal magnetization recovery is relatively long.[4] T2-weighted imaging is obtained via long *TR* with a long *TE* to differentiate tissues based on T_2 relaxation. In T2-weighted MRI, tissues with a long T_2 relaxation time appear brighter than tissues with a short T_2 relaxation time. In steady-state, the magnetization for T_2 relaxation undergoes re-growth until it reaches thermal equilibrium, as governed by the following equation:

$$M_{eq} = M \frac{e^{-\frac{TR}{T_2}}}{\sin\theta e^{-\frac{TR}{T_2}}}, \qquad (1.43)$$

where T_2 is the spin-spin relaxation time. Based on equation *(1.43)*, tissues with a long T_2 yield a stronger signal than tissues with a short T_2.

Figure 1.5 shows T2-weighted and T1-weighted MR brain images. For the T2-weighted MR image, water-containing tissues, such as cerebrospinal fluid appear bright while lipid-containing tissues, such as white matter, appear dark. On the other hand, the cerebrospinal fluid appears dark and lipid-containing issues appear bright for the T1-weighted MR image.[5]

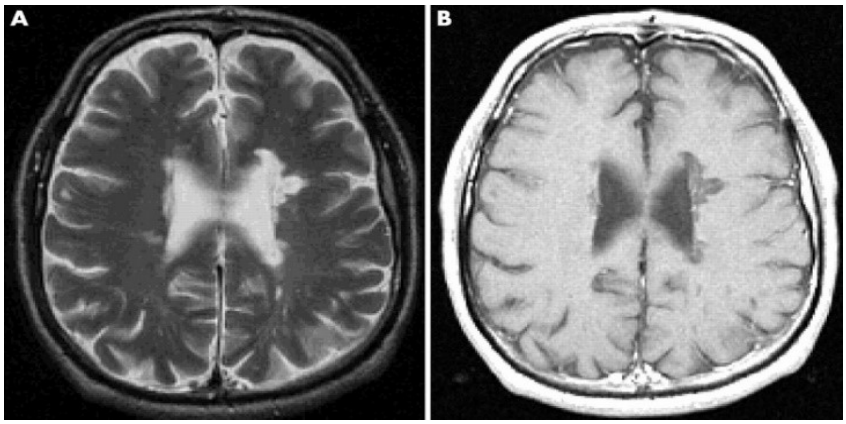

Figure 1.5: (A) T2-weighted and (B) T1-weighted axial brain MR images. Cerebrospinal fluid (CSF) has a longer T_2 relaxation time than brain tissue. Therefore, for a T2-weighted MR image (panel (A)), CSF appears bright while brain tissue appears dark. CSF has a shorter T1 relaxation time than brain tissue. Hence, for T1-weighted MRI (panel (B)), CSF appears darks while brain tissue appears bright. Images were taken with permission from ref. 5.

1.2.6 Functional Magnetic Resonance Imaging

One widely used MR imaging modality for the brain is functional magnetic resonance imaging (fMRI). It is a non-invasive technique that can localize areas of brain function.[6] fMRI uses the blood-oxygen level dependent (BOLD) mechanism, where signal changes within the brain are induced by changes in hemodynamic and metabolic processes occurring at neuronal

activation sites.[6] In particular, neural activity requires energy in the form of ATP, which is produced via oxidative glycosylation.[7] When a certain brain region is activated, it requires increased energy input, which results in upregulation of oxygen.[7] Oxygen is carried to the activated brain region in the form of oxygen-bound hemoglobin, which means there is a surge in the amount of oxygen-bound hemoglobin within that activated brain region.[7] The up-surge in blood flow and oxygen-bound hemoglobin within an activated brain region results in differential T_2 contrast.[8] Additionally, Ogawa *et al*. showed that a strong MRI signal was associated with areas of high concentrations of oxyhemoglobin compared to areas of high concentrations of deoxyhemoglobin,[8] mainly because oxyhemoglobin is diamagnetic while deoxyhemoglobin is paramagnetic.[9] The functional images can be overlaid with a high resolution proton MR image to determine which regions within the brain experienced higher metabolic activity via hemodynamic processes.[8]

1.3 Hyperpolarized Noble Gas MRI

Sections 1.1 and 1.2, respectively, describe NMR and MRI in the context of a ^{1}H nucleus. Although ^{1}H MRI can produce various images inside the human body, it is limited in providing anatomical and functional information for the lungs. It is limited because normal lung parenchyma have one-fifth the proton density of muscle tissue,[10] which reduces signal intensity within the lungs. Additionally, the protons in the lungs have a short transverse relaxation time because of the air-tissue interface,[4] which causes the lungs to be subjected to large magnetic susceptibility.[11] The strong magnetic field gradients applied in a 1.5 T field also rapidly dephase the Larmour frequency of protons within the lungs.[4] The use of noble gases, however, can circumvent the limitations with ^{1}H MR lung imaging. Conversely, the polarization level for thermally polarized noble gas nuclei with spin ½ quantum number is usually between 10^{-6} and

10^{-4}.[12] They also exist at low concentration at standard temperature and pressure. Therefore, because of their low polarization level and low concentration, their signal remain undetectable in NMR and MRI. To enhance their signal, noble gas nuclei can become hyperpolarized, whose polarization level is approximately 10^{-1}. It is therefore feasible to use hyperpolarized noble gases to attain enhanced lung MR images.

In general, hyperpolarized gases involve noble gases, such as ^{3}He, ^{129}Xe and ^{83}Kr, that can undergo magnetic resonance and have a spin quantum number of (2n-1)½, where n is any integer above 0. Noble gases undergo hyperpolarization via spin exchange optical pumping (as described in section 1.3.1). One of the major differences between proton and HP gas MRI is that the signal for proton MR lung imaging comes from the lung tissue, whereas the signal from HP gas MRI comes from the HP gas distributed within the alveoli.[13] Another major difference is that the hyperpolarized gases evenly distribute within the airspaces and airways of the lungs, which eliminates the problem of the short T2* relaxation time associated with ^{1}H in the lungs.[11]

There are implications in HP gas MR lung imaging, which are discussed in section 1.3.2. Since it is important to quantify the uptake and exchange of xenon in the lungs, xenon measuring techniques are explained in section 1.3.3. Finally, section 1.3.4 discusses MRI acquisition methods for HP gas MRI since the T1 relaxation for HP gases is non-recoverable.

1.3.1 Gas Polarization and Spin Exchange Optical Pumping

Spin exchange optical pumping (SEOP) is a technique in attaining HP ^{129}Xe or HP ^{3}He. SEOP uses circularly polarized laser light (involving optical/near optical photons) that carries angular momentum.[14] Noble gas atoms, however, are invisible to optical/near optical photons for nuclear excitations to occur; therefore, rubidium (Rb) is used to absorb the laser light and its angular momentum.[14] Rb is used in SEOP because of its simple electron structure and has a large

cross section that allows itself to absorb wavelenths of visible light. It can also preseve its long electron spin state and has a relatively high vapour pressure at low temperatures.[15] In SEOP, the laser light polarizes Rb, in which its valence electron is transferred from the spin down(up) to the spin up(down) orientation, depending on helicity of the laser (right or left circularly polarized light).[14] Assuming clockwise polarization of the laser, Rb can only absorb the laser light if their electron spins are down; therefore, the alkali vapor in the sample have electron spins positioned in the spin up direction.[14] For spin-conserving collisions, the spin of the valence electron for Rb remains flipped up until it collides with ^{3}He or ^{129}Xe, resulting in depolarization of the Rb atom.[11] After the collision, the ^{3}He or ^{129}Xe becomes polarized, where its spin in its nucleus is aligned in the spin up position. Meanwhile, the valence electron of the Rb atom absorbs another photon, and therefore undergoes realignment. Rb continues to collide with noble-gas nuclei to enhance the polarization of the HP ^{129}Xe or ^{3}He gas sample.[11] The steady state polarization achieved via spin-exchange between the noble gas nucleus and alkali metal is given by the following equation:[16]

$$[\text{P(noble gas)}] = [\text{P(alkali)}] + \frac{\gamma SE}{\gamma SE + \gamma SD} \qquad (1.44)$$

where γSE is the rate of spin-exchange for the alkali–noble gas interaction; γSD is the spin destruction rate of the noble gas (spin-rotating coupling, wall interaction, etc); and [P(alkali)] is the volume-averaged alkali polarization in the pumping cell. According to equation *(1.44),* the polarization of the noble gases will be less than or equal to the polarization of the alkali metal.[16] Eventually, the HP ^{129}Xe or ^{3}He can be separated from its buffer gases via cryogenic separation.[16]

To preserve the hyperpolarized spin state of the gas sample, it needs to have a slow *T1* relaxation.[17] The nuclear spin polarization for a hyperpolarized gas sample can be determined by

the signal enhancement factor, which is the ratio of the HP NMR signal to that of a thermally polarized sample.[17] The thermal spin polarization of a sample at ambient temperatures and within orders of several Tesla is

$$P_{therm} = \frac{|\gamma|\hbar B_0}{3k_B T}(I+1) \qquad (1.45)$$

where γ is the gyromagnetic ratio, k_B is the Boltzmann constant, I is the nuclear spin, and $\hbar = h/2\pi$, which is Planck's constant.[17] The polarization, P_{hp}, of a hyperpolarized gas sample, can be determined by the product of the SEOP enhancement factor and P_{therm}.[17]

Noble gases need to be hyperpolarized because of their low concentration at standard temperature and pressure. In addition, thermally polarized gases also have low polarization levels. Since their concentration and polarization levels are low, then the MRI signal is also low, as governed by the following relationship:

$$S \propto N \times P \qquad (1.46)$$

where S is signal intensity, N is the number of nuclei, and P is the polarization level for a given sample of gas, liquid, or solid. Based on *(1.46)*, the MRI signal from noble gases can be enhanced by increasing their polarization level.

.

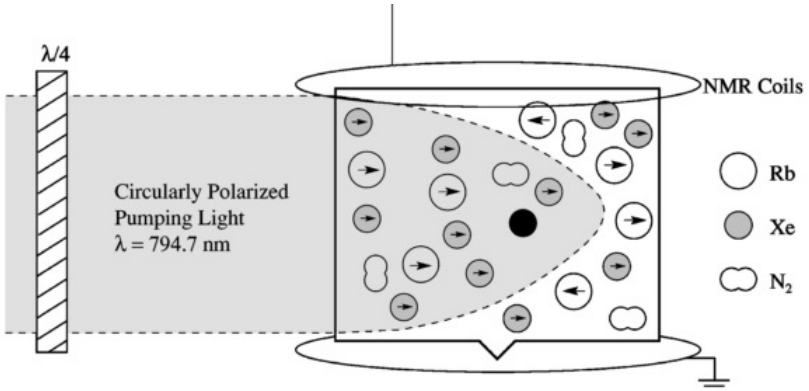

Figure 1.6: Spin Exchange occurring between Rb electrons and ^{129}Xe nuclei in gas-phase collisions. Adapted from ref. 14.

1.3.2 HP Noble Gas MR Lung Imaging

HP gas MRI has implications for providing enhanced lung images that convey functional and anatomical information of the lungs. For example, Albert *et al*. attained ex vivo lung images from a mouse using HP ^{129}Xe, as shown in figure 1.7.[18] In addition, Dr. Albert's lab demonstrated the use of HP ^{3}He to image different lung diseases, such as asthma, COPD, and asbestosis, as indicated in figure 1.8.[19]

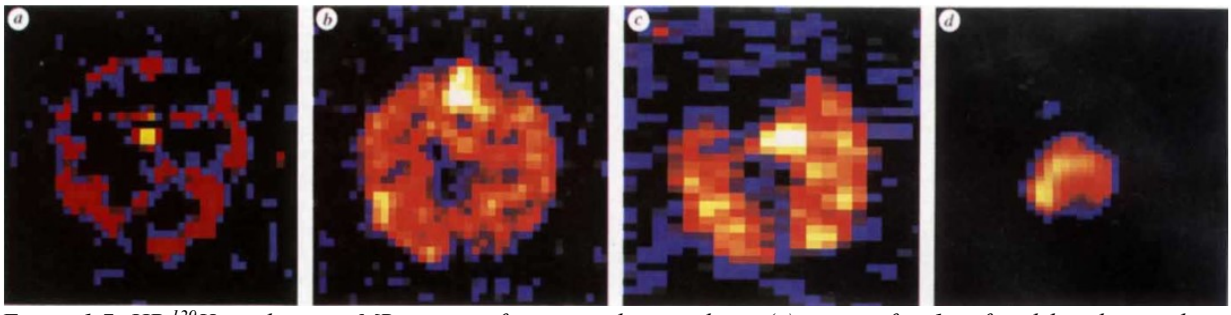

Figure 1.7: HP ^{129}Xe and proton MR images of an excised mouse lung. (a) image after 1 s of seal-breakage, where ^{129}Xe is delivered to the excised mouse lung while the N_2 gas is displaced from the lung. (b) another excised lung image after 2s ^{129}Xe gas is delivered to the excised lung. (c) 7 s after seal-breakage, with remaining HP ^{129}Xe gas. (d) proton MR image. Images taken with permission from ref. 18.

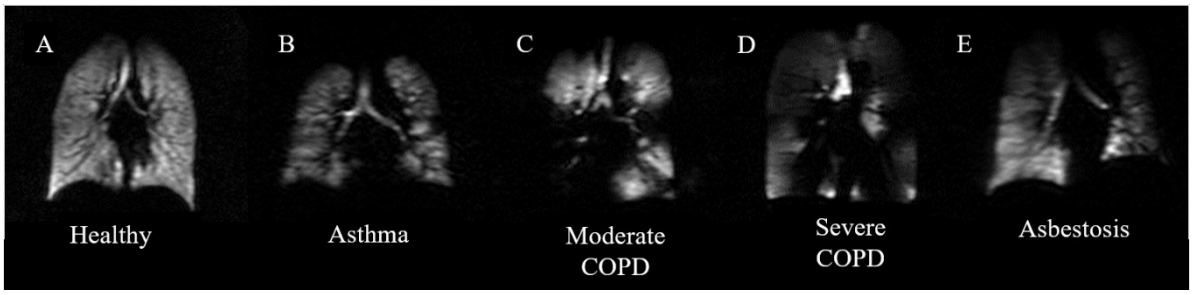

Figure 1.8: HP ^{3}He MR ventilation images from (a) healthy volunteer, and four separate individuals diagnosed with (b) asthma (c) moderate COPD (d) severe COPD and (e) asbestosis. There is a homogenous distribution of ^{3}He in the volunteer with healthy lungs. Dark regions indicate areas with no ^{3}He, which reveals areas of ventilation defect. Images from A to D are from ref. 19. Image E was taken from Dr. Mitchell Albert's lab.

HP gas MRI has the capacity to identify changes in the pulmonary structure and ventilation in the lungs, and therefore can differentiate lung pathologies.[11] Any modification in barrier tissues has an impact on gas exchange. Healthy subjects have even distribution while diseased

states have heterogenous distribution of HP gas within their lungs.[20] Any variation in signal-intensity within the lungs, besides the blood vessels, are attributed to potential pathological modifications within the lung tissue. Well-ventilated areas within the lungs appear bright while unventilated areas appear dark.[20] Additionally, for HP ^{129}Xe, there is an inverse correlation in the thickness of barrier tissues and gas distribution; an increase in tissue thickness results in decreased ^{129}Xe gas distribution and exchange with red blood cells (RBCs).[21] Any alterations to the lungs, such as inflammation, pulmonary edema, scarring, and the presence of cancer cells can impact gas exchange.[21] Therefore, based on the distribution of ^{129}Xe in the lungs, one can deduce their disease state.

It is important to consider the relaxation time for HP ^{129}Xe and ^{3}He since it affects their signal-to-noise ratio (SNR) in MRI. Pure samples of HP ^{3}He and ^{129}Xe have very long relaxation times. Therefore, HP ^{3}He or ^{129}Xe undergo no significant loss in polarization between its preparation and administration to the subject. However, upon interaction with paramagnetic oxygen, the relaxation times for hyperpolarized gases undergoes substantial reduction. The longitudinal relaxation rate ($1/T1$) upon interaction with oxygen for ^{3}He is governed by the following equation:

$$\frac{1}{T1} = 0.45\left(\frac{299}{T}\right)^{0.42}[O_2]\,, \qquad (1.47)$$

where T is temperature measured in Kelvin (K), and $[O_2]$ is oxygen concentration measured in Amagat.[22] The longitudinal relaxation rate for the interaction between oxygen and ^{129}Xe is governed by

$$\frac{1}{T1} = k\,pO_2\,, \qquad (1.48)$$

where $k = 0.38$ bar^{-1}s^{-1} at body temperature and pO_2 is the partial pressure of oxygen in bar.[23] Equations *(1.47)* and *(1.48)* show a direct correlation between oxygen concentration and

longitudinal relaxation rate for HP ^{3}He and HP ^{129}Xe.

HP ^{3}He and ^{129}Xe are the two most widely used gases in HP noble gas MRI. When ^{3}He MR images are compared with those of ^{129}Xe, the former have better SNR and can better detect ventilation defects.[21] This phenomenon results from ^{3}He having a higher gyromagnetic ratio than ^{129}Xe. However, the low gyromagnetic ratio and low diffusion coefficient of ^{129}Xe also offers other advantages over ^{3}He. The first advantage is that ^{129}Xe is less subject to off-resonance effects than ^{3}He because of its lower gyromagnetic ratio. To utilize ^{129}Xe advantages, however, it is important to have high levels of polarization.[10]

The properties of ^{129}Xe differ from those of other noble gases.[21] First, ^{129}Xe is soluble in barrier tissues and blood upon inhalation. Additionally, ^{129}Xe nuclei exhibit a chemical shift of 197 ppm in barrier tissue and of 217 ppm in blood, which are both relative to the chemical shift of pure gas at 0 ppm.[21] As a result, ^{129}Xe can be used in chemical shift imaging, which makes it plausible to measure regional gas exchange.[21] The properties of ^{129}Xe were first demonstrated in rodents and canine models, which showed, in a fibrotic disease model, decreased gaseous ^{129}Xe diffusion within areas of the lungs damaged from fibrosis.[21] This situation led to the idea of conducting clinical trials to detect lung defects in humans.[24,25]

Gaseous ^{129}Xe has a larger diffusion coefficient than water in biological tissues, which has both positive and negative implications in MR imaging.[26] First, spatial-encoding gradients can induce diffusion-induced attenuation of the MR signal, which can limit the SNR and spatial resolution of HP ^{129}Xe MR images.[26] It is important to consider this factor when developing HP gas MRI pulse sequences.[26] Conversely, the high diffusion coefficient of ^{129}Xe allow for the execution of diffusion-weighted MR imaging, which can characterize the microstructure of the lungs[26] and allows for ADC mapping.

1.3.3 Indirect and Direct Measurement of Dissolved-phase Xenon in the Lungs

The advent of HP ^{3}He and ^{129}Xe MRI allowed for static imaging of airspaces within the lungs. On the other hand, it is important to measure the amount of xenon in the lungs to quantify lung function and pathology. It is plausible to measure dissolved-phase ^{129}Xe in the lungs since the ^{129}Xe atom is soluble in the lung parenchyma and blood. In general, there are direct and indirect techniques for measuring dissolved-phase ^{129}Xe in the lungs. Direct measurement of dissolved-phase ^{129}Xe was first demonstrated in early clinical trials via ^{129}Xe MR spectroscopy.[27] However, only two percent of HP ^{129}Xe resides in the lung tissue and blood, which makes their associated SNRs too low for dissolved-phase MR imaging.[26] Before improvements were made in gas polarization technology, it was difficult to produce high-resolution dissolved-phase ^{129}Xe MR images via direct measurement.[27] Therefore, xenon-polarization transfer contrast (XTC) and multiple-exchange time XTC (MXTC) were developed to indirectly measure xenon in the lungs.[28]

XTC indirectly measures dissolved-phase ^{129}Xe by measuring decreased magnetization of gaseous ^{129}Xe, where gaseous ^{129}Xe continually exchanges with its blood and lung tissue counterparts.[29] In general, XTC utilizes a small flip-angle gradient echo sequence and involves the collection of two ^{129}Xe images.[29] To attain the first image, a series of RF pulses separated by a constant delay is applied at the dissolved-phase ^{129}Xe frequency.[29] The bandwidth for this RF pulse is small enough to not actively depolarize the gas-phase ^{129}Xe.[29] Between each RF pulse, there is some magnetization recovery of the dissolved-phase ^{129}Xe since the ^{129}Xe atoms exchanges with its gaseous phase counterparts.[29] There is also simultaneous, non-recoverable decay of the gaseous ^{129}Xe magnetization. An additional gas-phase ^{129}Xe MR image is produced using the same parameters as that of the first gas-phase ^{129}Xe MR image. The two ^{129}Xe MR

images are combined to form a depolarization map, where the intensity of each pixel signifies relative change in gas polarization.[29] The depolarization map creates a ratio between the two ^{129}Xe images, where each pixel is associated with a particular volume of ^{129}Xe gas exchange.[29]

Another method to indirectly measure dissolved-phase xenon in the lungs is to use MXTC, which is an extension of XTC. This method involves the collection of data at multiple delay times.[30] MXTC collects four 3D MR images using fast low angle shot pulse sequences. MXTC allows for the derivation of two lung-function parameters, which are septal wall thickness and tissue-to-alveolar volume ratio. If there are alveolar sites in which ^{129}Xe atoms did not undergo depolarization, then these sites lack gas exchange, and therefore do not contribute to image contrast. As a result, MXTC can detect alterations of lung tissue due to lung diseases.

Direct measurement of dissolved-phase xenon in the lungs became feasible upon improvements in gas polarization. Such improvements include producing polarization levels at 40 to 50 percent for ^{129}Xe and generating litre quantities of HP ^{129}Xe gas. As a result, the SNR of dissolved-phase ^{129}Xe in the lungs became high enough for direct dissolved-phase MR imaging, suitable for a single-breath hold period for humans. Moreover, Cleveland *et al.* and Driehuys *et al.* developed methods that involve the direct measurement of xenon in the lungs.

Cleveland's method involves using an RF pulse with a high-flip angle whose frequency matches the precessional frequency of dissolved-phase ^{129}Xe.[31] The high-flip angle compensates for the low percentage of ^{129}Xe that resides in the lung tissue and blood. Following the application of the high-flip angle RF pulse angle, gas exchange restores the xenon in the dissolved-phase compartments within a time period of 10 ms.[26] A separate HP ^{129}Xe ventilation image is then acquired and normalized with the dissolved-phase image to quantify the amount of gas exchange that occurs in each region of the lung.[31] See Figure 1.9 for Cleveland's results.

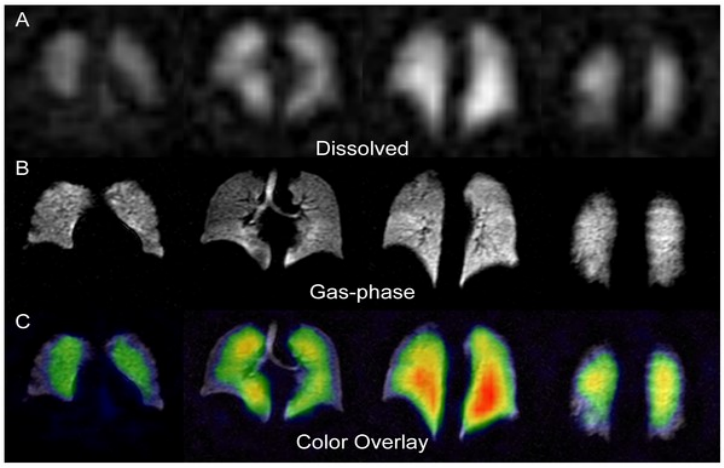

Figure 1.9: HP ^{129}Xe MR images of lungs from a healthy volunteer. (A) Dissolved-phase ^{129}Xe MR images with slice thickness of 15 mm. (B) The corresponding gas-phase ^{129}Xe MR images from the same volunteer with the same slice thickness as in (A). (C) Colour-coded dissolved-phase ^{129}Xe MR images overlaid on gas-phase ^{129}Xe MR images. Images taken with permission from ref. 31.

Driehuys *et al*. developed the xenon alveolar capillary transfer (XACT) imaging technique, which involves a 2D radial sequence to acquire a dissolved-phase ^{129}Xe.[32] The image is subsequently separated into tissue-dissolved and blood-dissolved ^{129}Xe MR images using the one-point Dixon method.[33] Figures 1.10 B and C show the ^{129}Xe signal in lung tissue and blood, respectively; images were acquired with a spatial resolution 1.25 x 1.25 mm^2 in a healthy control rat using the XACT technique. Figure 1.10 A shows a ventilation image that was attained at different breath-hold from figure B and C. For the injured rat, the dissolved-phase ^{129}Xe in tissue (figure 1.10 E) closely resembles the ventilation image (figure 1.10 D); however, there is a lack of ^{129}Xe uptake by red blood cells in the injured rat with left lung fibrosis, as shown in figure 1.10 F. This decreased uptake is due to the thickening of the alveolar wall (also confirmed via histology), resulting in decreased transfer of ^{129}Xe from the alveoli to red blood cells.[32] Additionally, Cleveland *et al*. used a similar method to Driehuys *et al*. to detect decreased ^{129}Xe from partitioning between the alveoli and the blood in an animal with fibrosis.[34]

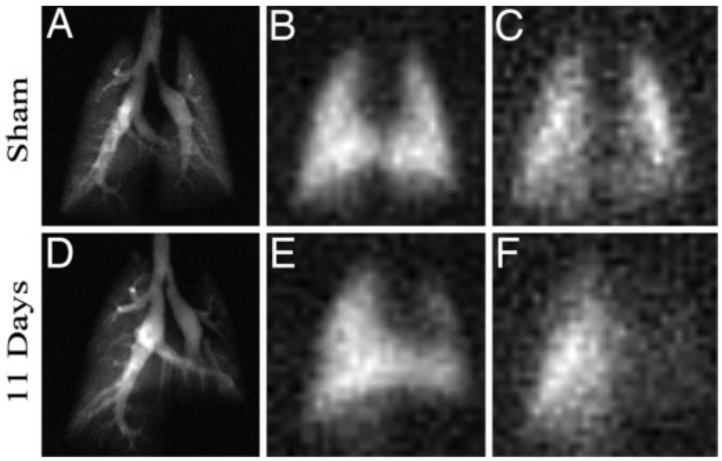

Figure 1.10: Comparison of ^{129}Xe MR images in a sham lung from a healthy control rat (A to C) versus injured rat with left lung fibrosis (D to F). MR images were acquired using the XACT imaging technique. The ventilation image in (A) closely resembles the images for ^{129}Xe in lung parenchyma (B) and blood (C). For the injured rat, (E) shows ^{129}Xe in tissue, which closely resembles the ventilation image in (D). However, the image for ^{129}Xe in blood (F) shows decreased uptake of ^{129}Xe by red blood cells in the left lung, which has fibrosis. Images were taken with permission from ref. 32.

1.3.4 MRI Acquisition Methods for HP Noble Gases

Since the hyperpolarized state for HP gas nuclei is not in equilibrium with the static magnetic field of the MRI scanner, then its hyperpolarized state and its detectable magnetization are non-recoverable. As a result, once HP gas nuclei undergo T1 relaxation (resulting in the decay of their hyperpolarized state), then they undergo decay in their magnetization, which is non-recoverable. In general, pulse sequences with multiple RF pulses, such as spin echo (SE) and fast spin echo (FSE), are generally avoided. Fast low-angle shot (FLASH) and variable flip-angle pulse sequences are better optimized for HP gas MRI than SE and FSE pulse sequences since they effectively use the available magnetization of HP noble gases before it decays or becomes destroyed.[35]

The pulse sequences that are generally used in HP gas MRI are FLASH and variable-flip angle approaches. FLASH, however, leads to non-uniform weighting of k-space and k-space artifacts, such as loss of edge enhancement, blurring, and a reduced SNR.[35] The most effective pulse sequence in HP gas MR imaging is the variable flip angle approach, in which the flip angle of each RF pulse is gradually increased throughout the MRI acquisition, leading to constant transverse magnetization throughout the MRI acquisition process.[36] The variable flip angle approach, therefore, maintains a consistent SNR within central lines of k-space for HP gas MRI.

1.4 HP ^{129}Xe Brain Imaging

Previous research demonstrated the use of HP gas MRI in detecting a variety of lung diseases, such as asthma, COPD, and cystic fibrosis.[37] On the other hand, ^{129}Xe is highly lipophilic and its gas-blood partition coefficient, 0.15, allows for rapid transportation within the circulatory system.[38] Because of these properties, it is feasible to combine HP ^{129}Xe with MR brain imaging and fMRI. In this manner, ^{129}Xe is considered to be a brain perfusion marker, where there is increased perfusion of HP ^{129}Xe in activated brain regions.[39]

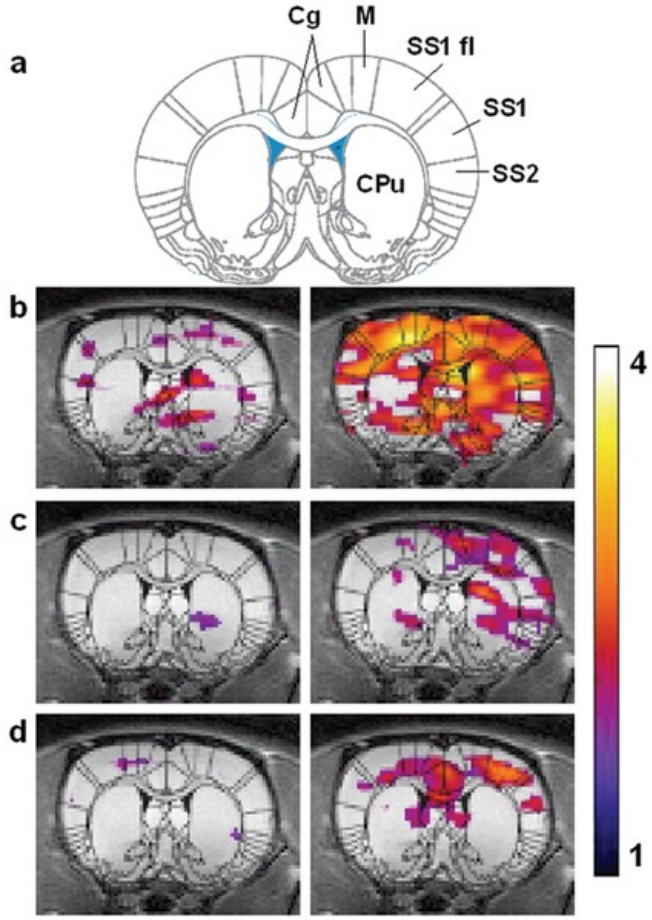

Figure 1.11: HP ^{129}Xe fMRI before and after pain response in a Sprague-Dawley Rat. The images in the left panel indicate baseline signal intensity. the images in the right panel indicate pain response after injecting 20 uL capsaicin into the right forepaw of a rat. The ^{129}Xe signal intensity was overlaid on a rat brain atlas (shown in a), which shows that the ^{129}Xe fMRI signal in the right panel corresponds to the brain region for pain response. Images were taken with permission from ref. 41.

Some in vivo studies have demonstrated ^{129}Xe fMRI as a highly sensitive imaging modality. For example, Swanson *et al*. demonstrated ^{129}Xe NMR spectroscopy and MRI in Sprague-Dawley rats.[40] Additionally, Mazzanti *et al.* also showed functional ^{129}Xe MRI of pain response in an animal model (figure 1.11).[41]

Most in vivo ^{129}Xe fMRI studies, however, are limited by xenon's short T1 relaxation time in blood and its low solubility in tissues. The short T1 of xenon in blood also reduces its signal upon reaching the brain. Other factors, such as

field strength and blood oxygenation levels, affect the T1 relaxation time for ^{129}Xe, thereby affecting its SNR. Albert *et al*. determined that the T1 relaxation times for ^{129}Xe in oxygenated and deoxygenated blood are, respectively, 13 s and 4 s.[42] This difference in T1 values is most likely attributed to the interaction with deoxyhemoglobin and cross-relaxation of protons with Xe.[43]

It is important to measure the T1 values for ^{129}Xe in the brain since they affect the SNR of HP ^{129}Xe MR brain imaging. To measure the T1 value, previous studies assessed the change in dissolved-phase ^{129}Xe NMR signal intensity to quantify the uptake and/or washout of HP ^{129}Xe in brain tissue.[44,45,46,47,48] Subsequently, these studies developed theoretical models to assess the T1 value for ^{129}Xe in brain tissue, which accounted for pulmonary blood flow and respiration rate since they affect ^{129}Xe signal dynamics within the brain.[39,49] Some in vivo brain studies reported T1 values that range from 3.6 to 26 s.[44,45,48,39] This variation is likely due to the heterogeneity of T1 values in different tissue compartments of the brain. This variation also likely results from the low SNR obtained in most of these studies.[39] Zhou *et al.* determined that the T1 value of ^{129}Xe in a rat brain is only 15 s, which accounted for low SNR.[39] Killian *et al.* reported T1 values of 8 s and 14 s for white and grey matter, respectively.[47] Kimura *et al.* measured a T1 value of 14 s in the mouse brain.[50]

Previous researchers reported different ^{129}Xe T1 relaxation values for the brain in rats. Wilson *et al*. measured the T1 value in rat brain tissue to be 18±1 to 22±2 s, depending on oxygenation levels of the tissues.[51] Additionally, a range of values for T1 for rat brain in vivo were reported by several researchers. Choquet *et al*. reported a T1 value of 3.6±2.1 s,[48] whereas Wakai *et al*. reported a value of 26±4 s.[45]

One prime example of a theoretical model for signal dynamics of HP ^{129}Xe in brain tissue is that developed by Fujiwara and colleagues.[46,50] This model assumes a steady-state concentration of ^{129}Xe within the alveoli during continuous xenon ventilation. Therefore, Fick's principle can be used to determine ^{129}Xe concentration in the brain tissue (C_i):[49]

$$\frac{dC_i(t)}{dt} = F_i C_a - \alpha C_i\,, \quad where\ \alpha = \frac{F_i}{\lambda_i} + \frac{1}{T_{1i}} \qquad (1.49)$$

where the flip angle is θ; C_a is the steady state concentration of ^{129}Xe in arterial blood; λ_i is the partition coefficient between the tissue and blood; and F_i is the global cerebral blood flow in mL of blood per mL of tissue per minute.[46]

Since RF pulses induces T1 relaxation of HP ^{129}Xe (thus causing decay of its hyperpolarized state), then the following equation can be used to determine the ^{129}Xe concentration in the brain for an MRI acquisition with repetitive RF pulses:

$$\frac{dC_i(t)}{dt} = F_i C_a - \beta C_i \quad with \quad \beta = \frac{F_i}{\lambda_i} + \frac{f(1-cos\,\theta)}{TR} + \frac{1}{T_{1i}}\,, \qquad (1.50)$$

where θ is the flip angle, and f is the proportion of the remaining HP ^{129}Xe magnetization after the application of an RF pulse.[50] The ^{129}Xe NMR signal intensity, *S(t)*, can be determined via equation *(1.50)*, where the initial condition is $C_i(0) = F_i C_a/\alpha$, derived from equation *(1.49)* as a steady state condition.[52]

1.5 HP ^{129}Xe biosensors and HyperCEST

It is difficult to selectively deliver HP ^{129}Xe atoms to a particular site. HP ^{129}Xe atoms are also prone to poor sensitivity because of their non-recoverable polarization at room temperature.[53] It is, however, feasible to take advantage of its available magnetization by combining HP ^{129}Xe atoms with ^{129}Xe biosensors for hyperpolarized xenon chemical exchange saturation transfer (HyperCEST). In general, the type of biosensor used in HyperCEST is a supramolecular cage, which non-covalently binds to the ^{129}Xe atom.[53] Examples of

supramolecular cages are cryptophane-A (Cr-A) and cucurbit[6]uril (CB[6]), which are further discussed in section 1.5.1.

In general, there are two factors in developing supramolecular cages for xenon. First, it is important that the chemical shift for cage-bound xenon is considerably different from that of free xenon in solution.[20] For example, the chemical shift for xenon bound to cryptophane-A is 61.8 ppm away from the free-dissolved ^{129}Xe NMR peak at 0 ppm.[54] Hence, the cage-bound ^{129}Xe is distinguishable from free gaseous and free dissolved ^{129}Xe within biological tissues.[20] Moreover, it is important that the frequency difference ($\Delta\omega$) between cage-bound and free-dissolved ^{129}Xe is greater than the exchange rate (τ_{ex}^{-1}) of ^{129}Xe inside and outside of its host (i.e. $\Delta\omega >> \tau_{ex}^{-1}$).[55] Otherwise, if $\Delta\omega << (\tau_{ex}^{-1})$, then ^{129}Xe has a "fast" exchange rate inside and outside of its host,[55] which allows the NMR peaks for cage-bound xenon and free-dissolved xenon to merge as one, single peak.[20] Thus, any HyperCEST effect would become undetectable.

Additionally, it is feasible to develop functionalized ^{129}Xe biosensors, which involve a supramolecular cage tethered to a motif that binds to a particular binding site in vivo, ex vivo, or in vitro.[53] As a result, functionalized ^{129}Xe biosensors can be used as a molecular imaging tool to detect biochemical changes associated with disease onset and progression.[53] Several functionalized ^{129}Xe biosensors are reported in the literature. For example, Spence *et al.* developed a functionalized ^{129}Xe biosensor that involved a cryptophane-A cage tethered to biotin to detect the presence of avidin.[56] Additionally, Rose *et al*. also developed an antibody-based ^{129}Xe biosensor to detect and target the CD14 receptor at a nanomolar concentration.[57] This biosensor was developed by conjugating an anti-CD14 antibody to avidin. Then, in a separate process, Cr-A was conjugated to biotin. Finally, the anti-CD14 antibody was attached to Cr-A by an avidin-biotin reaction. See figure 1.12 for a schematic of this functionalized ^{129}Xe biosensor.

Recently, Witte *et al*. introduced a functionalized xenon biosensor to detect the presence of glycans in live cells.[58] This biosensor is a Cr-A cage attached to a bio-orthogonal functional group, which binds to glycans found on the surface of cells.[58]

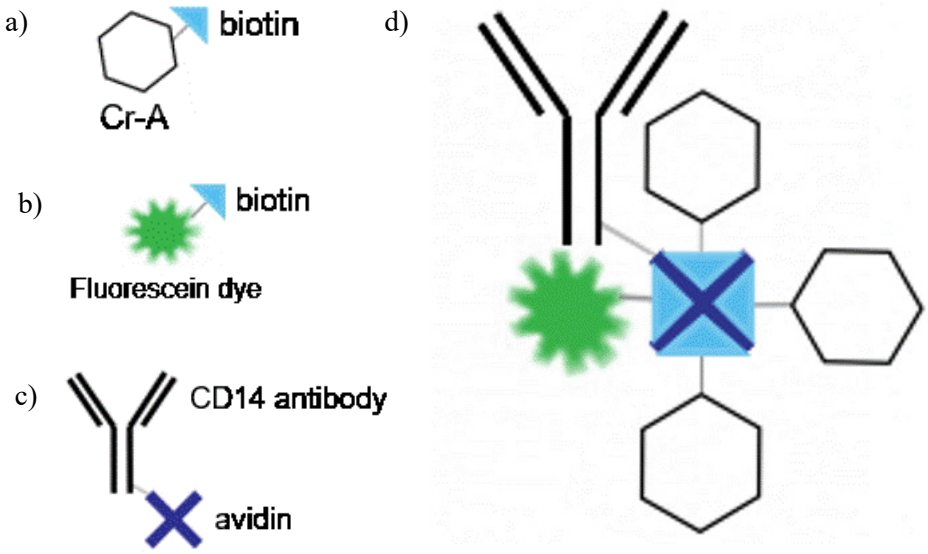

Figure 1.12: Schematic showing CD14 antibody functionalized ^{129}Xe biosensor. a) Cr-A conjugated to biotin; b) fluorescein dye conjugated to biotin; c) anti-CD14 antibody conjugated to avidin. d) CD14 antibody attached to three Cr-A cages via biotin-avidin conjugation. All images were taken with permission from ref. 57.

HyperCEST involves hyperpolarized xenon chemical exchange saturation transfer.[58] It was first developed by Schroder *et al*., who demonstrated HyperCEST using a functionalized ^{129}Xe biosensor.[55] In HyperCEST, xenon reversibly binds to its host, where, upon binding, there is a large chemical shift.[58] This technique also involves indirect measurement of bound xenon (dilute pool of xenon) by detecting the amount of unbound, depolarized xenon in solution.[59] HyperCEST works by applying an on-resonance saturation pulse that depolarizes the xenon while inside of its host; the depolarized xenon is then transferred to the free solution via chemical exchange.[59] To detect the accumulation of depolarized xenon in solution (i.e. a pool of depolarized ^{129}Xe atoms), an off-resonant saturation pulse is subsequently applied to the

system.[59] Since hyperpolarization creates a high population of spins in the ground state, there is sufficient difference between the initial condition (before applying the on-resonance pulse) and the depolarized final state (after the application of the on-resonance pulse).[59] If HyperCEST is conducted in a solution containing a functionalized ^{129}Xe biosensor and its target, and if unbound functionalized ^{129}Xe biosensor is subsequently washed from solution, then this situation allows the Lamour frequency of the biosensor-bound ^{129}Xe to be distinguished from that of free-dissolved ^{129}Xe, on an NMR frequency scale. The signal from free-dissolved ^{129}Xe is easily distinguishable from that of cage-associated ^{129}Xe since xenon has a unique chemical shift when placed in different chemical environments.[54] ^{129}Xe also has a relatively slow exchange rate, resulting in a selective saturation depletion in the z-spectra,[54] which is a plot of signal depletion and chemical shift of ^{129}Xe on an NMR frequency scale. The equation for signal depletion is

$$signal\ depletion = \frac{SNR(of\ HyperCEST) - SNR(of\ control)}{SNR(of\ control)} \qquad (1.51)$$

where *SNR(of HyperCEST)* and *SNR(of control)* are, respectively, the SNR of a sample after the application of an on-resonance pulse and after the application of an off-resonance pulse.

Additionally, the slow exchange rate poses no problem for the transfer of ^{129}Xe between different chemical environments since its T1 relaxation time is slow compared to the saturation time for ^{129}Xe to become depolarized while residing in its cage. As a result, depolarized ^{129}Xe is effectively stored in a bulk pool.[60]

To attain a sufficient HyperCEST signal, it is important that the frequency difference ($\Delta\omega$) between cage-bound xenon and its dissolved-phase counterpart is significantly larger than xenon's exchange rate (τ_{ex}^{-1}), where $\Delta\omega >> \tau_{ex}^{-1}$.[20] Additionally, the exchange rate needs to be faster than the relaxation rate of xenon (τ_{ex}^{-1}) and significantly slower than the saturation pulse

rate (W).[20] In this manner, the detection of the magnetization transfer between the caged and the free xenon can be measured.[20]

1.5.1 ^{129}Xe Supramolecular Cages

CB[6] and Cr-A are two ^{129}Xe supramolecular cages that exhibit appreciable binding with ^{129}Xe. CB[6] is a macrocyclic compound with six glycoluril units and a hydrophobic core.[61] Cr-A is a spherical molecule, consisting of two cyclotriveratrylene bowls connected via OCH_2CH_2O bridges.[62] See Table 1.0 that shows the differences in the physical and chemical properties for Cr-A and CB[6].

Table 1.0: Physical and Chemical Properties for Cr-A and CB[6].

Physical or Chemical Property	Cr-A	CB[6]
Molecular Formula	$C_{54}H_{54}O_{12}$	$C_{36}H_{36}N_{24}O_{12}$
Molecular weight (g/mol)	895.014	996.825
Volume of inner cavity (Å^3)	85 – 89[63]	142[64]
Exchange rate with ^{129}Xe in pure water (s^{-1})[65]	38	2100
K_a in pure water (M^{-1})[65]	850	2500
% occupancy with ^{129}Xe using QHyperCEST (using pure water as a solvent)[59]	29	49

Quantitative HyperCEST (QHyperCEST) analysis shows that CB[6] has higher occupancy of Xe ($\beta = 49\%$) than cryptophane-A (Cr-A, $\beta = 29\%$) under the same experimental conditions.[59] In addition, CB[6] has a better HyperCEST exchange rate than Cr-A, which are $2100s^{-1}$ and $38s^{-1}$, respectively, in pure water.[65] This difference in exchange rate indicates that a higher HyperCEST signal can be attained with CB[6] than Cr-A. Cucurbiturils, in general, exhibit very little to no cellular or in vivo toxicity.[66] Recently, Hane *et al.* detected the presence of CB[6] within the vasculature of a Sprague-Dawley rat via HyperCEST (see figure 1.13), which also showed accumulation of CB[6] in the brain, heart, liver, and kidney.[67]

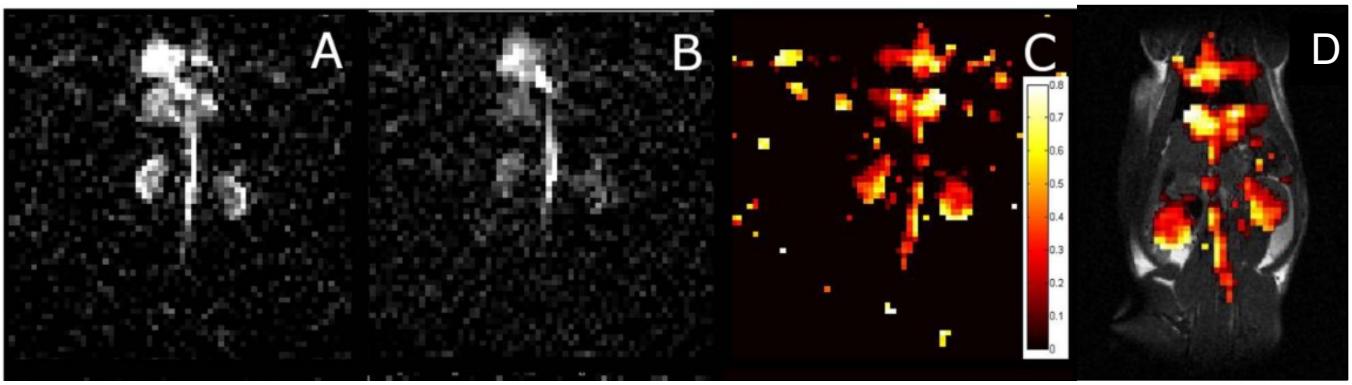

Figure 1.13: HyperCEST effect in the Sprague-Dawley rat after IV injection with a 10 mM CB6 solution. (A) shows a 2D gradient echo ^{129}Xe MR image after applying an off-resonance RF pulse at +260 ppm. (B) shows a 2D gradient echo ^{129}Xe MR image after applying a n on-resonant RF pulse at -260 ppm. (C) is a saturation map, which is the subtraction of the off-resonance image from the on-resonant image, pixel-by-pixel, which was then divided by the off-resonant image. (D) saturation map from (C) overlaid on a high resolution ^{1}H MR image. Images are from ref. 67 and are licensed under the Creative Commons License.

2. Research Objectives

HP ^{129}Xe MRI is a highly sensitive imaging modality. It has the capacity to show damaged and diseased areas within the human lung. Since the gas-blood partition coefficient for ^{129}Xe is 0.15,[38] then it can partition into the blood and travel to the brain. Therefore, HP ^{129}Xe fMRI can serve as an imaging tool for the brain, which can potentially provide a more refined signal of stimulated brain regions than proton BOLD fMRI. Additionally, HP ^{129}Xe can be combined with a biosensor to be utilized in HyperCEST, whose SNR is approximately three times larger than that of HP ^{129}Xe. The three objectives of this thesis research were: (a) to test xenon supramolecular cage molecules for a HyperCEST effect [chapter 3]; (b) to detect the HyperCEST effect in the lungs (or alveoli) of a Sprague-Dawley rat [chapter 4]; and (c) to demonstrate xenon fMRI in the brains of healthy human volunteers [chapter 5].

The first objective was to test a series of ^{129}Xe host molecules to determine their HyperCEST effect. If a ^{129}Xe host molecule exhibited a large HyperCEST effect, it was conjugated with an affinity tag to target pathological sites within a living organism. For example, a pseudorotaxane (a supramolecular cage threaded with an alkyl chain through its inner cavity) can be conjugated to thioflavin-t to detect plaques often associated with Alzheimer disease. The pseudorotaxane would encapsulate the xenon, while thioflavin-t would bind to the Alzheimer disease plaques. As a result, plaques inside of the brain would exhibit a HyperCEST effect.

The second objective was to detect the HyperCEST effect in the lungs (or alveoli) of a Sprague-Dawley rat using cucurbit[6]uril (CB[6]) as a xenon supramolecular cage. CB[6] was chosen because of its sufficiently moderate exchange rate with xenon, which is 2100 s^{-1} in an aqueous environment.[65] The HyperCEST experiments were conducted with reference to the gas phase since the gaseous HP ^{129}Xe has a higher SNR than its dissolved-phase counterpart within the lungs. A series of saturation maps were generated to image the HyperCEST effect in the

lungs of a Sprague-Dawley rat. This project would provide a foundation for using HyperCEST, in conjunction with an HP ^{129}Xe biosensor, to detect stage one of non-small cell lung cancer (NSCLC), which has a very low survival rate and is most often detected at a very late stage.[68] If successful, the subsequent step would consist of developing a functionalized xenon biosensor, whereby CB[6] is conjugated to an affibody (a small, engineered protein)[69] that detects the presence of the EGFR protein, which is overexpressed in up to sixty-two percent of NSCLC cases.[70] Overall, this project has the potential in creating a new detection technique for NSCLC.

The third objective was to detect a xenon fMRI signal in the brains of healthy human volunteers. It was hypothesized that the signal in HP ^{129}Xe fMRI relies on increased perfusion of xenon in stimulated brain regions. A comparison was made between proton and xenon fMRI scans to determine if xenon could be a highly sensitive imaging modality. If successful, then this project provides the potential for creating a new detection technique for Alzheimer disease.

3. Detecting the HyperCEST Effect in ^{129}Xe Host Molecules

3.1 Introduction

The two most common molecular imaging techniques, positron emission tomography (PET) and single-photon emission computed tomography (SPECT), require the use of radiotracers. DNP-MRI is an emerging, molecular imaging technique, which can be used to image ^{13}C pyruvate, a metabolite associated with some cancers.[71] HP ^{129}Xe MRI is another imaging modality that has the potential to detect and monitor the progression of diseases. In contrast to PET and SPECT, it does not require ionizing radiation and takes advantage of MRI's high spatial resolution. Additionally, HP ^{129}Xe atoms can be combined with^{129}Xe host molecules, such as supramolecular cages or pseudorotaxanes, for use in HyperCEST. It is advantageous to use HyperCEST since its SNR is approximately three orders of magnitude higher than HP ^{129}Xe alone. HyperCEST can also be combined with functionalized ^{129}Xe biosensors to detect the presence of a particular biomarker.

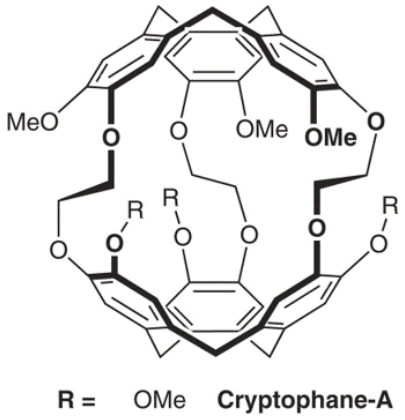

Figure 3.1: Structure of Cryptophane-A (Cr-A)

One of the most widely used ^{129}Xe host molecules in HyperCEST is cryptophane-A (Cr-A), as shown in figure 3.1. Although Cr-A can be functionalized with different ligands, Cr-A is limited by a low yield and multi-step synthesis.[72] It is feasible to explore other xenon hosts for HyperCEST, such as cucurbiturils, cucurbituril-based pseudorotaxanes and cyclodextrin-based

pseudorotaxanes, which possess an inner, hydrophobic cavity to non-covalently clathrate ^{129}Xe atoms via hydrophobic effects.[61] Some cucurbituril molecules include CB[6], CB[7], and CB[8] (shown, respectively, in figures 3.2 a) to c)). CB[6] and CB[7] show appreciable affinity for xenon, while CB[8] does not since the volume of its inner cavity is too large to interact with ^{129}Xe via hydrophobic effects. Another type of ^{129}Xe host molecule in HyperCEST involve cyclodextrins, which, in general, are a group of cyclic oligosaccharide molecules with glucopyranose units.[73] Examples include alpha (α) -, beta (β) -, and gamma (γ) cyclodextrins (as shown, respectively, in figures 3.2 e) to g)). They are suitable candidates for ^{129}Xe host molecules because they are water-soluble and non-toxic.[74] It is, however, usually difficult to detect their HyperCEST effect because they either lack the ability to bind to xenon in aqueous solution or the exchange rate for xenon is too fast for a xenon-bound cage peak to appear in the ^{129}Xe NMR spectrum.[75,76] To circumvent this problem, it is plausible to use a cyclodextrin as a supramolecular cage for creating a pseudorotaxane or rotaxane.

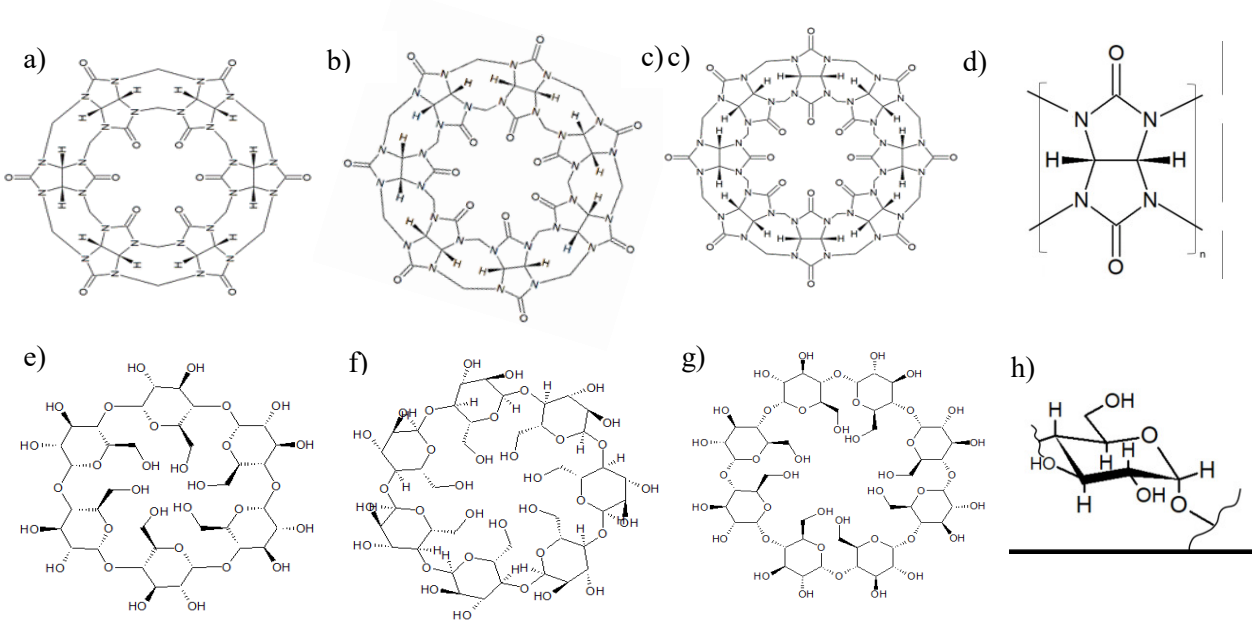

Figure 3.2: Structures of a) CB[6], b) CB[7], c) CB[8], d) the glycoluril unit of cucurbiturils (a to c), e) α-CD, f) β-CD, g) γ-CD, and h) the glucopyranose unit in cyclodextrin (e to g). The average pore sizes for cucurbiturils in a) to c) are, respectively, 3.9 Å, 5.4 Å and 6.9 Å. The average pore size for each cyclodextrin in e) to g), respectively, are 5.3 Å, 6.5 Å and 8.3 Å.

Other types of ^{129}Xe host molecules include pseudorotaxanes (figure 3.3a) and rotaxanes (figure 3.3b). A pseudorotaxane is a supramolecular cage with a long, alkyl chain threaded through its inner core.[77] The rotaxane is similar to a pseudorotaxane, except the rotaxane has a stopper placed on each end of the alkyl chain to prevent it from detaching itself from the supramolecular cage.[77] Stoppers allow for the conjugation of ligands, fluorophores, antibodies, and so on. By creating pseudorotaxanes and rotaxanes, it is possible to decrease the pore size of a supramolecular cage and thus decrease xenon's exchange rate such that it becomes NMR detectible.[78] However, to allow for the successful development of pseudorotaxanes and rotaxanes, the inner cavity of the chosen supramolecular cage needs to be large enough to accommodate both the alkyl chain and the ^{129}Xe atom.[74] The development of pseudorotaxanes and rotaxanes provides the opportunity to functionalize supramolecular cages, such as cyclodextrins or cucurbiturils, by threading them with an alkyl chain attached to an affinity tag, which can target a biomarker. The functionalization of cucurbiturils is otherwise difficult to do because of their highly stable structures.[79]

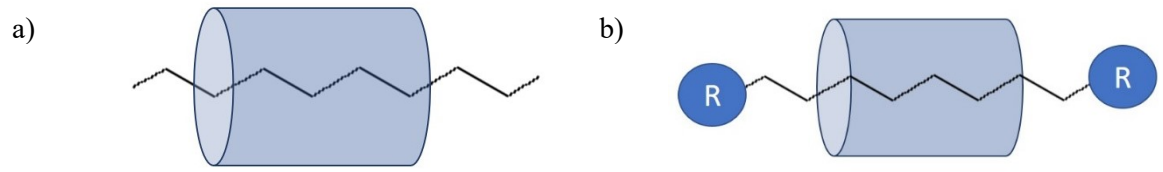

Figure 3.3: a) Schematic of pseudorotaxane, which has an alkyl chain threaded through the inner cavity of a supramolecular cage. b) Schematic of rotaxane, which is a supramolecular cage threaded with a long, alkyl chain that has an R group attached to each end. The R groups are potential sites for conjugating fluorophores, antibodies and so on.

The purpose of this project was to test a series of ^{129}Xe host molecules, such as supramolecular cages, pseudorotaxanes and rotaxanes, for their ability to exhibit a large HyperCEST effect (thus matching the first objective in chapter 2). If a ^{129}Xe host molecule exhibited an efficient HyperCEST effect, then the plan was to conjugate it with an affinity tag to bind to a particular disease site. Pulse parameters, such as repetition time (TR), the type of pulse,

and flip angle were optimized to maximize the HyperCEST effect. It is important that the RF pulse is applied at the same time in which the ^{129}Xe atom is inside of its host molecule. The type of pulse is an important aspect in HyperCEST since the sinusoidal wave pulse has a narrower bandwidth than a 3-lobe sinc pulse; hence, a sinusoidal saturation pulse can exclusively saturate cage-encapsulated ^{129}Xe without saturating the free-dissolved ^{129}Xe pool. It is important to apply a pulse at the cage-bound ^{129}Xe peak with a high enough flip angle to effectively destroy xenon's polarization and thus develop a sufficient, depolarized ^{129}Xe pool. A flip angle that is too small may not effectively destroy enough of xenon's polarization to develop a depolarized pool.

3.2 Materials and Methods

Naturally abundant xenon was polarized to approximately 30% using a Xemed polarizer (Xemed, Durham, NH) utilizing SEOP and dispensed in a 1 L Tedlar bag. A 30 mL syringe was placed on the inflow tube of the fritted glass phantom to drawn in approximately 1 mL of the supramolecular cage or pseudorotaxane sample. (Refer to each figure heading in the Results section for the structure and solution composition of the supramolecular cage sample used). The fritted glass phantom with the sample was subsequently placed inside of a custom-made RF ^{129}Xe bird-cage coil, that was placed inside the bore of the MRI scanner. The Tedlar bag with hyperpolarized xenon was placed inside a pressure chamber and connected to the inflow tube of the fritted glass phantom. The pressure chamber was hooked up to a nitrogen tank to push xenon continuously from the Tedlar bag into the fritted glass phantom, where it passed through a fine disc and produced microbubbles within the solution. The xenon gas then exited the fritted glass phantom through the outflow tube. The concentration of ^{129}Xe in the solution at any given time point was between 1 and 10 mM. All NMR spectra data were collected using a 3T Philips Achieva MRI scanner. For each type of pulse, the carrier frequency of the saturation pulse was

carried through a range of frequencies (between -150 and +30 ppm) that contained the ^{129}Xe-cage frequency. A z-spectrum was produced using a custom Matlab script (MathWords, Natick, MA, USA), which plotted the SNR of each carrier frequency of the saturation pulse against the SNR for the frequency that involved the free-dissolved ^{129}Xe. The 0 ppm on each z-spectrum was assigned to the free, dissolved-phase ^{129}Xe signal.

3.3 Results

Most pseudorotaxanes in this study did not exhibit a HyperCEST effect. However, the following ^{129}Xe host molecules exhibited a HyperCEST effect: an anthracene-based chain tethered through γ-CD (figure 3.5), a 100 μM solution CB[6] (figure 3.6), and 10 mM solution benzene-appended CB[6] (figure 3.7). The signal depletion for each ^{129}Xe host molecule is summarized in Table 3-1. The results in this chapter only include key results pertaining to this project. Refer to Appendix A for additional z-spectra and 1D spectra for other ^{129}Xe host molecules. that pertain to testing their HyperCEST effect.

Table 3-1: HyperCEST Results for ^{129}Xe Host Molecules

Figure Number	^{129}Xe Host Molecule	Signal Depletion (%)	Chemical Shift (ppm)
3.4	CB[7] with 5-C alkane chain	NE*	NE*
3.5	γ-CD with anthracene-based ligand	30	-40
3.6 a	100 uM CB[6] solution (supramolecular cage)	87	-72
3.6 b	100 uM CB[6] solution (supramolecular cage)	89	-78
3.7	10 mM solution of benzene-appended CB[6] (dissolved in deionized water)	70	-80
A-1	50 mM solution γ-CD with triphenyl(10-triphenylphosphaniumyldecyl)phosphanium	NE*	NE *
A-2	50 mM solution γ-CD with 1,5-bis(2-bromoethoxy)naphthalene	NE *	NE *
A-3	50 mM solution γ-CD with 1-ethyl-3-[12-(3-ethylimidazol-3-ium-1-yl)dodecyl]imidazol-1-ium	NE*	NE*
A-4	50 mM solution γ-CD with anthracene-based ligand	NE*	NE*
A-5	50 mM solution γ-CD with 1-ethyl-3-hexadecyl-1H-imidazole-3-ium	NE*	NE*
A-6	50 mM solution γ-CD with 1,5 -Bis(10-bromodedoxy)naphthalene	NE*	NE*
A-7	50 mM solution γ-CD with 1,5-Bis[2-[2-[2-(tosyloxy)ethoxy]ethoxy]ethoxy]naphthalene	NE*	NE*
A-8	γ-CD with N,N,N',N'-tetraphenyldecane-1,10-diamine	NE*	NE*
A-9	50 mM solution γ-CD with 3,3'-trimethylenebis(1-ethyl-1H-imidazole-3-ium)	NE*	NE*
A-10	γ-CD with anthracene-based chain	NE*	NE*
A-11	β-CD with anthracene-based chain	NE*	NE*
A-12	50 mM solution γ-CD with 1-ethyl-3[2-[5-2-(3-ethylimidazol-1-ium-1-yl)decoxy]naphthalen-1-yl[oxydec]imidazole-3-ium	NE*	NE*
A-13	γ-CD with bar before $NaBH_4$	NE*	NE*
A-14	300 mM solution γ-CD with spermine	NE*	NE*
A-15	300 mM solution γ-CD with spermidine	NE*	NE*
A-16	300 mM solution γ-CD with spermidine trihydro chloride	NE*	NE*
A-17	CB[6] with 5-C alkane chain	NE*	NE*
A-18	CB[8] with 5-C alkane chain	NE*	NE*
A-19	γ-CD with PEG-600	NE*	NE*
A-20	γ-CD with 10-C alkane chain	NE*	NE*
A-21	γ-CD with bar after $NaBH_4$	NE*	NE*
A-22	γ-CD with 8-C alkane chain	NE*	NE*

*NE means negligible effect, where the ^{129}Xe host molecule exhibited a very negligible to no HyperCEST effect. Figures A-1 to A-22 are found in Appendix A.

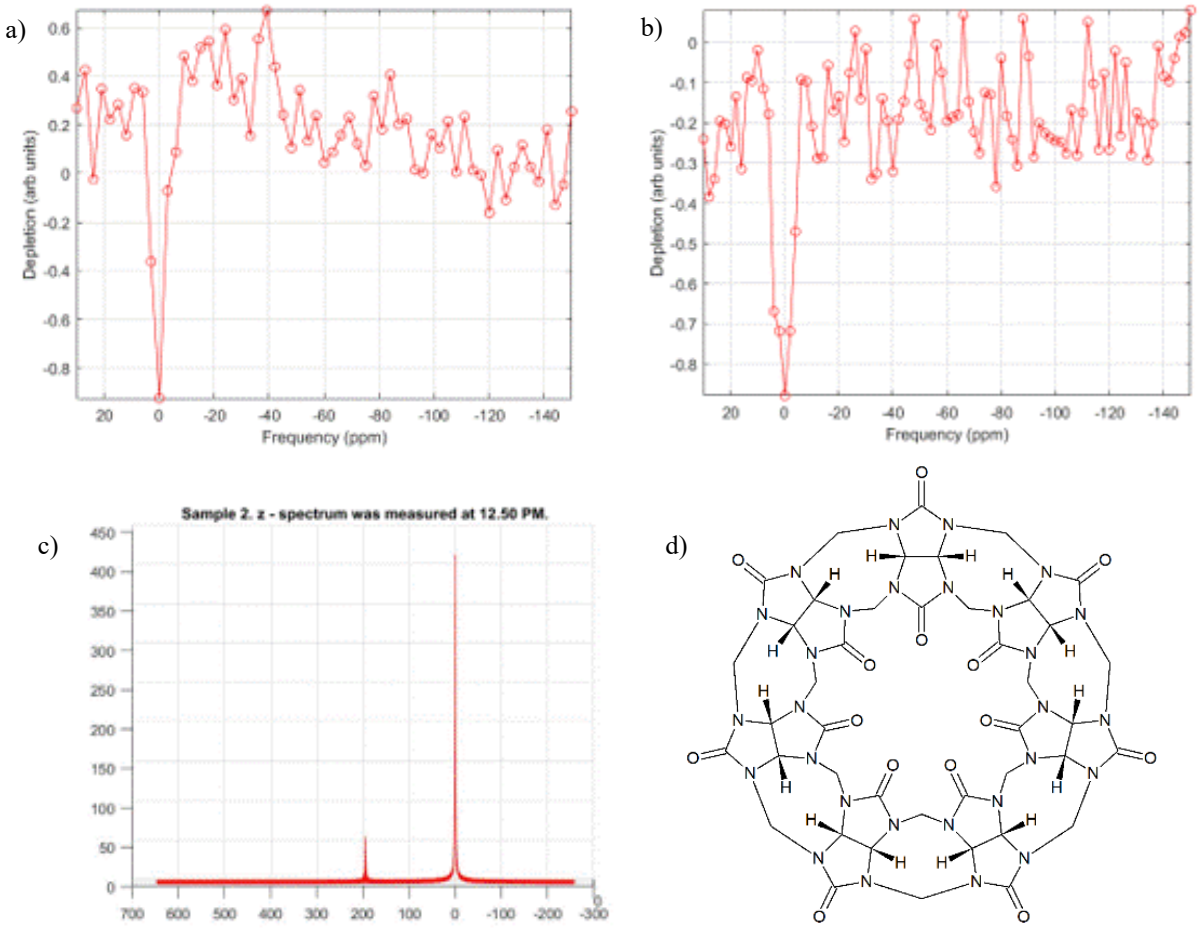

Figure 3.4 No HyperCEST effect was observed for this ^{129}Xe host molecule, which is a 5-C alkane chain tethered through CB[7] (dissolved in deionized water). a) Z-spectrum involving a 16 x 30 3-lobe sinc pulse, a 140° flip angle and TR = 7 s. b) Z-spectrum involving a 16 x 30 sinusoidal wave pulse, a 1530° flip angle and a TR = 6 s. c) 1D spectrum with gas-phase and dissolved-phase ^{129}Xe peaks at 0 and 198 ppm, respectively. d) Structure of CB[7].

a)

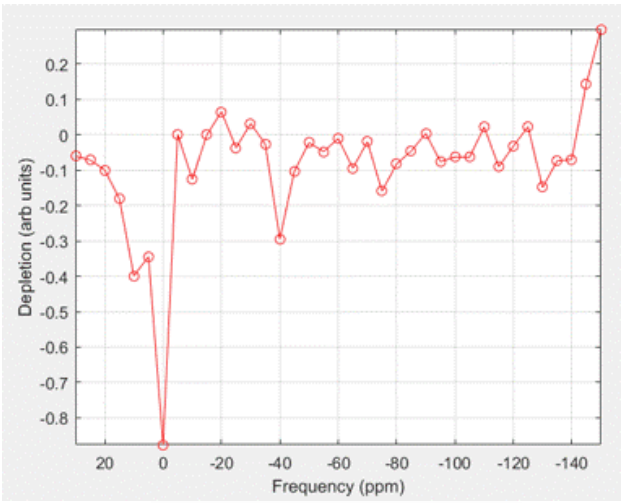

b)

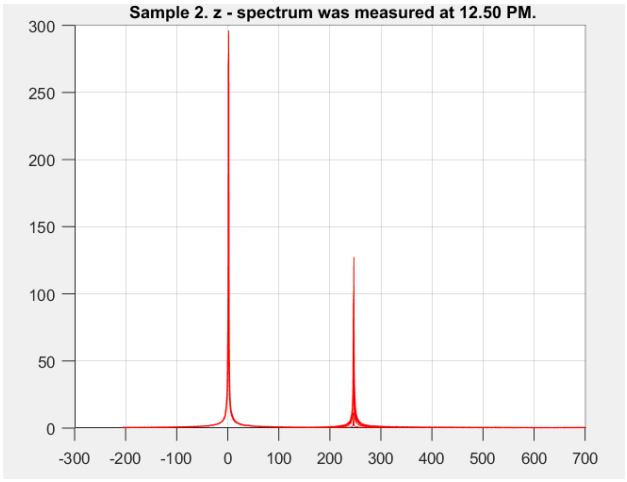

c)

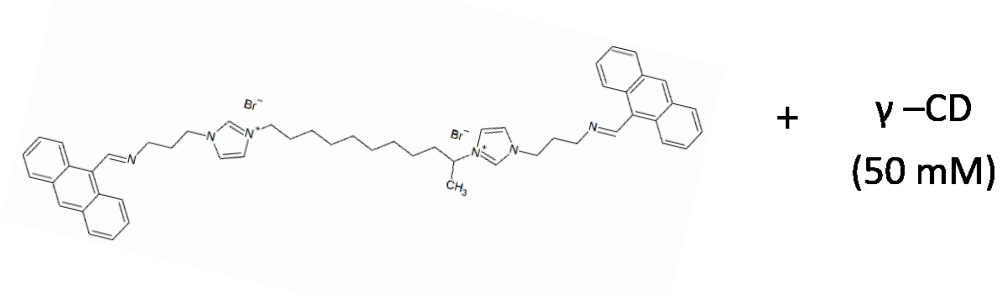

Figure 3.5: The ^{129}Xe host molecule is an anthracene-based chain tethered through γ-CD. a) Z-spectrum produced using a 16 x 30 3-lobe sinc pulse, a 140° flip angle, which shows 20% signal depletion at -40 ppm. b) 1D spectrum showing the 0 ppm and 240 ppm as the ^{129}Xe gas-phase and dissolved-phase peaks, respectively. c) Structure of anthracene-based chain that was threaded through γ-CD.

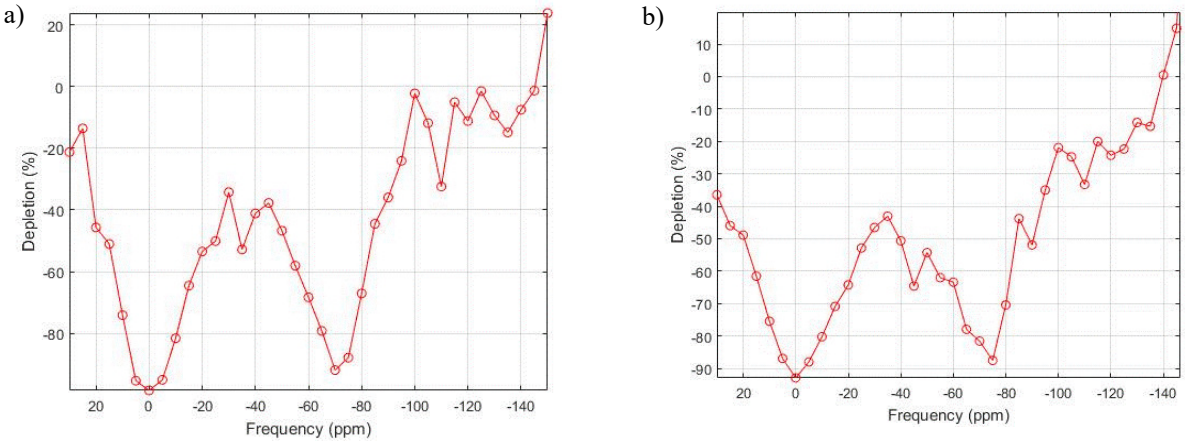

Figure 3.6: Z-spectra for 100 µM solution of CB[6] (dissolved in PBS buffer). a) and b) are z-spectra that involved a 16 x 30 sinusoidal wave pulse with a 1530° flip angle and a 5 ppm step. a) Z-spectrum shows signal depletion of approximately 87% at -72 ppm. b) Z-spectrum shows signal depletion of approximately 89% at -78 ppm.

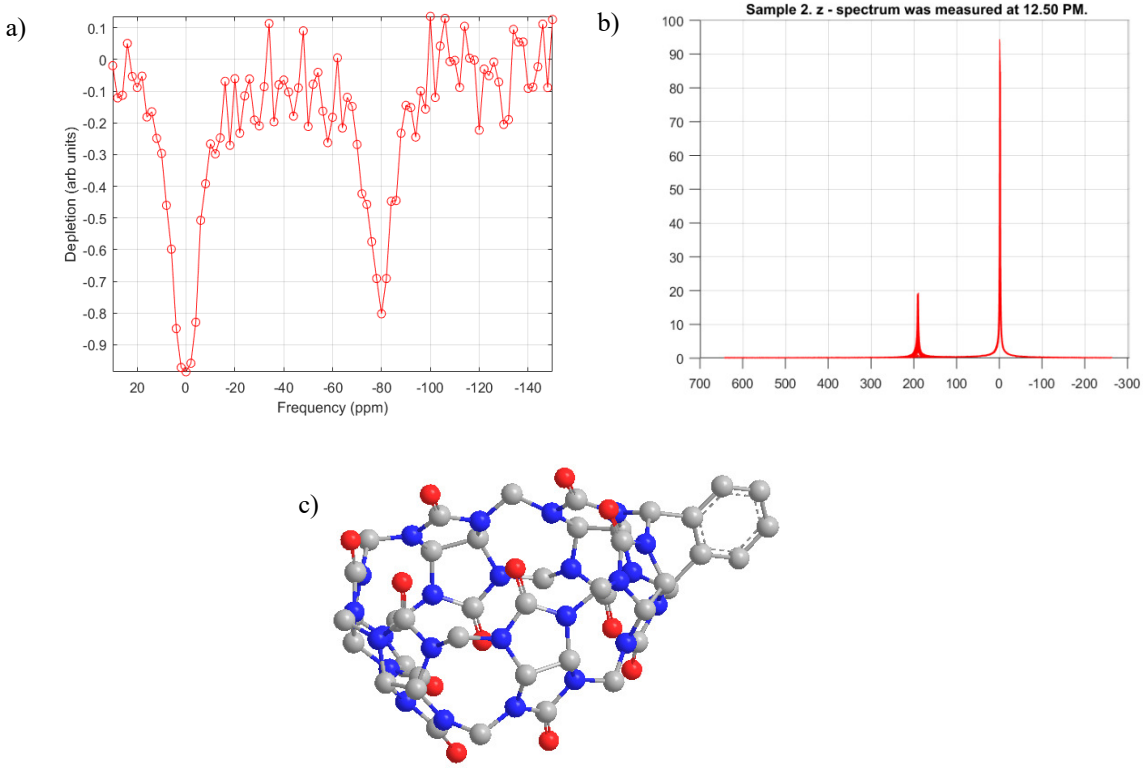

Figure 3.7: Z-spectrum and 1D spectrum for 10 mM solution benzene-appended CB[6] (dissolved in deionized water). a) Z-spectrum produced using a 16 x 30 sinusoidal wave pulse with a 1530° flip angle and a 2 ppm step; signal depletion is approximately 70% at -80 ppm. b) 1D spectrum with gas-phase and dissolved-phase ^{129}Xe peaks at 0 ppm and 200 ppm, respectively. c) Ball-and-stick figure of benzene-appended CB[6], the chosen ^{129}Xe host molecule for figure 3.7.

3.4 Discussion

In this work, we surveyed pseudo-rotaxanes to determine their ability to conjugate to affinity tags and still exhibit a HyperCEST effect. We further optimized the HyperCEST pulse sequences to enhance detectability, such as using a sinusoidal wave pulse, which has a narrower bandwidth than a 3-lobe sinc pulse. However, most pseudorotaxanes investigated did not display a HyperCEST effect, which is possibly due to the xenon's fast exchange rate. Accordingly, the xenon atoms may have had very little to no hydrophobic effect with the cage molecules, leading to a low binding constant for xenon. In this manner, there was likely an insufficient number of encapsulated xenon atoms upon the application of an on-resonance saturation pulse, resulting in an insufficient development of a free-dissolved, depolarized ^{129}Xe pool, a necessary component in HyperCEST.

It is likely that the pseudorotaxanes in this study deviated from 1:1 host-guest complex,[74] leading to a diminished HyperCEST effect. Additionally, for cucurbituril-based pseudorotaxanes, the volume of their internal cavities need to be between 164 and 176 Å^3 to facilitate optimum xenon-cage interaction.[74] Hence, the alkyl chain for cucurbituril-based pseudorotaxanes may have occupied a large portion of the internal cavity so that its resulting volume is less than 164 Å^3. As a result, the xenon atoms could not become encapsulated by the cage molecule. Furthermore, the lack of HyperCEST effect may be due to the stoppers on the alkyl chain that was threaded through the pseudorotaxane. Some stoppers have benzene rings, which may sterically hinder the xenon atom from entering the cage's internal cavity. Nonetheless, this anomaly can be used to create a functionalized xenon biosensor, such that a HyperCEST effect is not displayed until the alkyl chain is cleaved by an enzyme or change in pH, which releases the cage molecule to encapsulate the ^{129}Xe atom. Finbloom *et al*. already demonstrated this effect

using CB[6], which could not encapsulate ^{129}Xe because it was threaded with a bulky alkyl chain. However, upon cleavage of the alkyl chain, the CB[6] was released, which encapsulated ^{129}Xe; hence, a HyperCEST effect was exhibited.[80]

Previous research demonstrated the reduction in the HyperCEST effect for CB[6] bound to triazole-diammonium guests with no bulky stoppers or additional axle components because an equilibrium complex may have formed between unbound and triazole-bound CB[6].[81] Therefore, it is possible that an equilibrium complex may have also been established between bound and unbound γ-CD, such as spermidine-bound γ-CD versus unbound γ-CD (refer to figure 3.8 for the diagram; refer to figure A-15 for z-spectra pertaining to γ-CD and spermidine). Hence, unbound y-CD would not have the proper volume to encapsulate ^{129}Xe, resulting in a reduced HyperCEST effect.

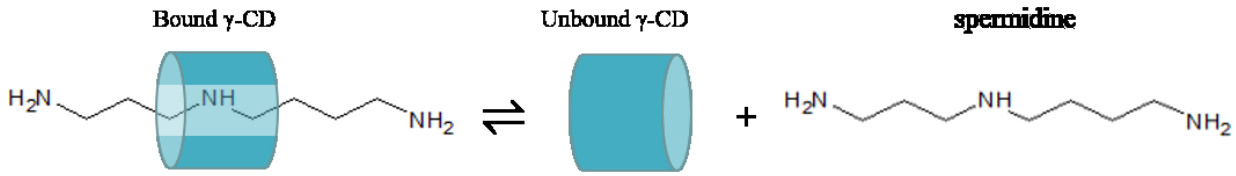

Figure 3.8: Equilibrium between spermidine-bound γ-CD versus unbound γ-CD.

The ^{129}Xe supramolecular cages which exhibited the greatest HyperCEST effect were CB[6] (figure 3.6) and benzene-appended CB[6] (figure 3.7). This result confirms previous research showing that CB[6] is a highly sensitive ^{129}Xe contrast agent. Additionally, the cage-bound peak (at -72 ppm) for CB[6] (figure 3.6a) is more broad than the cage-bound peak (at -80 ppm) for benzene-appended CB[6] (figure 3.7a). This phenomenon is likely attributed to the type of pulse used to acquire the z-spectra for CB[6] and benzene-appended CB[6], which, respectively, involved a 16 x 30 3-lobe sinc pulse and a 16 x 30 sinusoidal wave pulse. In this manner, the sinusoidal wave pulse has a narrower bandwidth than the 3-lobe sinc pulse, and therefore can, almost exclusively, selectively saturate the ^{129}Xe atom inside of its cage. The

pseudo-rotaxane in figure 3.5 may also exhibit a HyperCEST effect; however, the signal depletion was only 20 percent at -40 ppm.

One limitation of this study is that most pseudorotaxane samples are non-polar, which does not easily translate well as an *in vivo* application. Another limitation is the use of a 3T MRI clinical scanner, which may not provide data with very high resolution compared to data from a high field NMR spectrophotometer, which is frequently used in researching functionalized ^{129}Xe biosensor's HyperCEST effect.

3.5 Conclusion

In conclusion, the xenon supramolecular cage molecules that exhibited a large HyperCEST effect were CB[6] (shown in figure 3.6) and benzene-appended CB[6] (shown in figure 3.7). Conversely, most pseudorotaxanes in this project did not exhibit a HyperCEST effect (refer to appendix A for these results), either because the exchange rate for xenon was too fast, the stoppers on the alkyl chain prevented xenon from accessing the internal cavity, or an equilibrium was established between the cage molecule and alkyl chain (such as unbound γ-CD versus spermidine-bound γ-CD).

3.6 Future Work

Future work should focus on attaching polar groups to the pseudo-rotaxane chemical structure to enhance its water-solubility, which allows prospective use for *in vivo* studies. In the future, attempts should be made on testing the *in vivo*, HyperCEST effect of functionalized ^{129}Xe biosensors that are already published in literature.

4. Detecting the HyperCEST Effect in a Sprague-Dawley Rat's Lungs using CB[6]

4.1 Introduction

The most common type of lung cancer, non-small cell lung cancer (NSCLC), has a very low survival rate. Although early detection could significantly improve the survival rate of NSCLC, it is most often found at an advanced stage, at which treatment is relatively ineffective.[1] Current detection techniques for NSCLC include chest x-ray and positron emission tomography, which require ionizing radiation. Another detection technique is computed tomography (CT), which can identify lung nodules of early stage lung cancer. However, most of these lung nodules identified via CT are benign.[82] Therefore, a follow-up procedure, such as bronchoscopy or a biopsy, is usually required to confirm the malignancy risk of these lung nodules.[82] Bronchoscopy and biopsies, however, are invasive procedures. It is therefore feasible to propose non-invasive detection techniques, such as HP ^{129}Xe MRI and HyperCEST, to determine their capacity in detecting early stage NSCLC.

Although MRI is a non-invasive imaging modality with high spatial resolution,[83] it is still difficult to conduct molecular imaging using MRI. Lung images produced via ^{1}H MRI do not provide pertinent anatomical and physiological information. To circumvent this limitation, MRI can be combined with HP ^{129}Xe, whose signal in the lungs is approximately five orders of magnitude higher than thermally polarized ^{129}Xe MRI.[84] Previous clinical studies with HP ^{129}Xe MRI demonstrated its ability to identify pathological sites within the lungs. The ^{129}Xe atoms themselves, however, cannot target disease biomarkers. Nonetheless, HP ^{129}Xe atoms can be combined with functionalized ^{129}Xe biosensors and HyperCEST to detect disease biomarkers. The signal from HyperCEST is usually 10^3 higher than HP dissolved-phase ^{129}Xe;[85] hence, it is a highly sensitive detection technique. Chambers *et al.* already demonstrated the HyperCEST effect using a functionalized ^{129}Xe biosensor that detects the presence of carbonic anhydrases I

and II, which are associated with tumour formation and polycystic kidney disease.[86,87] It is therefore feasible to investigate the possibility of using HyperCEST, along with a functionalized xenon biosensor, to detect early stage NSCLC.

Previous research work on HyperCEST referenced the ^{129}Xe signal in the dissolved phase, which, after the application of an on-resonance pulse, results in a reduction in dissolved-phase ^{129}Xe signal. However, this project references the ^{129}Xe signal in the gas phase, which has a greater SNR than its dissolved-phase counterpart (within the lungs). It has a greater SNR since approximately 98% of HP ^{129}Xe resides in the alveoli, while only 2% HP ^{129}Xe resides in the blood and parenchyma.[26] Hence, in this project, we attempted to determine the reduction in gas-phase ^{129}Xe signal after the application of an on-resonance saturation pulse, whose frequency is the same as that of encapsulated ^{129}Xe while residing in the blood.

The purpose of this study is to determine the HyperCEST effect in the lungs (or alveoli) of a healthy Sprague-Dawley rat using CB[6] as a xenon supramolecular cage in reference to the gas phase ^{129}Xe (which matches the second objective in chapter 2). This project has the potential to use HyperCEST along with functionalized CB[6] to detect NSCLC. CB[6] was chosen because Hane *et al.* already demonstrated its HyperCEST effect within the vasculature of a Sprague-Dawley rat.[67]

4.2 Materials and Methods

To create the 10 mM CB[6] solution, 0.0990 g CB[6] (Sigma Aldrich, St. Louis, USA) was dissolved in 9.9 mL 1X phosphate buffer saline (PBS) with pH 7.2. The mixture was heated to approximately 50 °C and stirred to facilitate dissolution of CB[6] into PBS. The solution was cooled to room temperature.

All animal procedures were approved by LU and TBRHRI research ethics board. Sprague-Dawley rats (male, n = 8, ages 6 to 12 months) (Charles River, QC), which weighed between 350 to 550 g. Each rat was anesthetised with isoflurane at three litres per minute, until they exhibited no corneal, palpebral, and pupillary reflexes. Each rat received a subcutaneous injection of buprenorphine with a dose of 0.1 mg/kg body weight. Following induction of anesthesia, each rat received an intravenous perfusion of propofol (46 mg/kg/hr) by inserting a catheter into one of the tail veins. To inject the CB[6] solution into the rat, an additional tail vein catheter was inserted into a different tail vein. The neck of the rat was subjected to a midline incision to locate the trachea. A 1 mm incision was made into the trachea to insert an endotracheal catheter into the trachea. The neck was closed with sutures. The endotracheal catheter was hooked up to a custom-made ventilator, which had a breathing rate of 60 breaths per minute and a tidal volume of 5 mL. 3 mL of 10 mM CB[6] solution was injected into the rat using the tail vein catheter over a 2-minute interval. The rat was then placed inside a dual-tuned ($^{1}H/^{129}Xe$), custom-made, bird-cage coil. Following the collection of MR spectra and images, the rat was euthanized with pentobarbital.

All MR images were acquired using a Philips Achieva 3T clinical scanner. Xenon was polarized to 30% using a Xemed polarizer (Xemed, Durham, NH) and dispensed in a 1L Tedlar bag. The Tedlar bag was placed in the ventilator so that xenon could be dispensed to the rat. Before each MR acquisition, there was a 5-second wash-in period. During the MR acquisition, a mixture of 80% xenon and 20% oxygen was continuously administered to the rat 6 seconds following the commencement of xenon ventilation. A series of 2D FFE on-resonance (+4,540 Hz) and off-resonance coronal lung images (-4,505 Hz) were collected with respect to the gas phase resonance. All images were collected with FOV 150 x 150 mm, matrix size 64 x 64, voxel

size 2.34 x 2.34 x 300 mm, flip angle of 10°, minimum TR = 167 ms, TE = 1.67 ms. The actual TR varied from 5,275 to 10,275 ms. The images were collected in the following pattern: off-resonance, on-resonance, on-resonance, and off-resonance.

The SNR for each off-resonance and each on-resonance MR image was determined by using a custom-made Matlab Script. Another custom-made Matlab script was used to generate saturation maps. The off-resonance image was subtracted pixel-by-pixel from the on-resonance image and then divided pixel-by-pixel by the off-resonance image.

4.3 Results

A series of saturation maps were generated to depict the HyperCEST effect in the lungs of a Sprague-Dawley rat. Figures 4.1 and 4.2 show an off-resonance image, an on-resonance image, and a saturation map, respectively, in panels a), b) and c). Figures 4.3 to 4.6 show saturation maps. Each saturation map from each figure was generated from a different Sprague-Dawley rat. Figure 4.3 involves a TR = 5 s and a 16 x 30 3-lobe sinc pulse. Figure 4.3 showed positive signal depletion in the lungs. Figure 4.3 was also averaged for four off-resonance and four on-resonance images. Figure 4.5 also involves a 16 x 30 3-lobe sinc pulse and TR = 6 s. However, figure 4.5 also shows positive and negative signal depletion, respectively, in the interior and superior parts of the lungs. Figure 4.4 involved a 32 x 30 3-lobe sinc pulse, which showed greater signal depletion in the lungs than that of figure 4.3. Figure 4.6 involves a TR = 6 s and a 16 x 30 3-lobe sinc pulse. The saturation map for figure 4.6 shows negative signal depletion within the lungs. Refer to Appendix B for additional on-resonance images, off-resonance images, and saturation maps that pertain to this study.

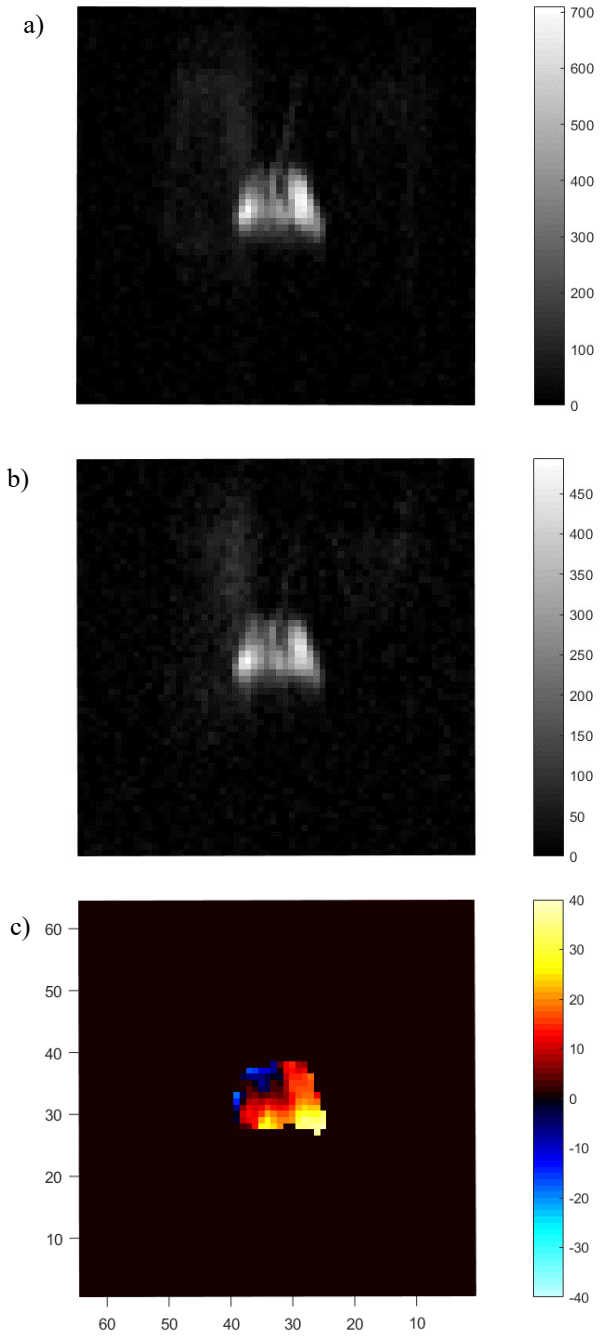

Figure 4.1: a) Off-resonance image with SNR = 35.22; b) On-resonance image with SNR = 31.05; Both a) and b) were produced using a 16 x 30 3-lobe sinc pulse, TR = 5 s, flip angle = 15°, and pulse angle = 140°. c) Saturation map.

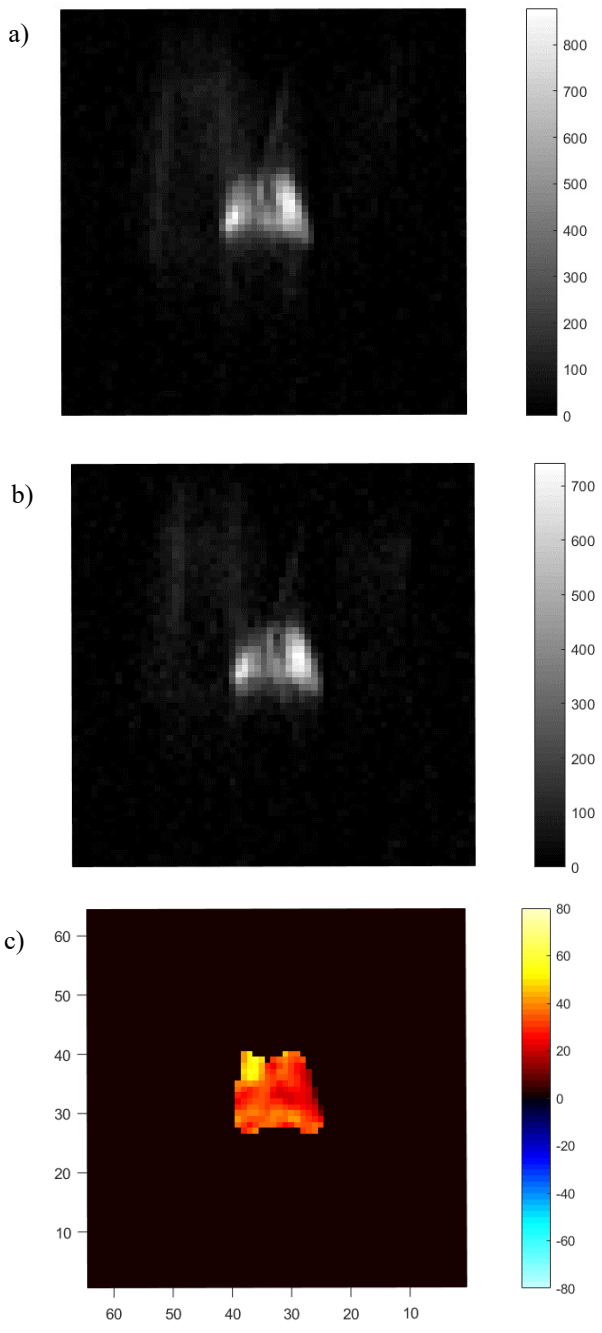

Figure 4.2: a) Off-resonance image with SNR = 59.38; b) On-resonance image with SNR = 39.34. Both a) and b) were produced using a 16 x 30 3-lobe sinc pulse, TR = 5s, flip angle = 15°, and pulse angle =140°. c) Saturation map.

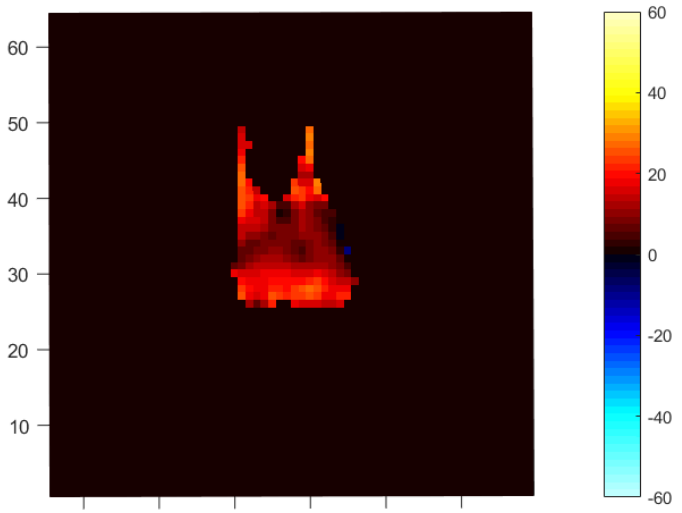

Figure 4.3: Saturation map averaged for 4 off-resonance and 4 on-resonance images, which involved a 16 x 30 3-lobe sinc pulse, TR = 5 s, flip angle = 15°, and pulse angle = 140°. This saturation map shows positive signal depletion in the lungs.

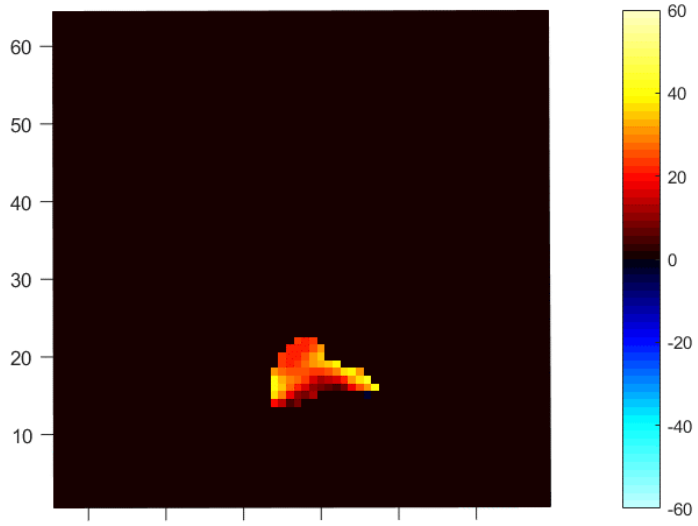

Figure 4.4: Saturation map averaged for 2 off-resonance and 2 on-resonance images. This saturation involved using a 32 x 30 3-lobe sinc pulse with a TR =5 s, flip angle = 10° and pulse angle = 140°. This saturation map shows positive signal depletion within the same set of lungs.

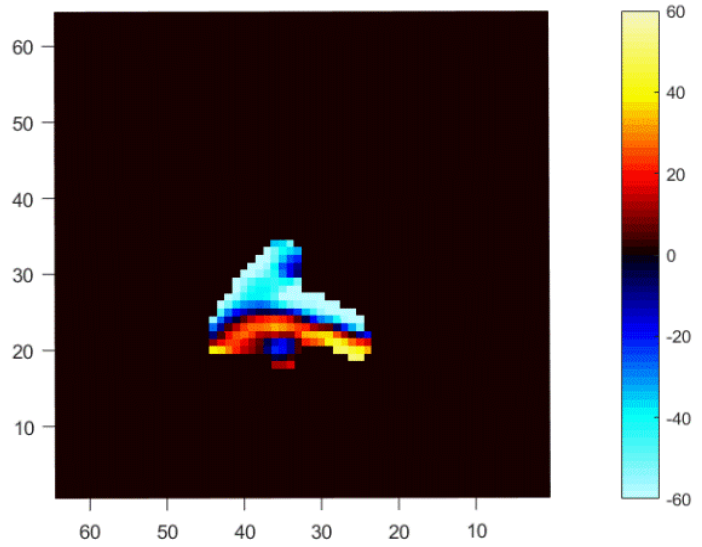

Figure 4.5: Saturation map averaged for 6 off-resonance and 6 on-resonance images. This saturation map involved using a 16 x 30 3-lobe sinc pulse with a TR = 5 s, flip angle = 15° and pulse angle = 140°. This saturation map shows positive and negative signal depletion within the same set of lungs.

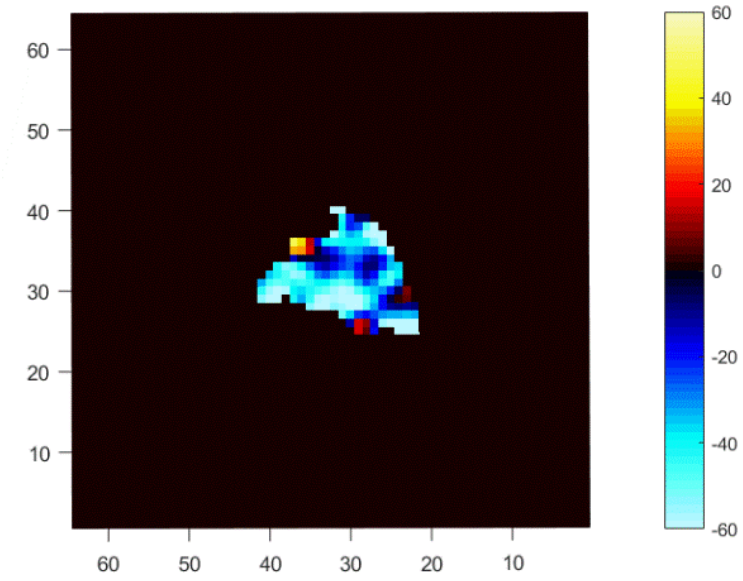

Figure 4.6: Saturation map averaged for 2 off-resonance and 2 on-resonance images. This saturation map was produced using a 16 x 30 3-lobe sinc pulse, TR = 6s, flip angle = 10°, and pulse angle =140°. This saturation map shows negative signal depletion within the same set of lungs.

4.4 Discussion

Some saturation maps show positive signal depletion occurring within the lungs (such as figure 4.3 and 4.4). Other saturation maps show negative depletion within the lungs (such as figure 4.6). There are other saturation maps, such as figure 4.5, which show areas with positive and negative signal depletion occurring within the same set of lungs. In addition, a change in TR from 5 s (figure 4.5) to 6 s (figure 4.6) did not improve the HyperCEST effect within the lungs.

The variation in results may be due to non-functionalization of CB[6], resulting in a changing concentration of CB[6] within the lungs. Further, there are many components within the lungs, such as parenchyma, alveoli, and blood vessels; hence, ^{129}Xe atoms have to exchange in and out of the alveoli to be encapsulated by CB[6], which is located mainly in the blood. As a result, this anomaly may result in insufficient development of a depolarized ^{129}Xe pool, which is a necessary component in HyperCEST. The variation in results, however, may also be due to a weak HyperCEST depletion, where any positive HyperCEST signal results from random fluctuations.

Saturation maps that show positive signal depletion could plausibly indicate a HyperCEST effect. Positive signal depletion means that the signal resulting from an off-resonance pulse is greater than the signal from an on-resonance pulse. Previous research conducted by Hane *et al.* already demonstrated the *in vivo* HyperCEST effect of CB[6] within the vasculature of different organs in a Sprague-Dawley rat, including the lungs.[67] Conversely, it is possible that the ^{129}Xe atoms may have exchanged in and out of deoxygenated blood, whose T1 relaxation rate is 4 s.[42] This plausible event may also contribute to the development of a depolarized ^{129}Xe pool, and therefore result in a positive signal depletion occurring within the lungs.

One limitation with this particular ^{129}Xe host molecule is the difficulty in functionalizing CB[6] with an antibody because of its highly stable structure.[79] Another limitation is that this study involved a 3T MRI clinical scanner, which provides less spatial resolution than a 11T MRI scanner (these types of scanners are specifically designed for animals). Additionally, the multiple components within the lungs present another limitation, where ^{129}Xe atoms have to move from the alveoli to the blood to be encapsulated by CB[6].

Rousseau *et al.* produced a functionalized ^{129}Xe biosensor that detects the EGFR protein upregulated in NSCLC.[88] This biosensor consists of cryptophane-a conjugated to an EGFR antibody. Some limitations with this biosensor, however, include the production of cryptophane-a, which involves a difficult, multi-step synthesis, and a low yield. Also, the binding constant for cryptophane-A is 850 M^{-1}, which is low compared to CB[6] (2500 M^{-1}).[65] Conversely, it is easier to attach an antibody to cryptophane-a than to CB[6].

4.5 Conclusion

In conclusion, saturation maps with positive signal depletion may show HyperCEST effect. On the other hand, some saturation maps showed negative depletion, while other saturation maps showed both positive and negative saturation maps in the lungs. Therefore, there is a large variation in results.

4.6 Future Work

Future work should focus on the optimization of ^{129}Xe biosensors for *in vivo* applications. Although Rousseau *et al.* developed a functionalized ^{129}Xe biosensor for detecting EGFR protein associated with NSCLC,[88] it involves cryptophane-A, which is associated with a multi-step synthesis and a low yield. Future work should also consider developing the same type of biosensor to track different cancers. For example, NSCLC and colon cancer are associated with development and upregulation of the EGFR protein.[70,89] Therefore, the same type of biosensor may be used to detect the EGFR protein for both types of cancer.

5. HP ^{129}Xe Functional Magnetic Resonance Imaging in the Brain of Healthy Volunteers

5.1 Introduction

Proton BOLD fMRI is largely used within the field of neuroscience to depict areas of high brain activity within humans. It is based on the correlation between neuronal activity and blood perfusion, where areas with high neuronal activity require increased amount of ATP and glucose to maintain its activity, and therefore undergo greater oxygenated blood perfusion than areas with low neuronal activity.[6] This imaging modality, however, requires many signal averages to reach statistical significance; also, it does not have the capacity to elucidate underlying neurologic mechanisms.[90] The signal enhancement for proton BOLD fMRI is fairly low.

The SNR is likely to be higher for HP ^{129}Xe fMRI than proton BOLD fMRI since the ^{129}Xe atom can serve as a perfusion tracer,[39] where its signal is directly correlated with blood flow in activated brain regions. Additionally, the partition coefficient of ^{129}Xe, which is 0.15, allows for its rapid transportation through the bloodstream to the brain.[91] The chemical shift for ^{129}Xe is different in oxygenated and deoxygenated blood, which allows for local mapping of pO_2. ^{129}Xe also has different T1 values for oxygenated and deoxygenated blood,[42] and thereby allows for the differentiation between brain regions that have high and low levels of oxygenation. Mazzanti *et al.* previously demonstrated a HP ^{129}Xe fMRI signal in areas of the brain associated with pain response due to capsaicin injection in an animal model.[41]

The objective of this project was to detect an HP ^{129}Xe fMRI signal within the visual cortex of healthy volunteers. We assumed that areas with increased blood perfusion experience greater concentration of ^{129}Xe than areas with low blood perfusion. The T1 relaxation time for ^{129}Xe is higher in oxygenated than deoxygenated blood. We additionally assumed therefore that

signal intensity will depend on blood oxygenation levels. HP ^{129}Xe fMRI has the potential to provide a more refined signal for activated brain regions than proton BOLD fMRI.

5.2 Materials and Methods

All procedures were reviewed and approved by the LU and TBRHRI Research Ethics Boards. All volunteers provided written informed consent. Brain imaging was performed in 9 healthy volunteers (n = 9, male & female, ages 24-64) using a 3T Philips Achieva MRI, equipped with a ^{129}Xe/^{1}H dual tuned head-coil (Clinical MR Solutions, Brookfield, WI). Each volunteer inhaled 1 L of enriched (84%) ^{129}Xe (polarized to 26-32%) and held their breath for 20s. The ^{129}Xe fMRI were acquired via 2D fast field echo (FFE) pulse sequence. Imaging parameters for HP ^{129}Xe fMRI were FOV = 250 mm x 250 mm, matrix = 32x32, TR/TE = 250 ms/0.84 ms, FA = 12°. The volunteer was then asked to conduct a visual task, which involved looking at a checkerboard for 20 s followed by looking at a blank screen for another 20 s; the visual task was 3 min and 20 s during the proton BOLD fMRI acquisition. ^{129}Xe MR imaging during the stimulus/task was conducted identically to the baseline imaging. ^{1}H MRI were acquired using a turbo spin echo sequence utilizing the following parameters: FOV = 250 mm x 250 mm, matrix = 256x256, TR/TE = 3 s/80 ms, FA = 90°. ^{1}H MRI data were analyzed using statistical parametric mapping 12 (spm12).[92] ^{129}Xe MRI were processed using a custom Matlab (MathWorks, Natick, MA, USA) script. Xenon images were zero-filled to 256x256, registered to the center of the field of view. The baseline ^{129}Xe MR image was subtracted from the stimulus/task ^{129}Xe MR image to create a ^{129}Xe fMRI map. The results in this section include key results for this project. Refer to Appendix C for additional data that pertain to this study.

5.3 Results

Only one dataset (figure 5.1) showed enhancement within the visual cortex of a healthy volunteer for both proton BOLD and ^{129}Xe fMRI. Figures 5.2 and 5.3 showed very little to no stimulation in the visual cortex. The other proton BOLD fMRI images found in Appendix C also did not show stimulated activity in the visual cortex.

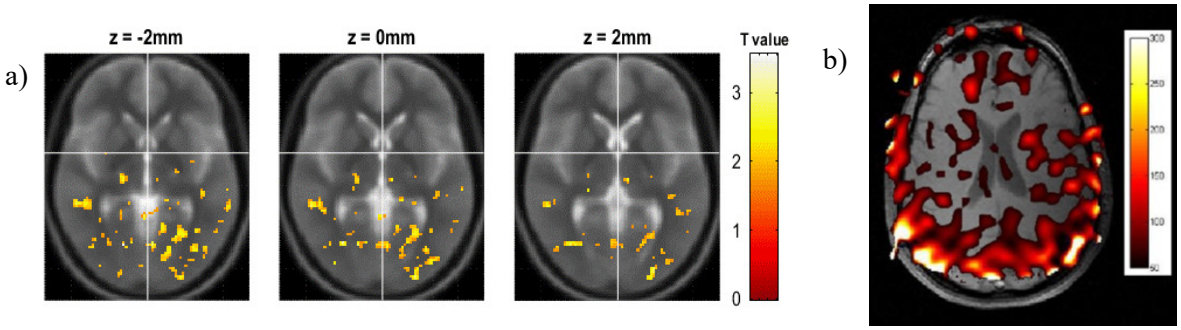

Figure 5.1: a) Three proton, BOLD fMRI slices. b) One, ^{129}Xe BOLD fMRI image (produced by Dr. Francis Hane). Both a) and b) show signal enhancement within the visual cortex of the same healthy volunteer.

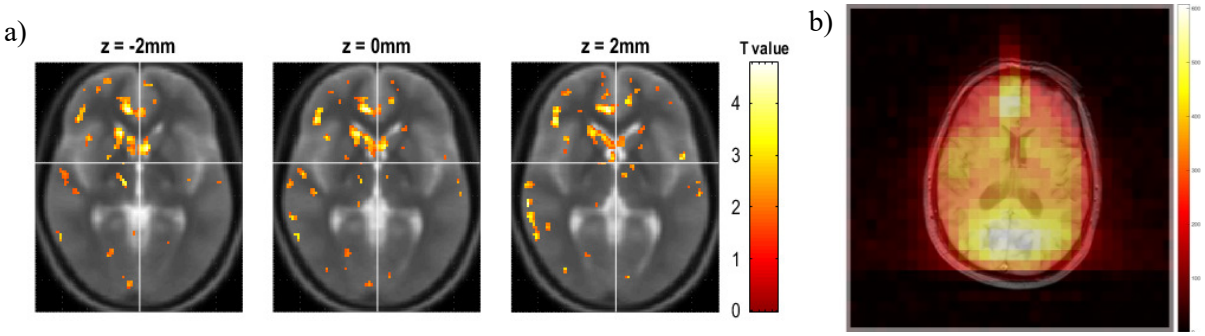

Figure 5.2: a) Three proton, BOLD fMRI slices that indicates very little ^{1}H BOLD fMRI signal enhancement within the healthy volunteer's visual cortex. b) ^{129}Xe BOLD fMRI imaging showing very small signal enhancement in the visual cortex of the healthy volunteer.

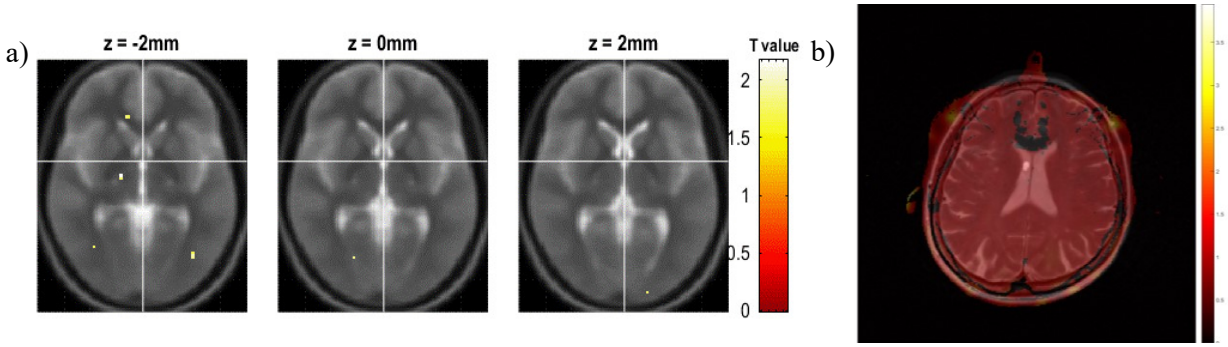

Figure 5.3: a) Three proton, BOLD fMRI slices. b) One ^{129}Xe fMRI image. Both a) and b) show almost no signal enhancement within the visual cortex of a healthy volunteer.

5.4 Discussion

Only one proton BOLD (figure 5.1a) and its corresponding ^{129}Xe fMRI (figure 5.1b) signal maps showed signal enhancement almost exclusively within the visual cortex of a healthy volunteer. Conversely, it is difficult to determine whether signal enhancement for ^{129}Xe fMRI shown in figure 5.1b is an artifact or an actual signal of the stimulated brain region. The ^{129}Xe fMRI image in figure 5.2b also shows some signal enhancement within the visual cortex; however, it also shows signal enhancement within the frontal lobe.

It is possible that the ^{129}Xe fMRI is obscured by noise for figures 5.2 b and 5.3 b. In contrast, Mazzanti *et al.* showed ^{129}Xe fMRI signal of pain response within an animal model using a 2D chemical shift imaging (CSI) pulse sequence, which provides a higher SNR than the pulse sequence used in our study, which is a 2D fast field echo (FFE) sequence.[41]

The principle behind ^{129}Xe fMRI is that ^{129}Xe atoms act as a perfusion tracer, and therefore have the potential to provide a more refined signal than proton BOLD fMRI. However, only two percent of HP ^{129}Xe dissolves in the lung tissue and blood. As a result, the lack of signal within the visual cortex may result from the small concentration of ^{129}Xe that can travel to the brain. Furthermore, the healthy volunteers may not have the same breath-hold capacity, which should be easily quantifiable in the future. Otherwise, different breath-hold capacity results in different xenon concentrations within the brain. Therefore, the lack of a refined ^{129}Xe signal may be due to different breath-hold capacity for each volunteer.

The proton BOLD fMRI images did not always show signal enhancement within the visual cortex of healthy volunteers, as shown in panel a for figures 5.2 and 5.3. One of the drawbacks with this imaging modality is that signal enhancement relies on brain perfusion within activated brain regions. Hence, a large signal that is occurring in one activated brain region can

alter the signal for brain regions with small activation.[93] The lack of signal enhancement within the visual cortex is also likely attributed to the task timing design for proton BOLD fMRI, which may not have provided enough perfusion of oxygenated blood within the visual cortex of healthy volunteers.

One limitation to this study is that the task timing design for the ^{129}Xe fMRI data was different from that of proton BOLD fMRI. The ^{129}Xe fMRI task timing design consisted of one 20 s resting period followed by one 20 s visual stimulus task, which was designed to consider the ^{129}Xe T1 relaxation time. The task timing design for the proton BOLD fMRI acquisition involved repetitions of the resting and visual stimulus tasks. Additionally, this study was based on the assumption that localized ^{129}Xe signal is due to increased perfusion of ^{129}Xe within stimulated brain region. Consequently, this task timing design for ^{129}Xe fMRI may not have provided enough ^{129}Xe perfusion within the stimulated brain region, resulting in a lack of signal.

5.5 Conclusion

According to the fMRI data, the HP ^{129}Xe fMRI technique did not always spatially localize ^{129}Xe within stimulated brain regions. However, the HP ^{129}Xe fMRI technique is still in its infancy. Future work should focus on collaboration with neurophysiologists to establish the most optimum task timing design suitable for both proton BOLD and ^{129}Xe fMRI.

References

1. Hashemi, R. H., Bradley, W. & Lisanti, C. *MRI: The Basics*. (Lippincott Williams and Wilkins, 2010).

2. Gossuin, Y., Hocq, A., Gillis, P. & Vuong, Q. L. Physics of magnetic resonance imaging: from spin to pixel. *J. Phys. D Appl. Phys* **43,** 213001–213015 (2010).

3. Goodson, B. M. Nuclear Magnetic Resonance of Laser-Polarized Noble Gases in Molecules , Materials , and Organisms. *J. Magn. Reson.* **155,** 157–216 (2002).

4. Nacher, P. Magnetic Resonance Imaging. *Spin* 159–193 (1999).

5. Trip, S. A. & Miller, D. H. Imaging in Multiple Sclerosis. *J Neurol Neurosurg Psychiatry* **76,** iii11-iii18 (2005).

6. Ogawa, S., Menon, R., Kim, S.-G. & Ugurbil, K. On the Characteristics of functional Magnetic Resonance Imaging of the Brain. *Annu. Rev. Biophys. Biomol. Struct.* **27,** 447–474 (1998).

7. Glover, G. H. Overview of functional magnetic resonance imaging. *Neurosurg Clin N Am* **22,** 133–139 (2011).

8. Ogawa, S., Lee, T.-M., Nayak, A. S. A. & Glyn, P. Oxygenation-Sensitive Contrast in Magnetic Resonance Image of Rodent Brain at High Magnetic Fields. *Magn Reson Med* **14,** 68–78 (1990).

9. Huettel, S. A., Song, A. W. & McCarthy, G. *Functional Magnetic Resonance Imaging*. (Sinauer Associates, Inc, 2004).

10. Hatabu, H. *et al.* MR imaging of pulmonary parenchyma with a half-Fourier single-shot turbo spin-echo (HASTE) sequence. *Eur J Radiol* **29,** 152–159 (1999).

11. Roos, J. E., McAdams, H. P., Kaushik, S. S. & Driehuys, B. Hyperpolarized Gas MRI: Technique and Applications. *Magn Reson Imaging Clin N Am* **23,** 217–229 (2015).

12. Goodson, B. M. *et al.* in *Encyclopedia of Analytical Science, 3rd Edition* 1–14 (Elsevier Inc., 2018). doi:10.1016/B978-0-12-409547-2.14072-7

13. Chen, X. J. *et al.* Spatially Resolved Measurements of Hyperpolarized Gas Properties in the Lung. *Magn Reson Med* **42,** 721–728 (1999).

14. Walker, T. G. & Happer, W. Spin-exchange optical pumping of noble-gas nuclei. *Rev Mod Phys* **69,** 629–642 (1997).

15. Witte, C. & Schröder, L. NMR of hyperpolarised probes. *NMR Biomed* **26,** 788–802 (2012).

16. Oros, A.-M. & Shah, N. J. Hyperpolarized xenon in NMR and MRI. *Phys. Med. Biol.* **49,** R105–R153 (2004).

17. Lilburn, D. M. L., Pavlovskaya, G. E. & Meersmann, T. Perspectives of hyperpolarized noble gas MRI beyond 3He. *J. Magn. Reson.* **229,** 173–186 (2013).

18. Albert, M. *et al.* Biological magnetic resonance imaging using laser-polarized 129Xe.

Nature **370,** 199–200 (1994).

19. Couch, M. J. *et al.* Inert fluorinated gas MRI: a new pulmonary imaging modality. *NMR Biomed.* **27,** 1525–1534 (2014).

20. Ruppert, K. Biomedical imaging with hyperpolarized noble gases. *Rep. Prog. Phys.* **77,** 116701–116734 (2014).

21. Ebner, L. *et al.* The role of hyperpolarized 129xenon in MR imaging of pulmonary function. *Eur. J. Radiol.* **86,** 343–352 (2016).

22. Saam, B., Happer, W. & Middleton, H. Nuclear relaxation of 3He in the presence of O2. *Phys Rev A* **52,** 862–865 (1995).

23. Jameson, C. J. *et al.* Nuclear spin relaxation by intermolecular magnetic dipole coupling in the gas phase 129Xe in Oxygen. *J Chem Phys* **89,** 4074–4081 (1988).

24. Cleveland, Z. I. *et al.* Chronic Obstructive Pulmonary Disease: Safety and Tolerability of Hyperpolarized 129 Xe MR Imaging in Healthy Volunteers and Patients. *Radiology* **262,** 279–289 (2012).

25. Stewart, N. J., Norquay, G., Griffiths, P. D. & Wild, J. M. Feasibility of Human Lung Ventilation Imaging Using Highly Polarized Naturally Abundant Xenon and Optimized Three-Dimensional Steady-State Free Precession. *Magn Reson Med* **74,** 346–352 (2015).

26. Mugler, J. P. & Altes, T. A. Hyperpolarized 129Xe MRI of the Human Lung. *J Magn Reson Imaging* **37,** 313–331 (2013).

27. Mugler, J. P. *et al.* MR Imaging and Spectroscopy Using Hyperpolarized 129 Xe Gas: Preliminary Human Results. *Magn Reson Med* **37,** 809–815 (1997).

28. Altes, T. A., Iii, J. P. M., Miller, G. W. & Hersman, F. W. (MXTC) MRI: Initial Results in Animals and Healthy Volunteers. *Magn Reson Med.* **67,** 943–953 (2013).

29. Qing, K. & Ruppert, K. in *Hyperpolarized and Inert Gas MRI* (eds. Hane, F. & Albert, M.) 172–173 (Elsevier, 2017).

30. Dregely, I. *et al.* Hyperpolarized Xenon-129 gas-exchange imaging of lung microstructure: First case studies in subjects with obstructive lung disease. *J Magn Reson Imaging* **33,** 1052–1062 (2011).

31. Cleveland, Z. I. *et al.* Hyperpolarized 129Xe MR Imaging of Alveolar Gas Uptake in Humans. *PLoS One* **5,** 1–8 (2010).

32. Driehuys, B. *et al.* Imaging alveolar – capillary gas transfer using hyperpolarized 129 Xe MRI. *PNAS* **103,** 18278–18283 (2006).

33. Ma, J. Dixon Techniques for Water and Fat Imaging. *J Magn Reson Imaging* **28,** 543–558 (2008).

34. Cleveland, Z. I., Virgincar, R. S., Qi, Y. & Robertson, S. H. 3D MRI of impaired hyperpolarized 129 Xe uptake in a rat model of pulmonary fibrosis. *NMR Biomed* **27,** 1502–1514 (2014).

35. Kauczor, H. U., Surkau, R. & Roberts, T. MRI using hyperpolarized noble gases. *Eur. Radiol* **8,** 820–7 (1998).

36. Zhao, L. *et al.* Gradient-Echo Imaging Considerations for Hyperpolarized 129Xe MR. *J Magn Reson* **113,** 179–183 (1996).

37. Couch, M. J. *et al.* Hyperpolarized and Inert Gas MRI: The Future. *Mol Imaging Biol* **17,** 149–162 (2015).

38. Goto, T. G. *et al.* The blood – gas partition coefficient of xenon may be lower than generally accepted. *Br. J. Anaesth.* **80,** 255–256 (1998).

39. Zhou, X. *et al.* Reinvestigating Hyperpolarized 129Xe longitudinal relaxation time in the rat brain with noise considerations. *NMR Biomed* **21,** 217–225 (2008).

40. Swanson, S. D. *et al.* Brain MRI with Laser-Polarized 129Xe. *Magn Reson Med* **38,** 695–698 (1997).

41. Mazzanti, M. L. *et al.* Distribution of Hyperpolarized Xenon in the Brain Following Sensory Stimulation: Preliminary MRI findings. *PLoS One* **6,** 1–7 (2011).

42. Albert, M. S., Kacher, D. F., Balamore, D., Venkatesh, A. K. & Jolesz, F. A. T1 of 129-Xe in Blood and the Role of Oxygenation. *J. Magn. Reson.* **140,** 264–273 (1999).

43. Wolber, J., Cherubini, A., Leach, M. O. & Bifone, A. On the oxygenation-dependent 129Xe T1 in blood. *NMR Biomed* **13,** 234–237 (2000).

44. Zhou, X. *et al.* MRI of stroke using hyperpolarized 129Xe. *NMR Biomed* **24,** 170–175 (2011).

45. Wakai, A. *et al.* A Method for Measuring the Decay Time of Hyperpolarized 129 Xe Magnetization in Rat Brain without Estimation of RF Flip Angles. *Magn. Reson. Med. Sci.* **4,** 19–25 (2005).

46. Kimura, K., Imai, H., Wakayama, T. & Fujiwara, H. A Simple Method for Quantitative Measurement and Analysis of Hyperpolarized 129Xe Uptake Dynamics in Mouse Brain under Controlled Flow. *Magn Reson Med Sci* **7,** 179–185 (2008).

47. Kilian, W., Seifert, F. & Rinneberg, H. Dynamic NMR Spectroscopy of Hyperpolarized Human Brain Analyzed by an Uptake Model. *Magn Reson Med* **847,** 843–847 (2004).

48. Choquet, P., Duhamel, G., Grillon, E., Leviel, J. & Ziegler, A. Method to Determine In Vivo Relaxation Time T1 of Hyperpolarized Xenon in Rat Brain. *Magn. Reson. Med.* **49,** 1014–1018 (2003).

49. Hane, F. T. *et al.* in *Hyperpolarized and Inert Gas MRI: from Technology to Application in Research and Medicine* (eds. Albert, M. S. & Hane, F. T.) 251–262 (Elsevier, 2017).

50. Kimura, A. *et al.* Improvement of T1 determination of Hyperpolarized 129Xe in mouse brain under controlled-flow. *Magn Reson Med Sci* **3,** 199–205 (2004).

51. Wilson, G. J., Santyr, G. E., Anderson, M. E. & Deluca, P. M. Longitudinal Relaxation Times of 129Xe in Rat Tissue Homogenates at 9.4 T. *Magn Reson Med* **938,** 933–938

(1999).

52. Hane, F. *et al.* in *Hyperpolarized and Inert Gas MRI: From Technology to Application in Research and Medicine* 251–277 (2017).

53. Schröder, L. in *HP and Inert Gas MRI: From Technology to Application in Research and Medicine* (eds. Albert, M. S. & Hane, F. T.) 263–277 (Elsevier Inc., 2017).

54. Schröder, L. Xenon for NMR biosensing - Inert but alert. *Phys. Medica* **29,** 3–16 (2013).

55. Schroder, L., Lowery, T. J., Hilty, C., Wemmer, D. E. & Pines, A. Molecular Imaging Using a Targeted Magnetic Resonance Hyperpolarized Biosensor. *Science (80-.).* **314,** 446–449 (2006).

56. Spence, M. M. *et al.* Functionalized xenon as a biosensor. *PNAS* **98,** 10654–7 (2001).

57. Rose, H. M. *et al.* Development of an antibody-based, modular biosensor for 129 Xe NMR molecular imaging of cells at nanomolar concentrations. *PNAS* **111,** 20–23 (2014).

58. Witte, C. *et al.* Live-cell MRI with xenon Hyper-CEST biosensors targeted to metabolically labeled cell-surface glycans. *Angew. Chemie - Int. Ed.* **54,** 2806–2810 (2015).

59. Kunth, M., Witte, C. & Schröder, L. Quantitative chemical exchange saturation transfer with hyperpolarized nuclei (qHyper-CEST): Sensing xenon-host exchange dynamics and binding affinities by NMR. *J. Chem. Phys.* **141,** (2014).

60. Harel, E., Schröder, L. & Xu, S. Novel detection schemes of nuclear magnetic resonance and magnetic resonance imaging: applications from analytical chemistry to molecular sensors. *Annu. Rev. Anal. Chem.* **1,** 133–63 (2008).

61. Lagona, J., Mukhopadhyay, P., Chakrabarti, S. & Isaacs, L. The Cucurbit[n]uril Family. *Angew. Chem. Int. Ed* **44,** 4844–4870 (2005).

62. Luhmer, M. *et al.* Study of Xenon Binding in Cryptophane-A Using Laser-Induced NMR Polarization Enhancement. *J. Am. Chem. Soc.* **121,** 3502–3512 (1999).

63. Wang, Y. & Dmochowski, I. J. An Expanded Palette of Xenon-129 NMR Biosensors. *Acc. Chem. Res* **49,** 2179–2187 (2016).

64. Nau, W. M., Florea, M. & Assaf, K. I. Deep Inside Cucurbiturils: Physical Properties and Volumes of their Inner Cavity Determine the Hydrophobic Driving Force for Host – Guest Complexation. *Isr. J. Chem.* **51,** 559–577 (2011).

65. Kunth, M., Witte, C., Hennig, A. & Schröder, L. Identification, classification, and signal amplification capabilities of high-turnover gas binding hosts in ultra-sensitive NMR. *Chem. Sci.* **6,** 6069–6075 (2015).

66. Hettiarachchi, G. *et al.* Toxicology and Drug Delivery by Cucurbit[n]uril Type Molecular Containers. *PLoS One* **5,** e10514 (2010).

67. Hane, F. T. *et al.* In vivo detection of cucurbit[6]uril, a hyperpolarized xenon contrast agent for a xenon magnetic resonance imaging biosensor. *Sci. Rep.* **7,** 4–10 (2017).

68. Stage Distribution: Distribution of cases by stage at diagnosis for non-small cell lung cancer – 2013 diagnosis year. *Canadian Partnership against Cancer* Available at: https://www.systemperformance.ca/disease-sites/lung/stage-distribution/#!figures. (Accessed: 14th April 2019)

69. Löfblom, J. *et al.* Affibody molecules: Engineered proteins for therapeutic , diagnostic and biotechnological applications. *FEBS Lett.* **584,** 2670–2680 (2010).

70. Johnson, J. L., Pillai, S. & Chellappan, S. P. Genetic and biochemical alterations in non-small cell lung cancer. *Biochem. Res. Int.* **2012,** 1–18 (2012).

71. Serrao, E. M. & Brindle, K. M. Dynamic nuclear polarisation: The future of imaging in oncology? *Porto Biomed. J.* **2,** 71–75 (2017).

72. Taratula, O., Hill, P. A., Bai, Y., Khan, N. S. & Dmochowski, I. J. Shorter synthesis of trifunctionalized cryptophane - A derivatives. *Org Lett* **13,** 1414–1417 (2011).

73. Caligur, V. Cyclodextrins. *Biofiles* 3.3 32 (2008).

74. Hane, F. T. *et al.* Cyclodextrin-Based Pseudorotaxanes: Easily Conjugatable Scaffolds for Synthesizing Hyperpolarized Xenon-129 Magnetic Resonance Imaging Agents. *ACS Omega* **3,** 677–681 (2018).

75. Song, Y. *et al.* Selective Enhancement of NMR Signals for alpha-Cyclodextrin with Laser-Polarized Xenon. *Angew. Chem. Int. Ed. Engl.* **36,** 2368–2370 (1997).

76. Bartik, K., Luhmer, M., Heyes, S. J., Ottinger, R. & Reisse, J. Probing Molecular Cavities in alpha-Cyclodextrin Solutions by Xenon NMR. *J Magn Reson Ser. B* **109,** 164–168 (1995).

77. Xue, M., Yang, Y., Chi, X., Yan, X. & Huang, F. Development of Pseudorotaxanes and Rotaxanes: From Synthesis to Stimuli-Responsive Motions to Applications. *Chem. Rev* **115,** 7398–7501 (2015).

78. Jean, Y.-M., Whang, D., Kim, J. & Kim, K. A Simple Construction of a Rotaxane and Pseudorotaxane: Syntheses and X-ray Crystal Structures of Cucurbituril Threaded on Substituted Spermine. *Chem. Lett.* **25,** 503–504 (1996).

79. Jon, S. Y. *et al.* Facile Synthesis of Cucurbit[n]uril Derivatives via Direct Functionalization : Expanding Utilization of Cucurbit[n]uril. *JACS* **125,** 10186–10187 (2003).

80. Finbloom, J. A. *et al.* Rotaxane-mediated suppression and activation of cucurbit[6]uril for molecular detection by 129Xe hyperCEST NMR. *Chem. Commun.* **52,** 3119–3122 (2016).

81. Slack, C. C. *et al.* Rotaxane probes for protease detection by129Xe hyperCEST NMR. *Chem. Commun.* **53,** 1076–1079 (2017).

82. Kern, J. Lung Nodules. *National Jewish Health* 1 (2016). Available at: https://www.nationaljewish.org/conditions/lung-nodules. (Accessed: 24th April 2019)

83. Tyszka, J. M., Fraser, S. E. & Jacobs, R. E. Magnetic resonance microscopy: Recent advances and applications. *Curr Opin Biotechnol* **16,** 93–99 (2005).

84. Oros, A. & Shah, N. J. Hyperpolarized xenon in NMR and MRI. *Phys.Med. Biol.* **49,** 105–153 (2004).

85. Schröder, L. *et al.* Temperature response of 129Xe depolarization transfer and its application for ultrasensitive NMR detection. *Phys. Rev. Lett.* **100,** 1–4 (2008).

86. Pastorekova, S., Parkkila, S. & Zavada, J. Tumor-associated Carbonic Anhydrases and Their Clinical Significance. *Adv. Clin. Chem.* **42,** 167–216 (2006).

87. Kaneta, S., Ishizuki, S., Kasahara, M., Nagao, S. & Takahashi, H. Renal Carbonic Anhydrase Activity in DBA/2FG-pcy/pcy Mice with Inherited Polycystic Kidney Disease. *Exp Anim* **48,** 161–169 (1999).

88. Milanole, G. *et al.* Bimodal fluorescence/129Xe NMR probe for molecular imaging and biological inhibition of EGFR in Non-Small Cell Lung Cancer. *Bioorganic Med. Chem.* **25,** 6653–6660 (2017).

89. Ellina, M. *et al.* EGFR and HER2 exert distinct roles on colon cancer cell functional properties and expression of matrix macromolecules. *Biochim. Biophys. Acta* **1840,** 2651–2661 (2014).

90. Farah, M. J. Brain Images, Babies, and Bathwater: Critiquing Critiques of Functional Neuroimaging. *Hastings Cent. Rep.* **44,** 19–30 (2014).

91. Rao, M. R., Stewart, N. J., Griffiths, P. D., Norquay, G. & Wild, J. M. Imaging Human Brain Perfusion with Inhaled Hyperpolarized 129Xe MR Imaging. *Radiology* **286,** 659–665 (2016).

92. Wellcome Trust Centre for Neuroimaging. SPM (Statistical Parametric Mapping) 12 (2014). London: UCL.

93. Scott, S. K. & Wise, R. J. S. Functional imaging and language: A critical guide to methodology and analysis. *Speech Commun.* **41,** 7–21 (2003).

Appendix A: Additional Data for ^{129}Xe Host Molecules

This appendix contains additional z-spectra, 1-D spectra, and structures of different ^{129}Xe host molecules. The results in this appendix include ^{129}Xe host molecules that exhibited very negligible to no HyperCEST effect. The successful results pertaining to ^{129}Xe host molecules were included in chapter 3.

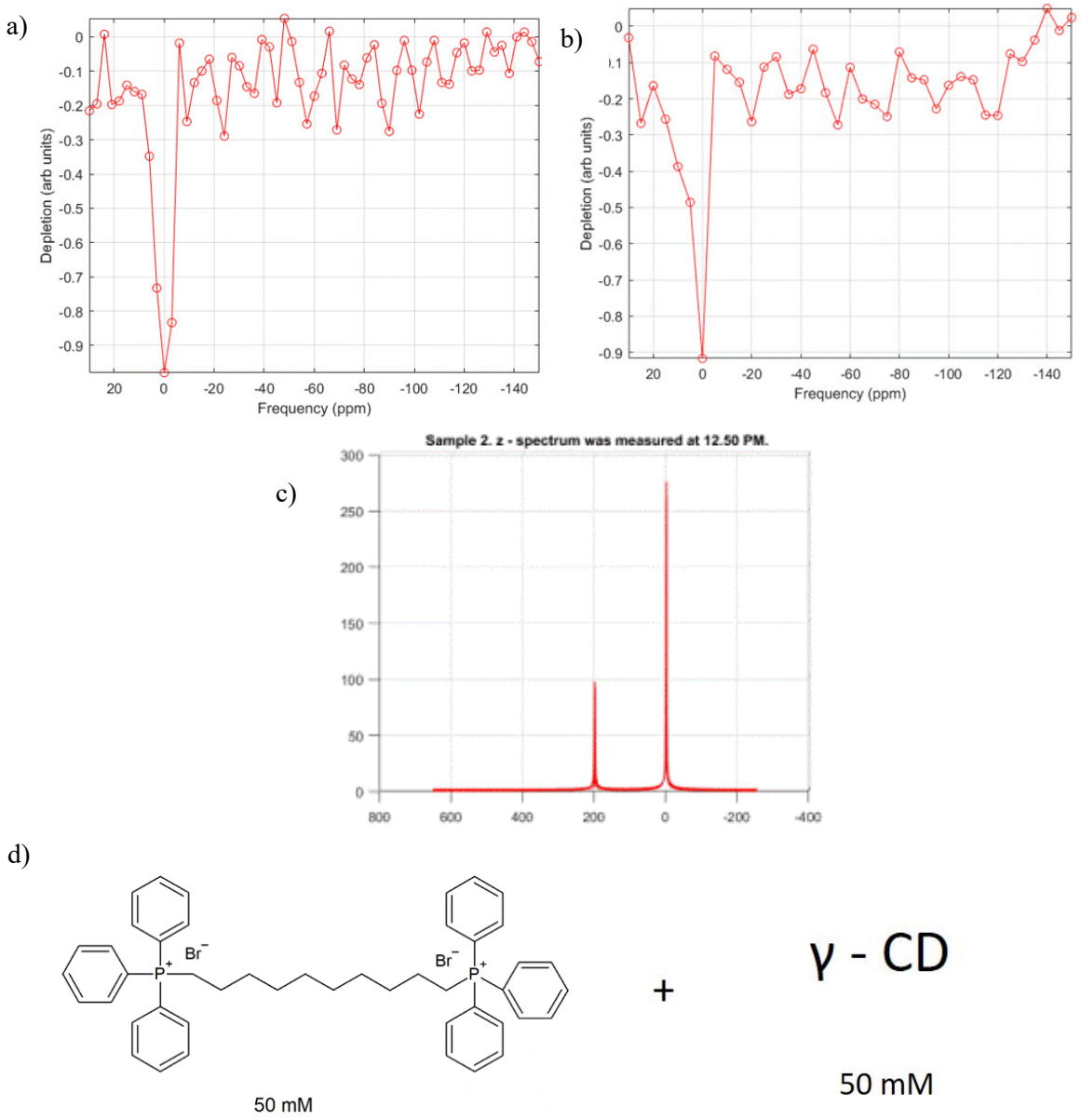

Figure A-1: The ^{129}Xe host molecule is triphenyl(10-triphenylphosphaniumyldecyl)phosphanium tethered through γ-CD. a) Z-spectrum for 16 x 30 3-lobe sinc pulse with a 140° flip angle and TR = 5 s. b) Z-spectrum for 1 x 500 ms sine pulse with a flip angle of 1530°. c) 1D spectrum, where 0 ppm and 196 ppm, respectively, are the ^{129}Xe gas phase and dissolved phase peaks. d) Structure of triphenyl(10-triphenylphosphaniumyldecyl)phosphanium.

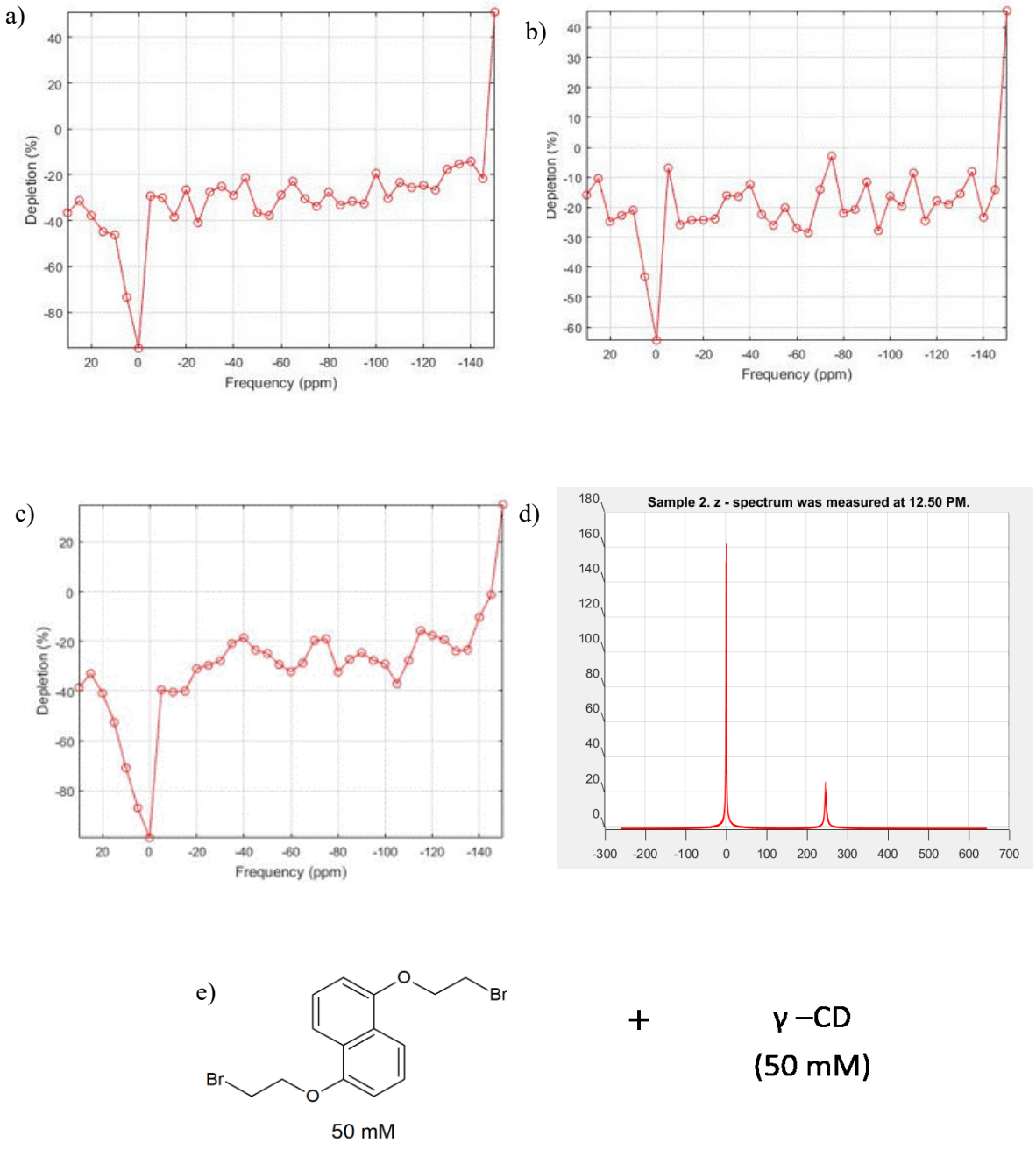

Figure A-2: The ^{129}Xe host molecule is 1,5-bis(2-bromoethoxy)naphthalene tethered through γ-CD. a) Z-spectrum involving a 16 x 30 3-lobe sinc pulse with a 140° flip angle and TR = 5 s. b) Z-spectrum for 1 x 500 ms sine pulse with a 1530° flip angle. c) Z-spectrum involving a 16 x 30 sinusoidal wave pulse with 140° flip angle. d) 1D spectrum that shows 0 ppm and 196 ppm as the ^{129}Xe gas phase peak and dissolved phase peak, respectively. e) Structure of 1,5-bis(2-bromoethoxy)naphthalene. Sample was dissolved in 3 mL of deionized water and 1 mL DMSO.

a)

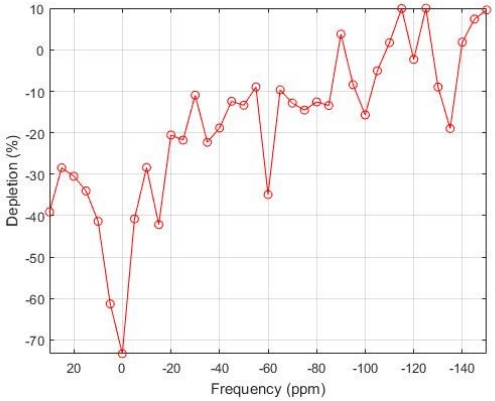

b)

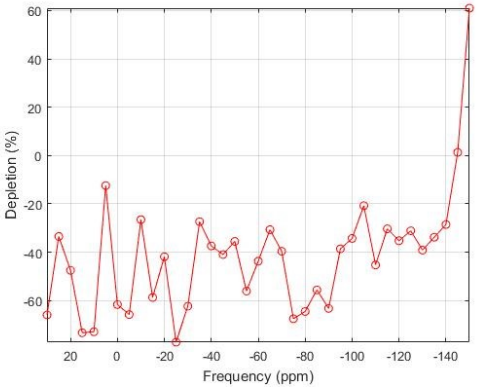

c)

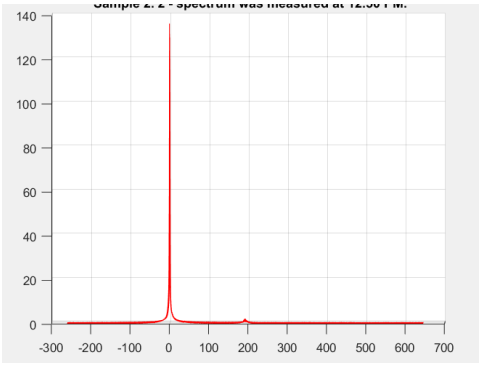

d)

+ γ -CD

Figure A-3: The ^{129}Xe host molecule is 1-ethyl-3-[12-(3-ethylimidazol-3-ium-1-yl)dodecyl]imidazol-1-ium tethered through γ-CD. a) Z-spectrum involving 16 x 30 3-lobe sinc pulse with a 140° flip angle. b) Z-spectrum involving a 1 500 ms sine pulse with a 1530° flip angle. c) 1D spectrum that shows 0 ppm and 196 ppm as the ^{129}Xe gas phase and dissolved phase peaks, respectively. d) Structure of 1-ethyl-3-[12-(3-ethylimidazol-3-ium-1-yl)dodecyl]imidazol-1-ium.. The sample of ^{129}Xe host molecule was dissolved in 4 mL of deionized water.

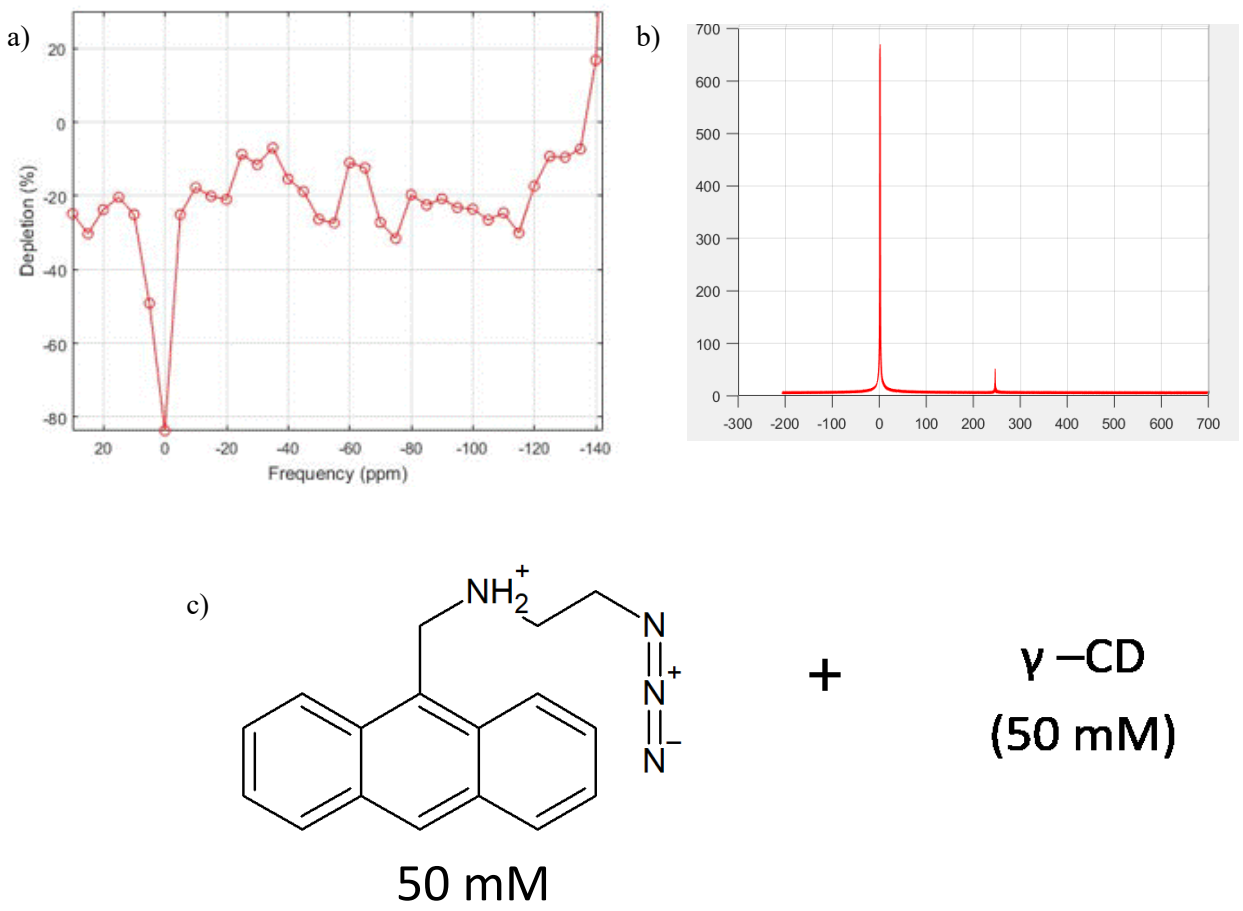

Figure A-4: The ^{129}Xe host molecule is an anthracene-based compound tethered through γ-CD. a) Z-spectrum involving a one 500 sine pulse with a 140° flip angle. b) 1D spectrum showing 0 ppm and 250 ppm as the ^{129}Xe gas-phase and dissolved-phase peaks, respectively. c) Structure of anthracene-based compound for z-spectra of figure A-4. Sample of this ^{129}Xe host molecule was dissolved in 4 mL of DMSO.

a)

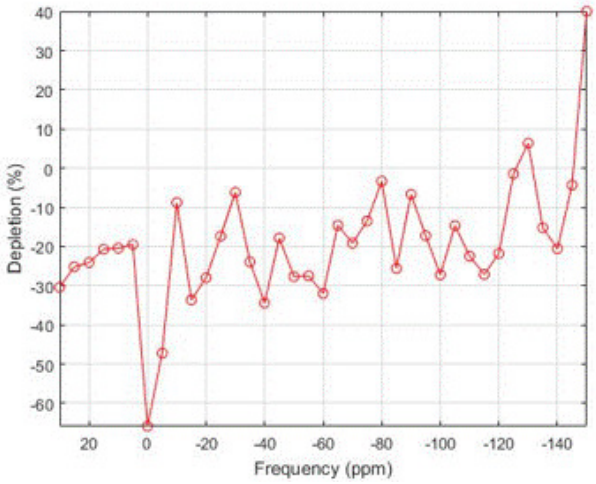

b)

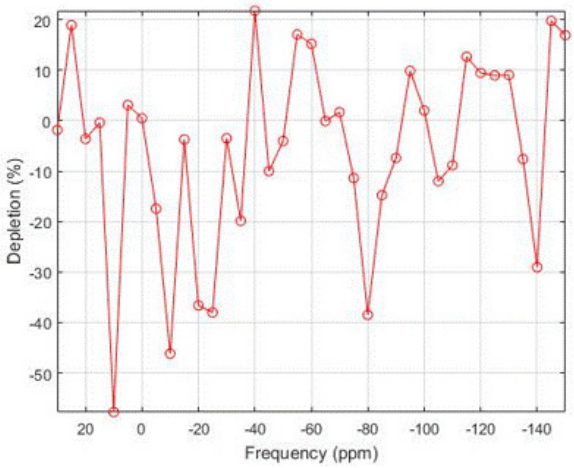

c)

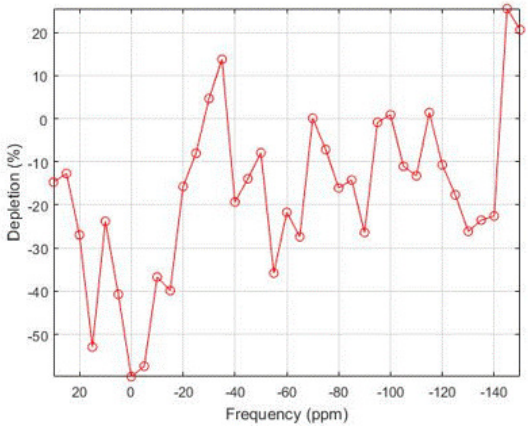

d)

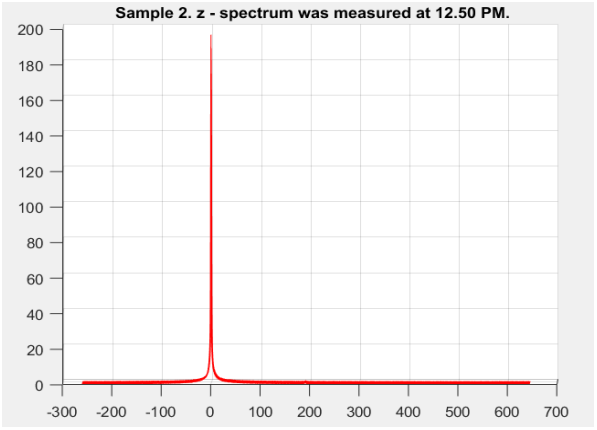

e)

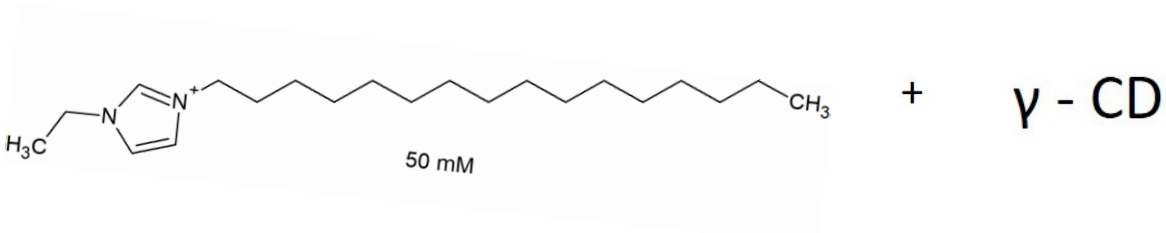

Figure A-5: The ^{129}Xe host molecule consists of 1-ethyl-3-hexadecyl-1H-imidazole-3-ium tethered through γ-CD. a) Z-spectrum involving a one 500 sine pulse with a 140° flip angle. b) Z-spectrum involving 16 x 30 sinusoidal wave pulse with 1530° flip angle. c) Z-spectrum involving a 16 x 30 3-lobe sinc pulse with 1530° flip angle. d) 1D spectrum showing 0 ppm as the ^{129}Xe gas phase peak. e) Structure of 1-ethyl-3-hexadecyl-1H-imidazole-3-ium. Sample of ^{129}Xe host molecule was dissolved in 4 mL of deionized water.

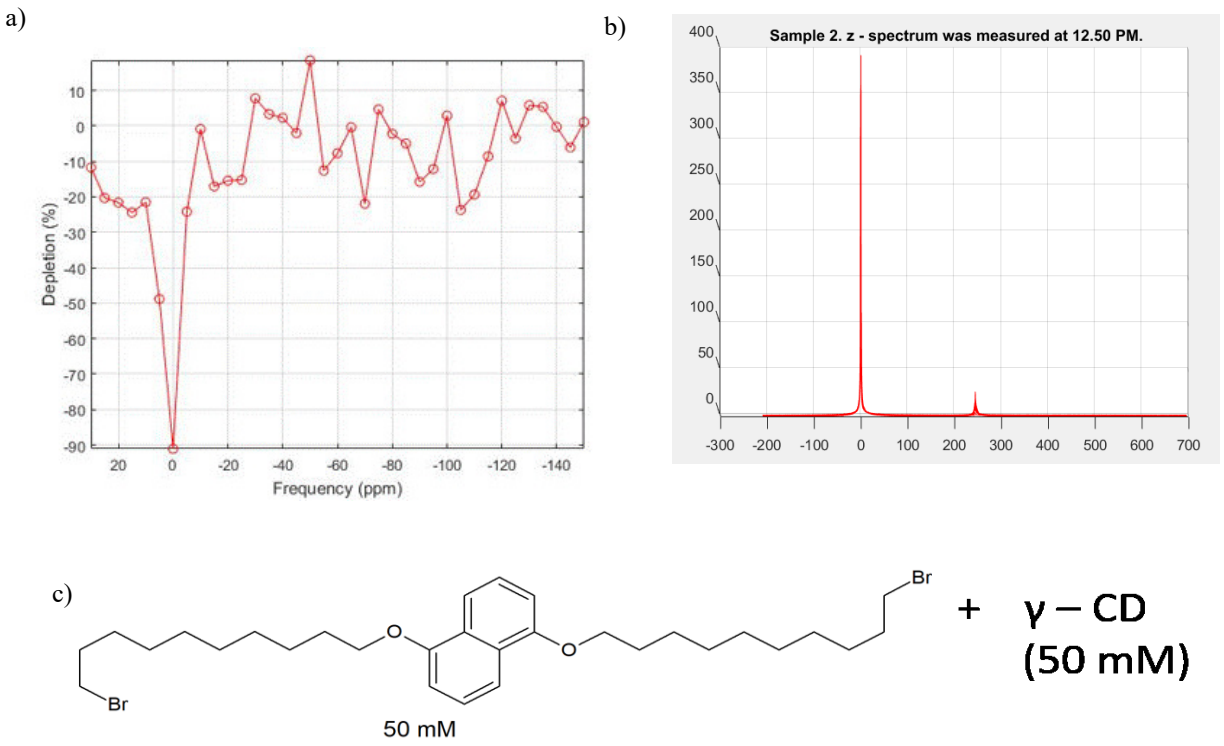

Figure A-6: The ^{129}Xe host molecule is 1,5 -bis(10-bromodedoxy)naphthalene tethered through γ-CD. a) Z-spectrum for 16 x 30 3-lobe sinc pulse with 140° flip angle. b) 1-D spectrum that shows 0 ppm and 250 ppm as the ^{129}Xe gas-phase and dissolved-phase peaks, respectively. c) Structure of 1,5 -bis(10-bromodedoxy)naphthalene for figure A-6 a to b. Sample of ^{129}Xe host molecule was dissolved in 4mL in DMSO.

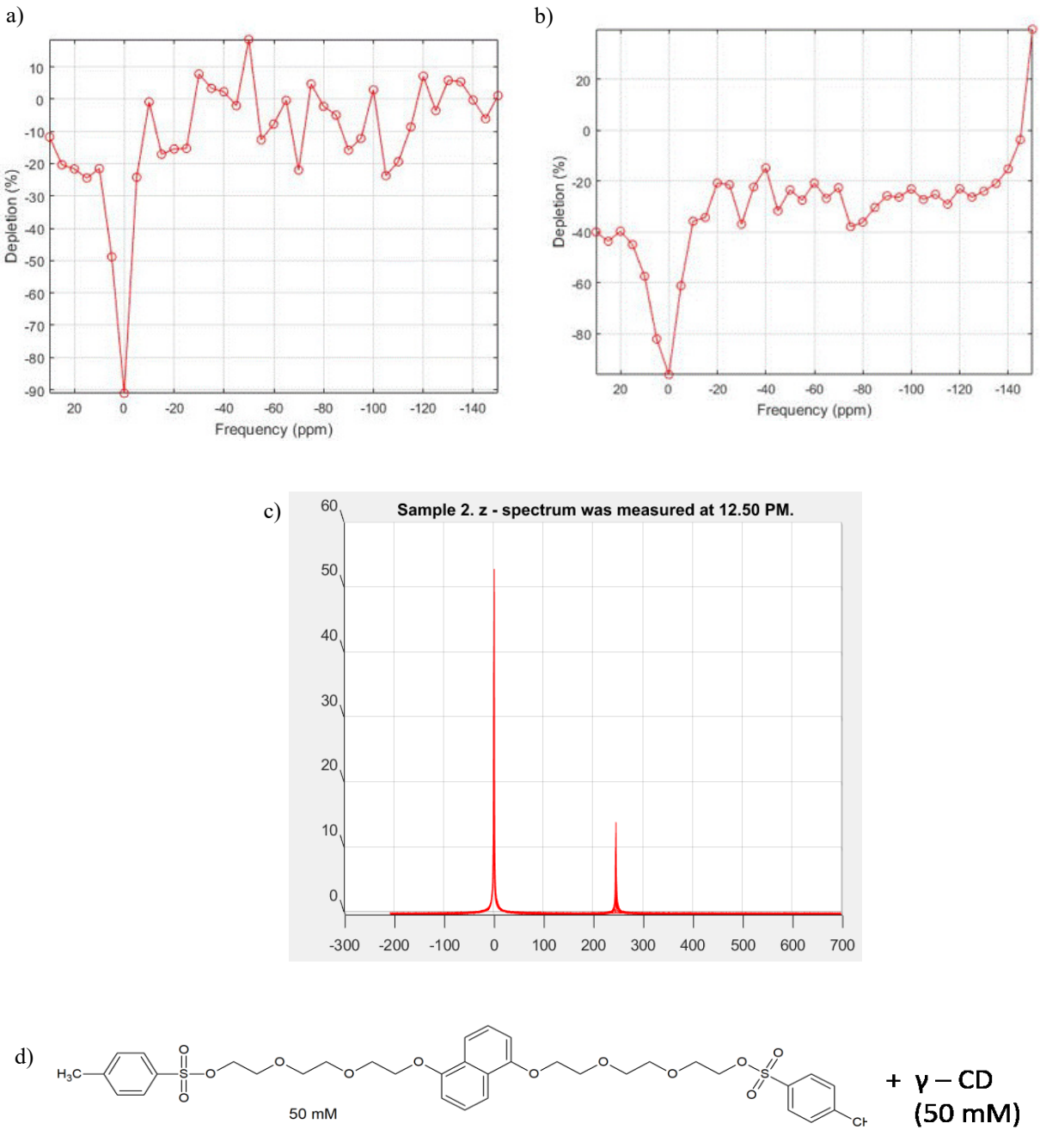

Figure A-7: The ^{129}Xe host molecule consists of 1,5-bis[2-[2-[2-(Tosyloxy)Ethoxy]Ethoxy]Ethoxy]Naphthalene tethered through γ-CD. a) Z-spectrum for 16 x 30 3-lobe sinc pulse with a 140° flip angle. b) Z-spectrum for 16 x 30 sinusoidal wave pulse with 1530° flip angle. c) 1D spectrum that shows 0 ppm and 250 ppm as the ^{129}Xe gas phase and dissolved-phase peaks, respectively. d) Structure of 1,5-bis[2-[2-[2-(tosyloxy)ethoxy]ethoxy]ethoxy]naphthalene. Sample of ^{129}Xe host molecule was dissolved in 4 mL of DMSO.

a)

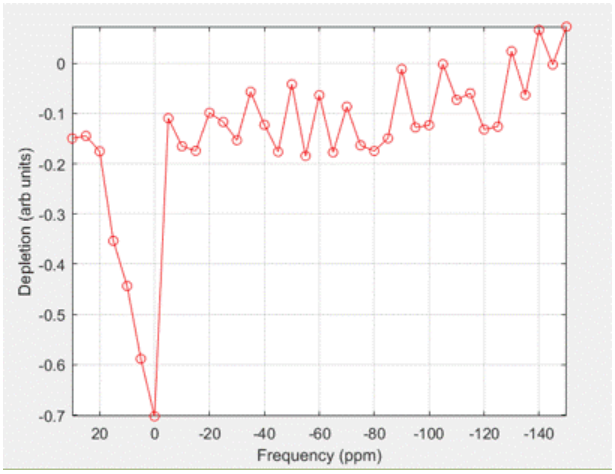

b)

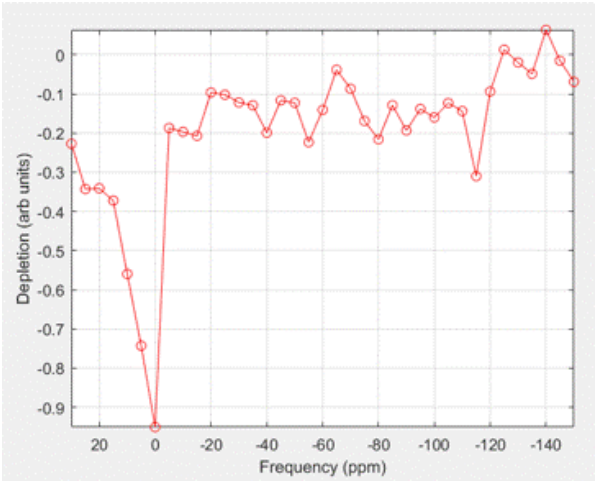

c)

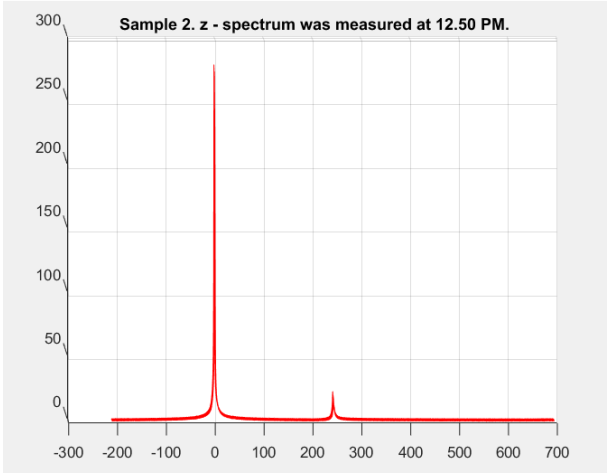

d)

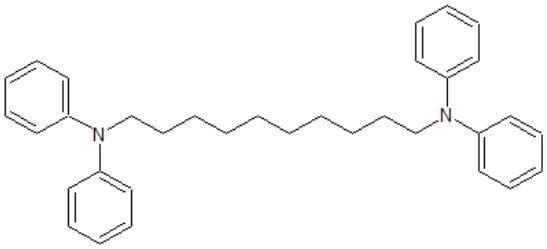

+ γ –CD (50 mM)

Figure A-8: The ^{129}Xe host molecule is N,N,N',N'-tetraphenyldecane-1,10-diamine tethered through γ-CD. a) Z-spectrum for 16 x 303-lobe sinc pulse with a 140° flip angle. b) Z-spectrum involving a 16 x 30 sinusoidal wave pulse with 1530° flip angle. c) 1D spectrum that shows 0 ppm and 250 ppm as the ^{129}Xe gas-phase and dissolved-phase peaks, respectively. d) Structure of N,N,N',N'-tetraphenyldecane-1,10-diamine for z-spectra of figure A-8, which was dissolved in 4 mL of DMSO.

a)

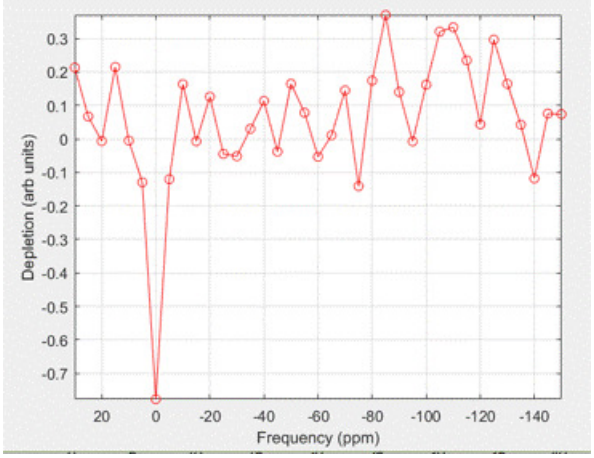

b)

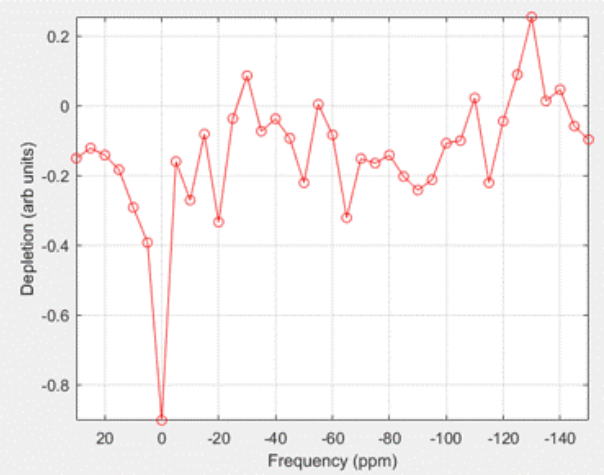

c)

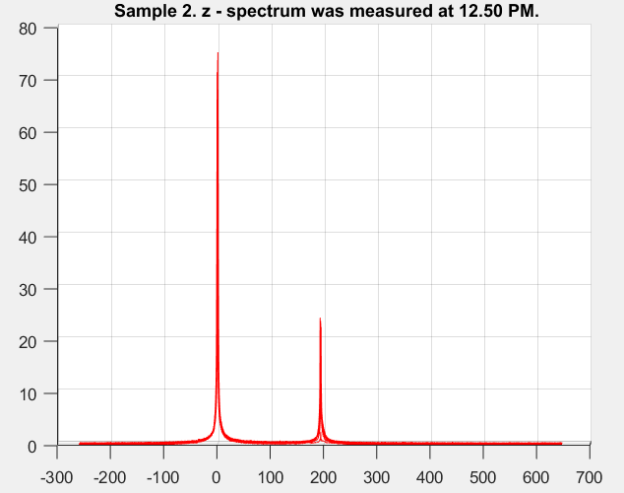

d)

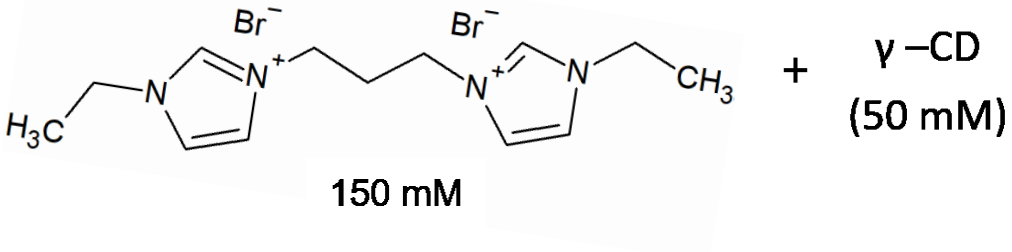

Figure A-9: The ^{129}Xe host molecule is chains of 3,3'-trimethylenebis(1-ethyl-1H-imidazole-3-ium) tethered through γ-CD. a) Z-spectrum for 16 x 30 3-lobe sinc pulse with a 140° flip angle. b) Z-spectrum for 16 x 30 sinusoidal wave pulse with 1530° flip angle. c) 1D spectrum that shows 0 ppm and 196 ppm as the ^{129}Xe gas-phase and dissolved-phase peaks, respectively. d) Structure of 3,3'-trimethylenebis(1-ethyl-1H-imidazole-3-ium). Sample was dissolved in 4 mL of deionized water.

a)

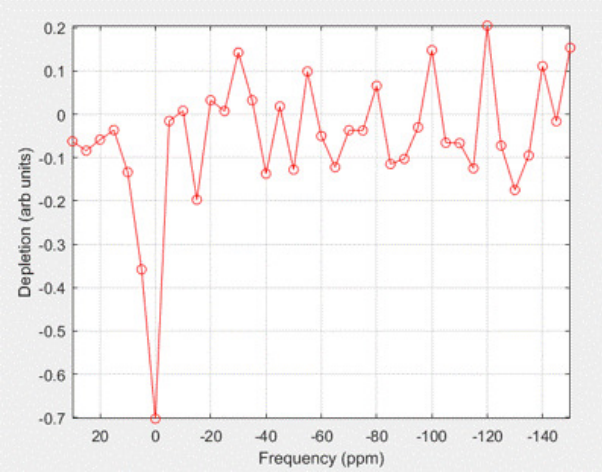

b)

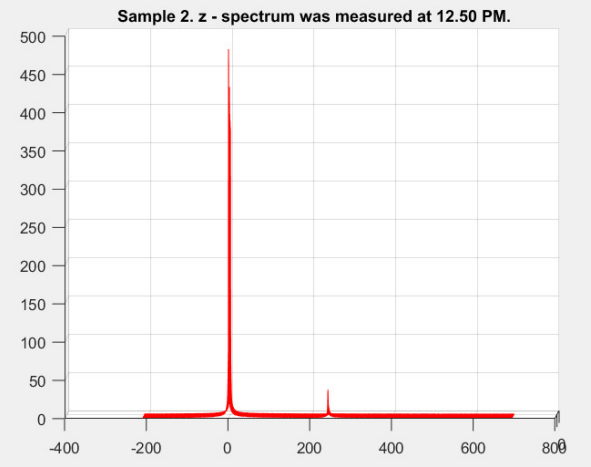

c)

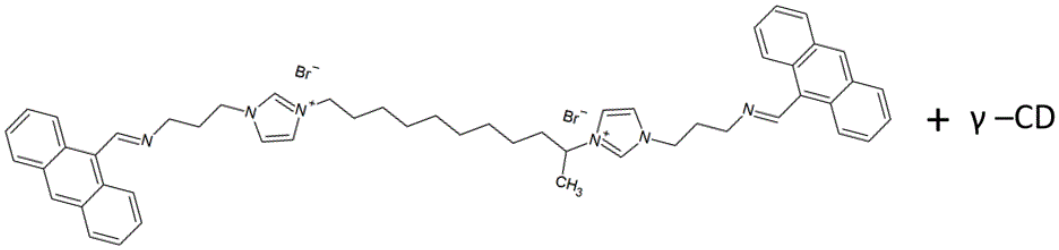

Figure A-10: The ^{129}Xe host molecule is an anthracene-based chain threaded through γ-CD. a) Z-spectrum involving a 16 x 30 3-lobe sinc pulse with 140 ° flip angle. b) 1D spectrum that shows 0 ppm and 196 ppm as the ^{129}Xe gas phase and dissolved-phase peaks, respectively. c) Structure of anthracene-based chain for figure A-10. This sample was made in a one pot reaction and dissolved in 4 mL of DMSO.

a)

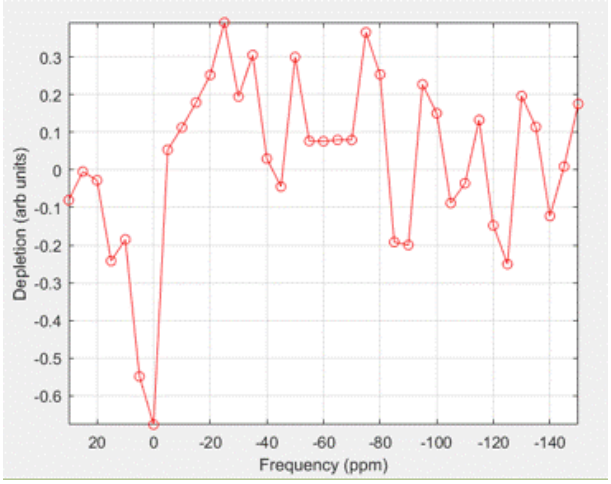

b)

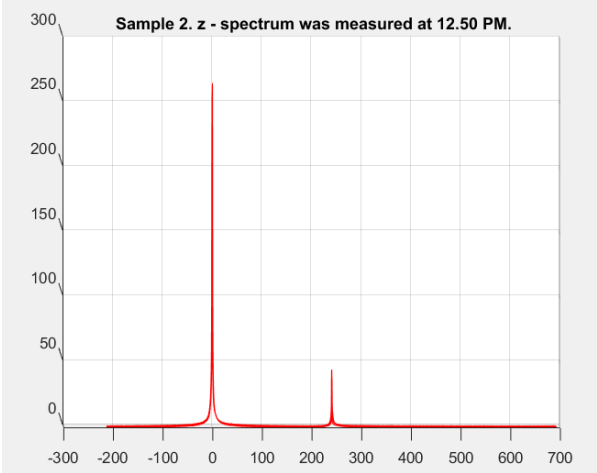

c)

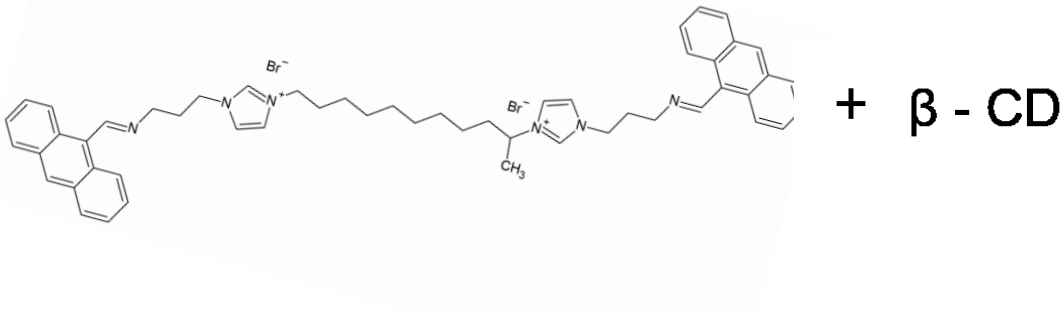

Figure A-11: The ^{129}Xe host molecule is an anthracene-based chain tethered through β-CD. a) Z-spectrum for 16 x 30 sinusoidal wave pulse with 1530 ° flip angle. b) 1D spectrum that shows 0 ppm and 240 ppm as the ^{129}Xe gas phase and dissolved-phase peaks, respectively. c) Structure of anthracene-based chain for figure A-11 a to b; this xenon biosensor was produced via one-pot reaction and dissolved in 4 mL of DMSO.

a)

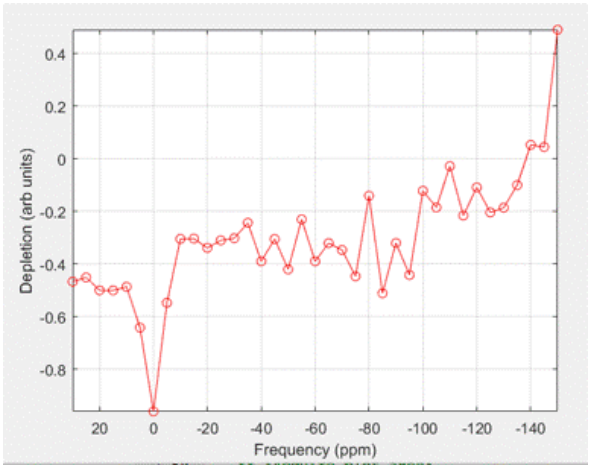

b)

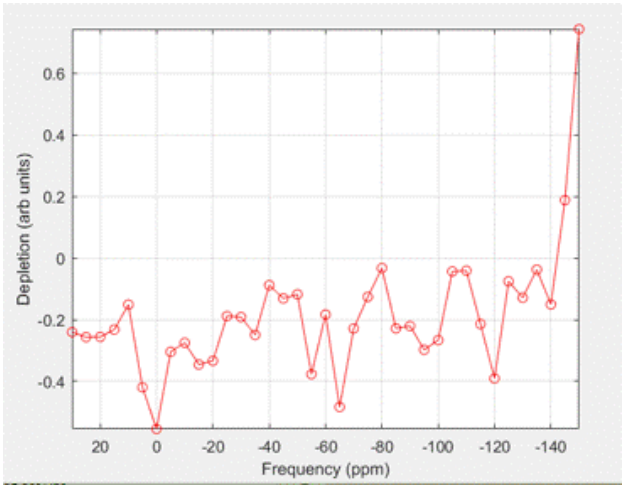

c)

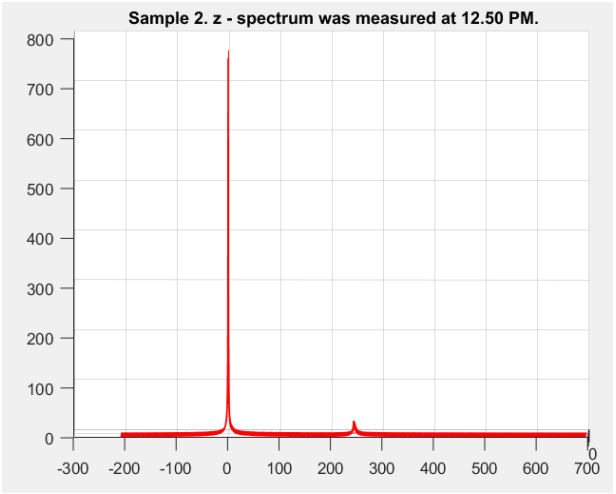

d)

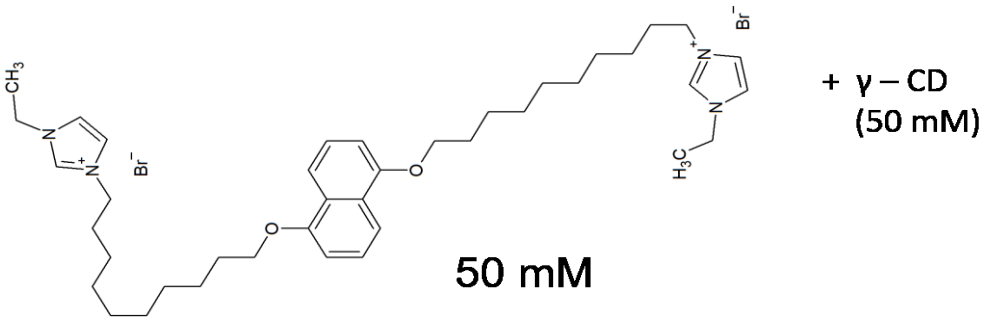

Figure A-12: The ^{129}Xe host molecule is 1-ethyl-3[2-[5-2-(3-ethylimidazol-1-ium-1-yl)decoxy]naphthalen-1-yl[oxydec]imidazole-3-ium tethered through γ-CD. a) Z-spectrum for 16 x 30 sinusoidal wave pulse with 1530 ° flip angle. b) Z-spectrum involving one 500 sine pulse with 140° flip angle. c) 1D spectrum that shows 0 ppm and 250 ppm as the ^{129}Xe gas phase and dissolved-phase peaks, respectively. d) Structure of 1-ethyl-3[2-[5-2-(3-ethylimidazol-1-ium-1-yl)decoxy]naphthalen-1-yl[oxydec]imidazole-3-ium for figure A-12.

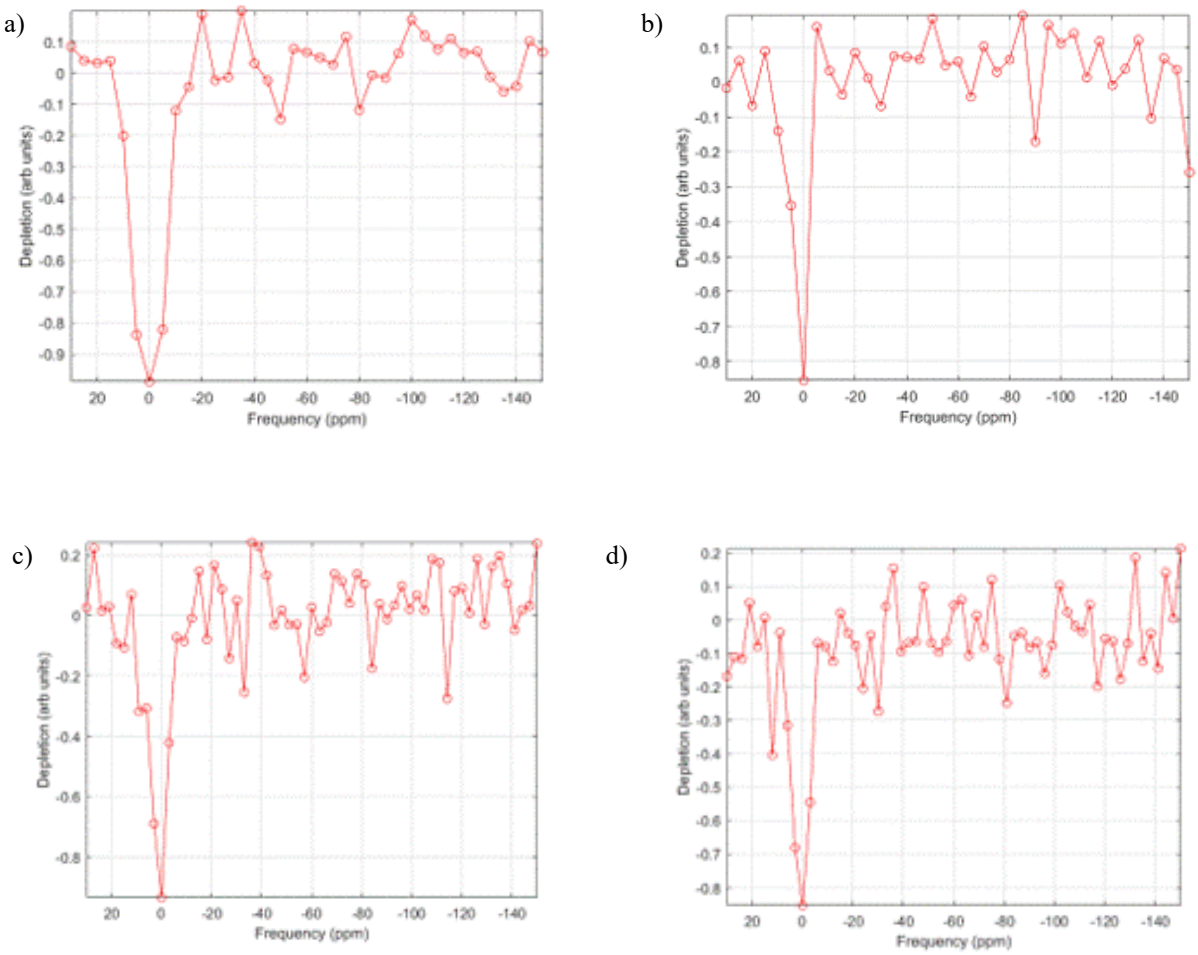

Figure A-13: The ^{129}Xe host molecule is γ-CD with a bar before $NaBH_4$. a) Z-spectrum for 96 x 20 3-lobe sinc pulse with a 180° flip angle. b) Z-spectrum involving a 16 x 30 3-lobe sinc pulse with 180 ° flip angle. c) Z-spectrum involving a 16 x 30 sinusoidal wave pulse with 1530° flip angle. d) Z-spectrum for 16 x 40 continuous sine pulse with 1800° flip angle.

a)

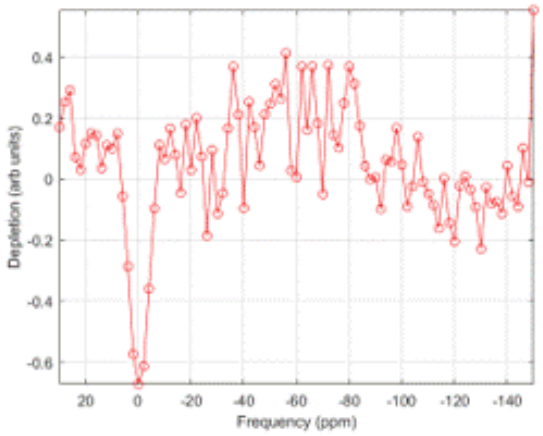

b)

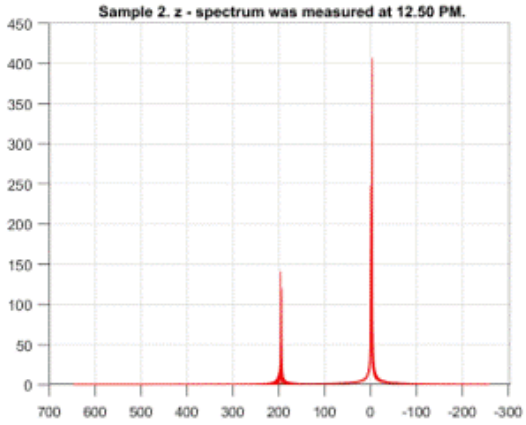

c)

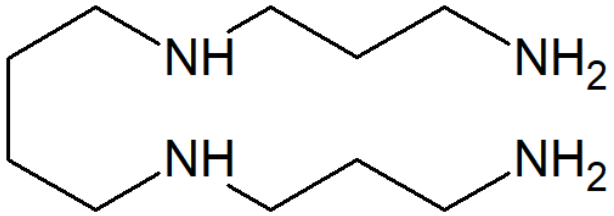

Figure A-14: The ^{129}Xe host molecule consisted of γ-CD threaded with spermine. a) Z-spectrum for 16 x 30 sinusoidal wave pulse with 1530 ° flip angle with TR = 5s. b) 1-D spectrum with dissolved-phase and gas-phase ^{129}Xe peaks at 200 ppm and 0 ppm, respectively. c) Structure of spermine, which was threaded through γ-CD.

a)

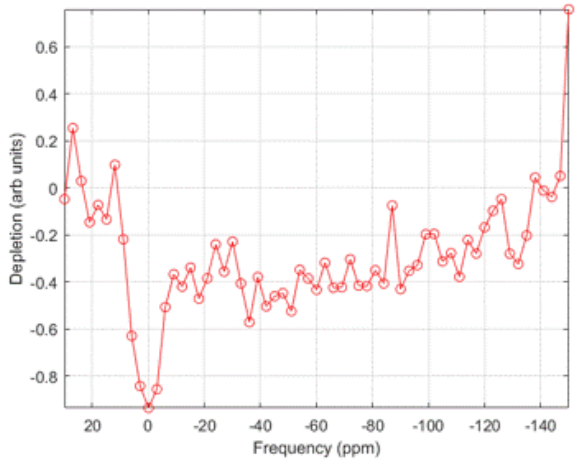

b)

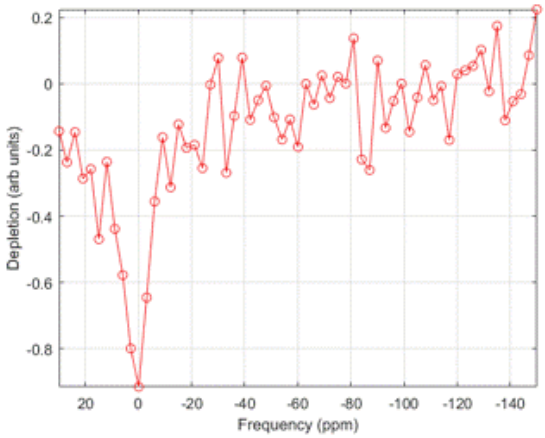

c)

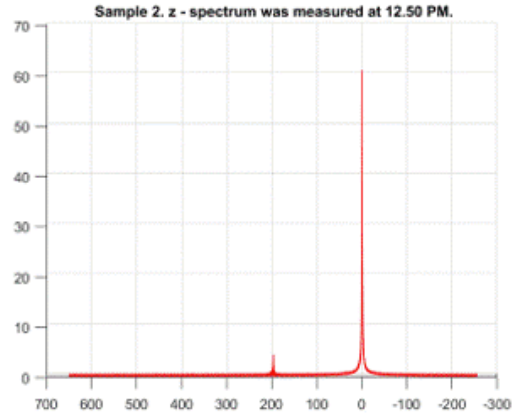

d)

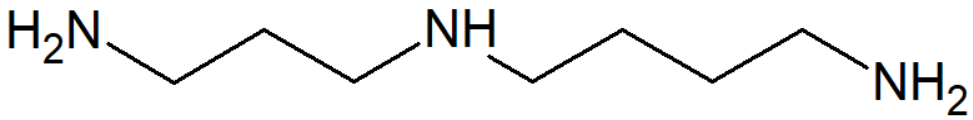

Figure A-15: The ^{129}Xe host molecule consisted of spermidine threaded through γ-CD. a) Z-spectrum for 16 x 30 3-lobe sinc pulse with a 330° flip angle and TR = 6s. b) Z-spectrum for 16 x 30 sinusoidal wave pulse with 1530° flip angle with TR = 4 s. c) 1D spectrum with gas-phase and dissolved-phase ^{129}Xe peaks at 0 ppm and 200 ppm, respectively. e) Structure of spermidine.

a)

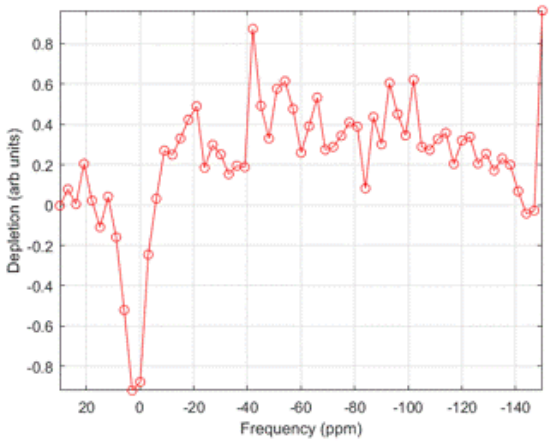

b)

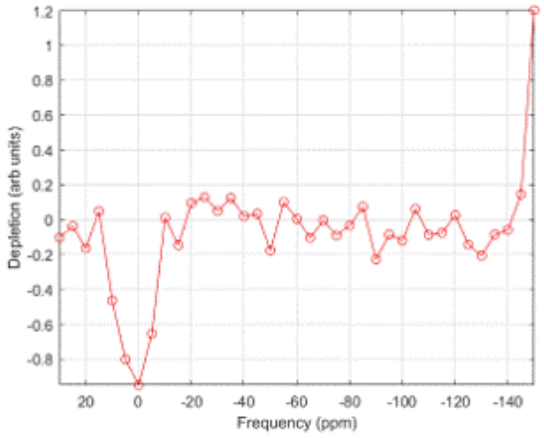

c)

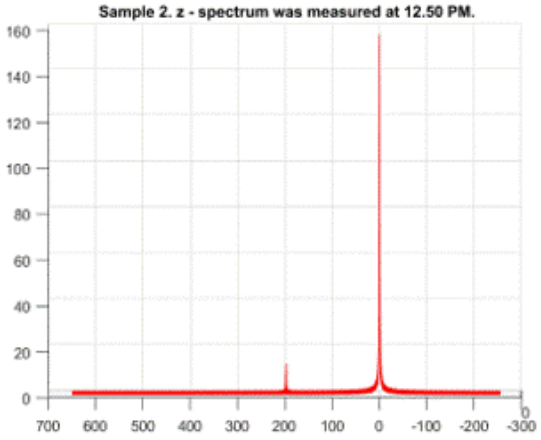

d)

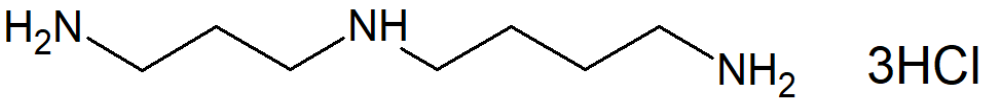

Figure A-16: The ^{129}Xe host molecule is spermidine trihydro chloride tethered through γ-CD. a) Z-spectrum for 16 x 30 sinusoidal wave pulse with 1530 ° flip angle with TR = 4s. b) Z-spectrum for 96 x 20 3-lobe sinc pulse with 180° flip angle and TR = 6s. c) 1D spectrum with gas-phase and dissolved-phase ^{129}Xe peaks at 0 ppm and 200 ppm, respectively. d) Structure of spermidine trichloride. This sample was used for figure A-16.

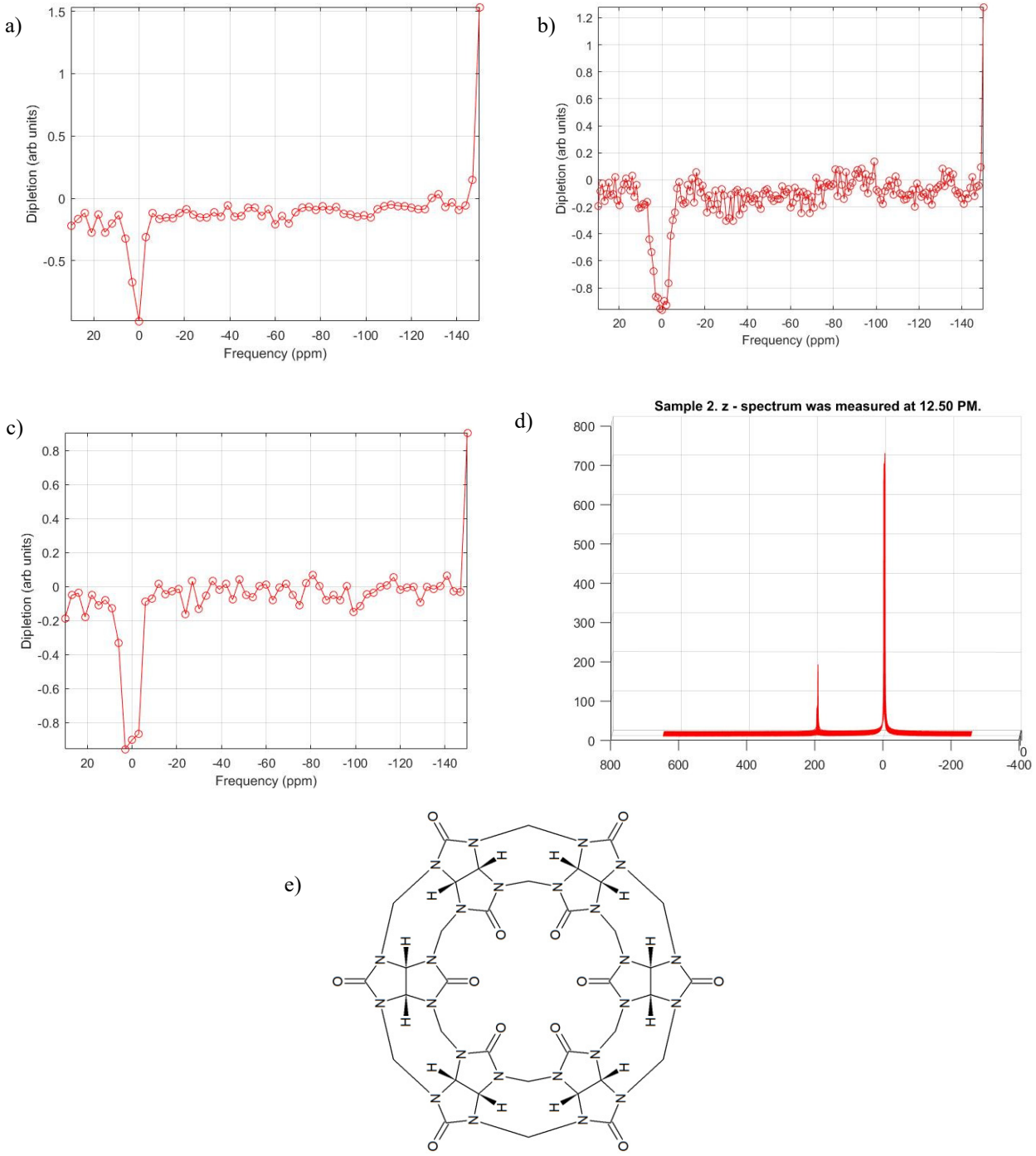

Figure A-17: The ^{129}Xe host molecule was CB[6] with 5-C alkane chain tethered through it. a) Z-spectrum for 16 x 30 3-lobe sinc pulse with a 180° flip angle and TR = 5 s. b) Z-spectrum for 16 x 30 sinusoidal wave pulse with 1530° flip angle with TR = 4 s. c) Z-spectrum for 16 x 30 3-lobe sinc pulse with 330° flip angle and TR = 6 s. d) 1D spectrum with gas-phase and dissolved-phase ^{129}Xe peaks at 0 ppm and 196 ppm, respectively. e) Structure of CB[6].

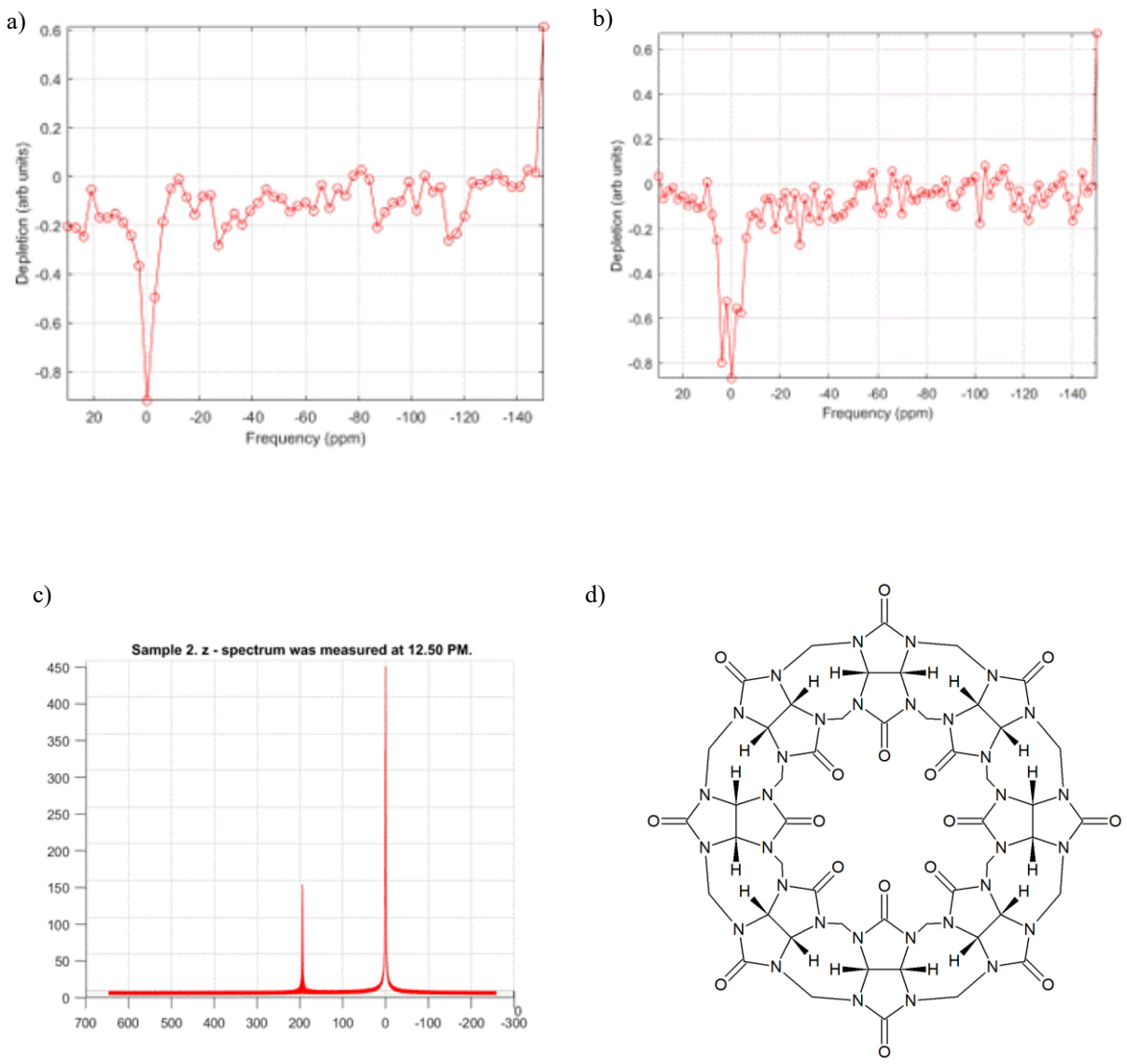

Figure A-18: The ^{129}Xe host molecule was 5-C alkane chain tethered through CB[8]. a) Z-spectrum for 16 x 30 3-lobe sinc pulse with a 140° flip angle and TR = 7 s. b) Z-spectrum for 16 x 30 sinusoidal wave pulse with 1530° flip angle with TR = 6s. c) 1D spectrum with gas-phase and dissolved-phase ^{129}Xe peaks at 0 ppm and 198 ppm, respectively. d) Structure of CB[8], where 5-C alkane chain was threaded through this molecule.

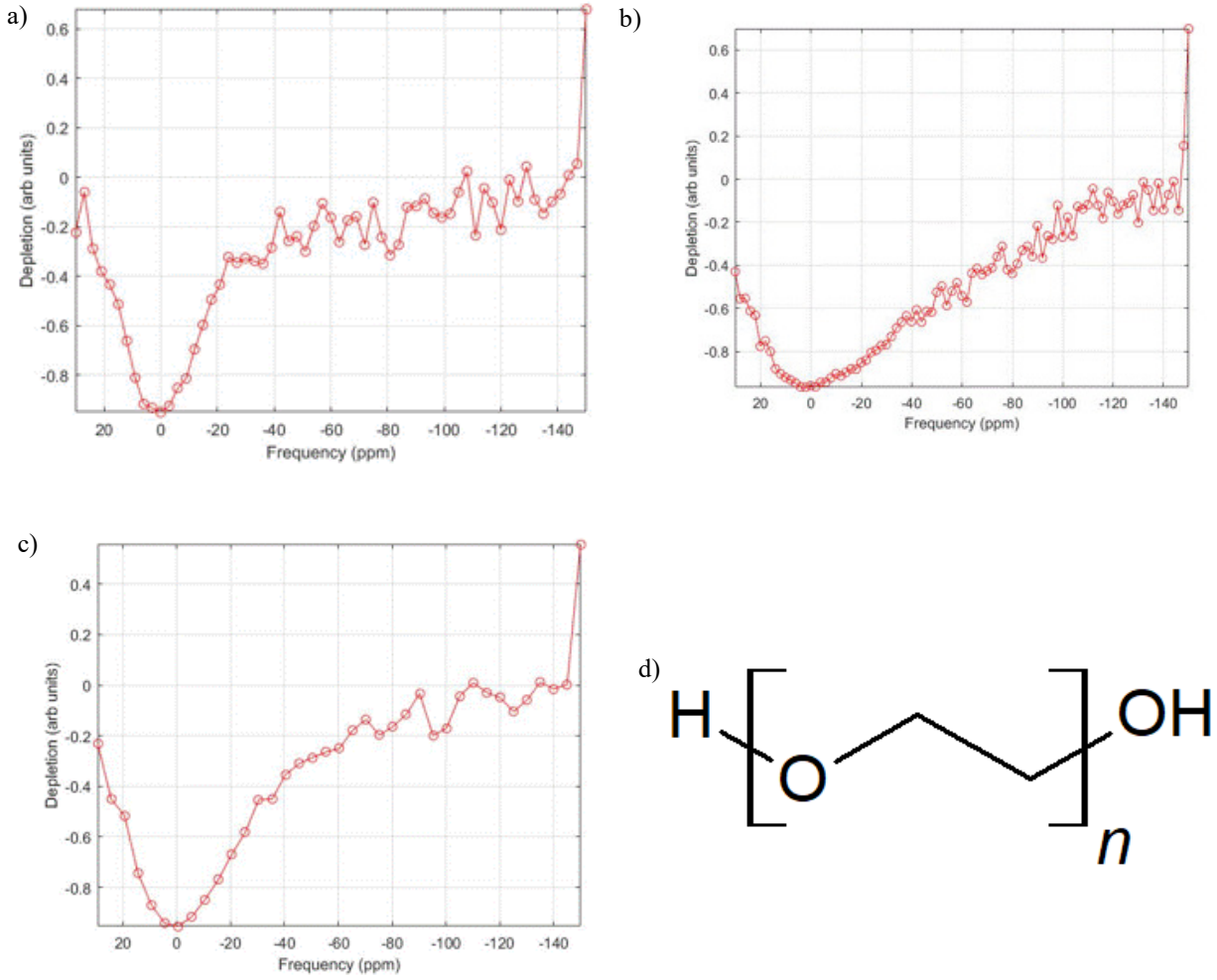

Figure A-19: The ^{129}Xe host molecule was PEG-600 tethered through γ-CD. a) Z-spectrum for 16 x 30 3-lobe sinc pulse with a 330° flip angle and TR = 6s. b) Z-spectrum for 16 x 30 sinusoidal wave pulse with 1530° flip angle with TR = 6s. c) Z-spectrum for 96 x 20 3-lobe sinc pulse with 180° flip angle and TR = 6s. d) Structural unit for PEG-600 molecule, where n = 600.

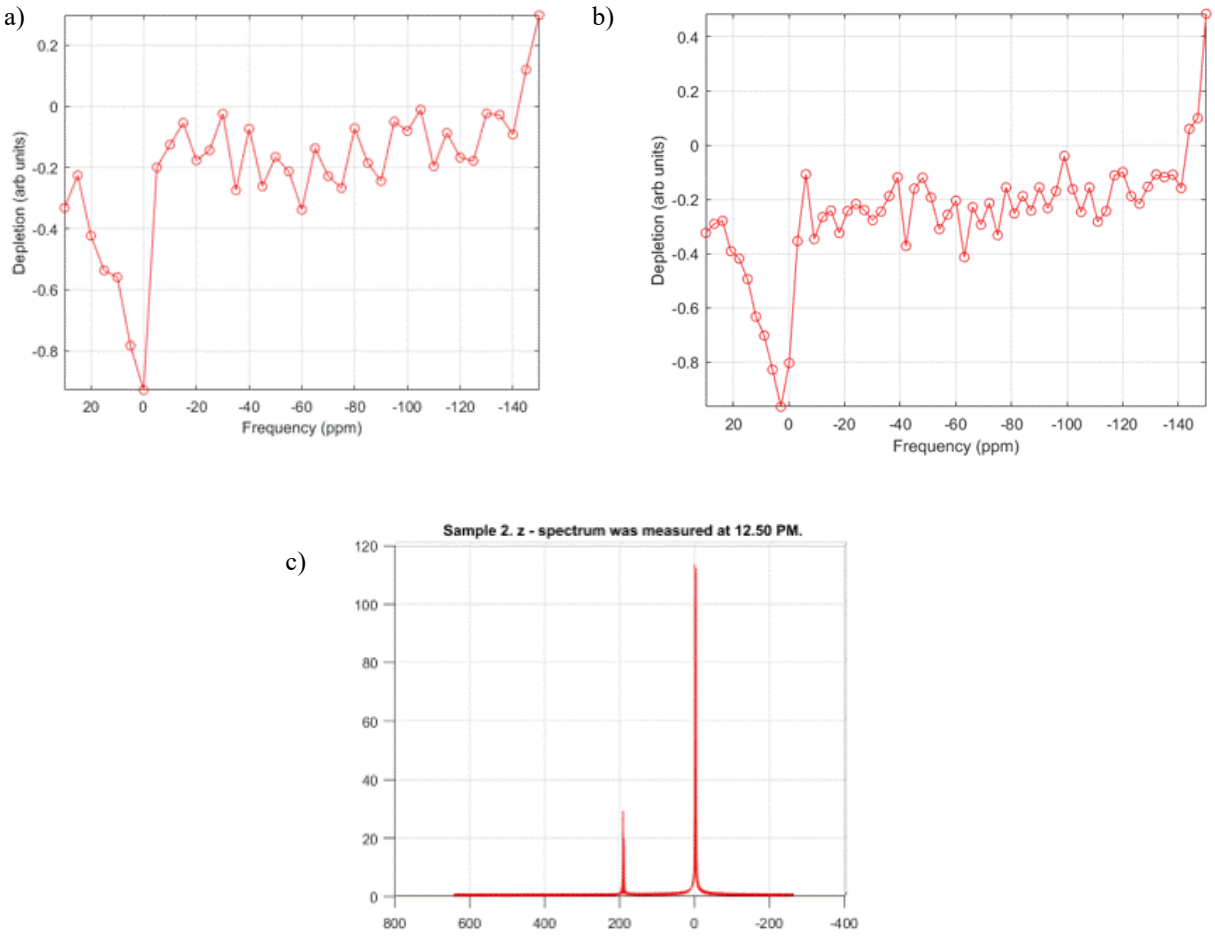

Figure A-20: The ^{129}Xe host molecule consisted of γ-CD tethered through 10-C alkane chain. a) Z-spectrum for 96 x 20 3-lobe sinc pulse with 180° flip angle and TR = 6 s. b) Z-spectrum for 16 x 20 3-lobe sine pulse with 330° flip angle and TR = 6 s. c) 1D spectrum with gas-phase and dissolved-phase ^{129}Xe peaks at 0 ppm and 200 ppm, respectively.

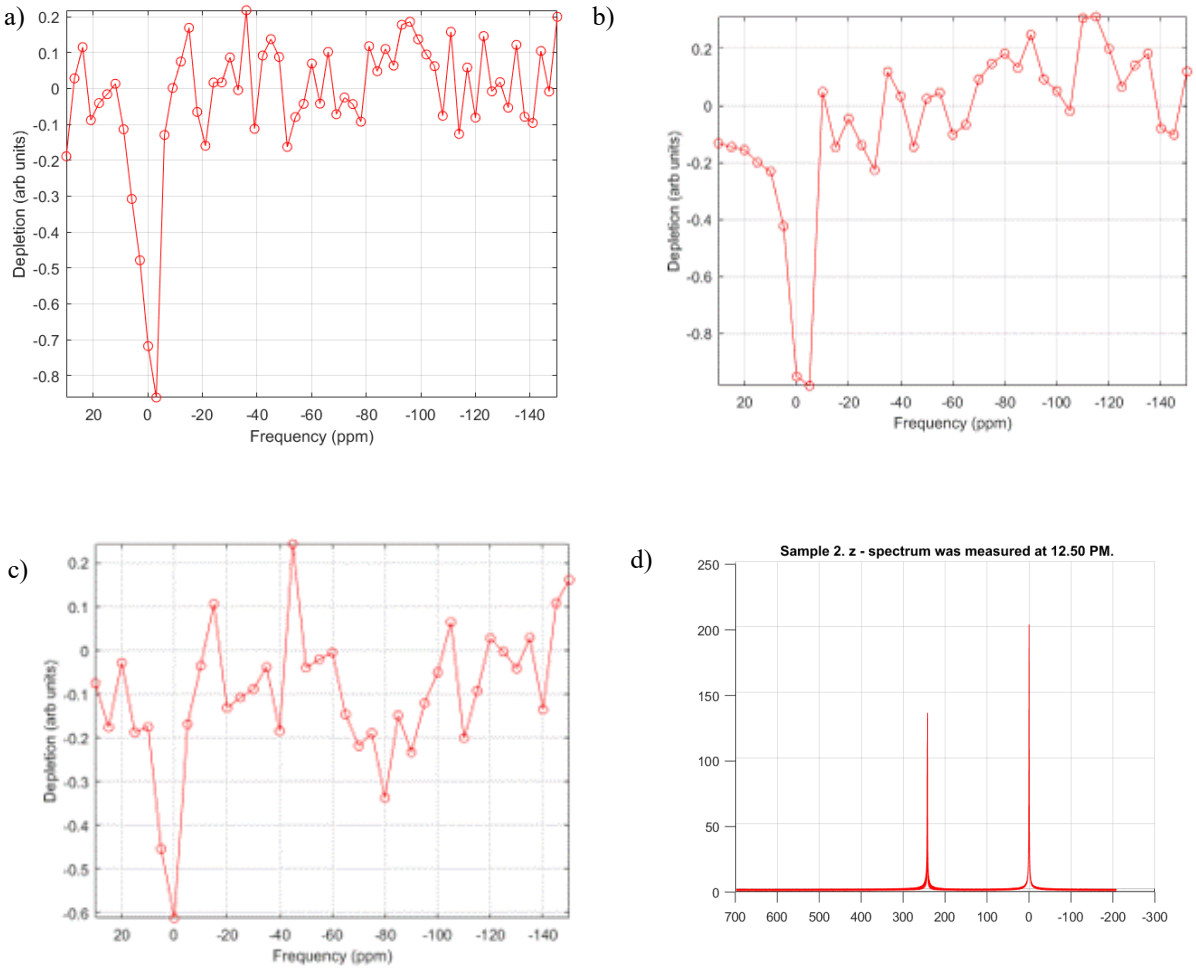

Figure A-21: The ^{129}Xe host molecule was γ-CD with bar after $NaBH_4$. a) Z-spectrum for 16 x 30 3-lobe sinc pulse with 330° flip angle and TR = 4 s. b) Z-spectrum for 96 x 20 3-lobe sine pulse with 180° flip angle and TR = 6 s. c) Z-spectrum for 16 x 30 sinusoidal wave pulse with 1530° flip angle and TR = 4 s. d) 1D spectrum with gas-phase and dissolved-phase ^{129}Xe peaks at 0 ppm and 250 ppm, respectively.

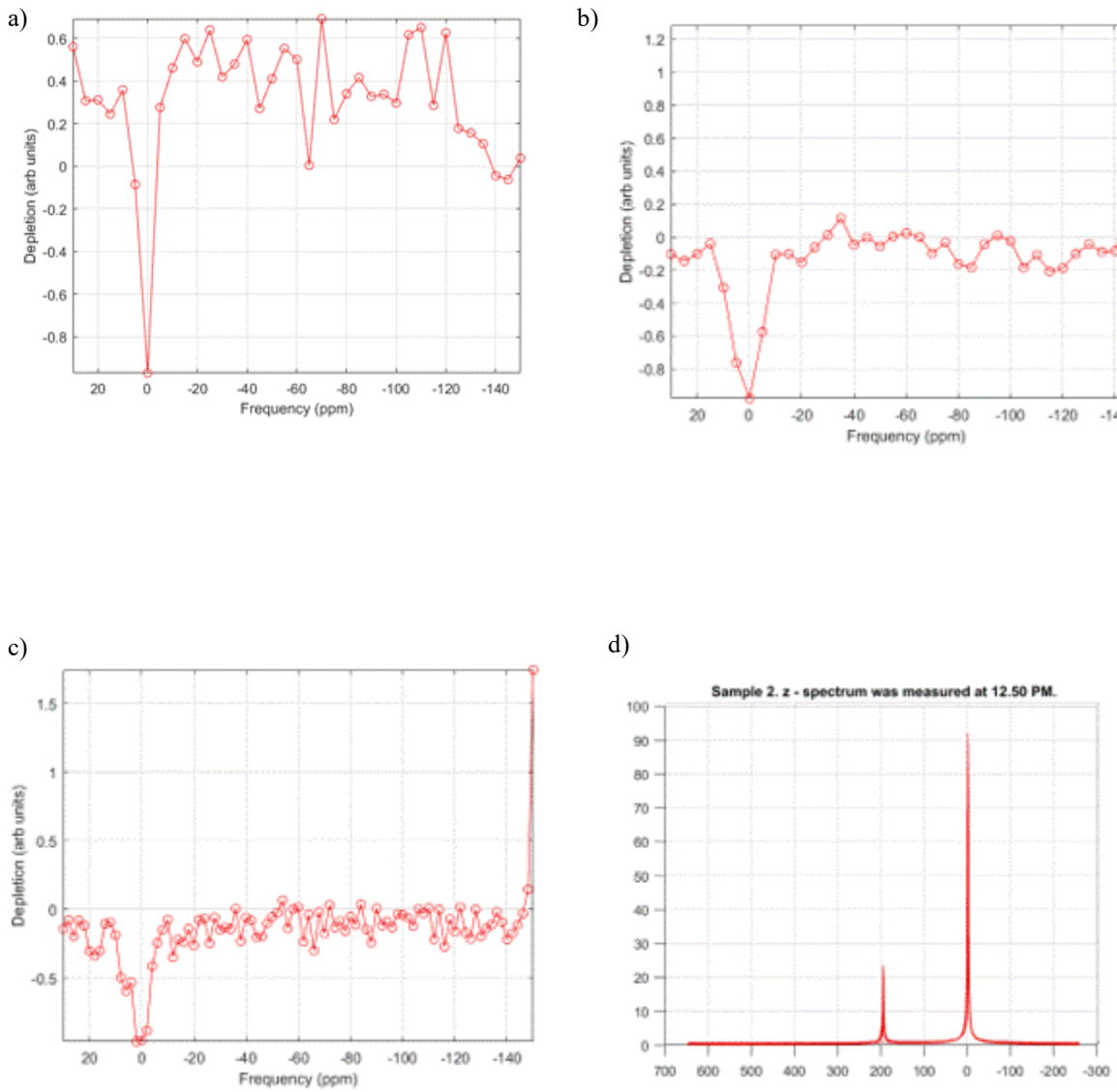

Figure A-22: The ^{129}Xe host molecule was γ-CD tethered through 8-C alkane chain. a) Z-spectrum for 16 x 30 3-lobe sinc pulse with a 140° flip angle and TR = 4s. b) Z-spectrum for 96 x 20 3-lobe sinc pulse with 180° flip angle and TR = 6.5 s. c) Z-spectrum for 16 x 30 sinusoidal wave pulse with 1530° flip angle and TR = 5.5 s. d) 1D spectrum with gas-phase and dissolved-phase ^{129}Xe peaks at 0 ppm and 198 ppm, respectively.

Appendix B: Additional Off-Resonance Images, On-Resonance Images, and Saturation Maps pertaining to the HyperCEST Effect in the Lungs of Sprague-Dawley Rats.

This appendix contains additional off-resonance images, on-resonance images, and saturation maps, which were omitted from chapter 4 to enhance flow of this thesis. Some saturation maps show positive signal depletion in the lungs, such as figures B-3, B-4, B-6, B-7, B-40, and B-41. Other saturation maps show negative signal depletion in the lungs, as shown in the following figures: B-1, B-2, B-5, B-8, B-9, B-15, B-18, B-19, B-21, B-22, B-36, B-38, B-39, and B-42. The rest of the figures show both positive and negative signal depletion in the lungs.

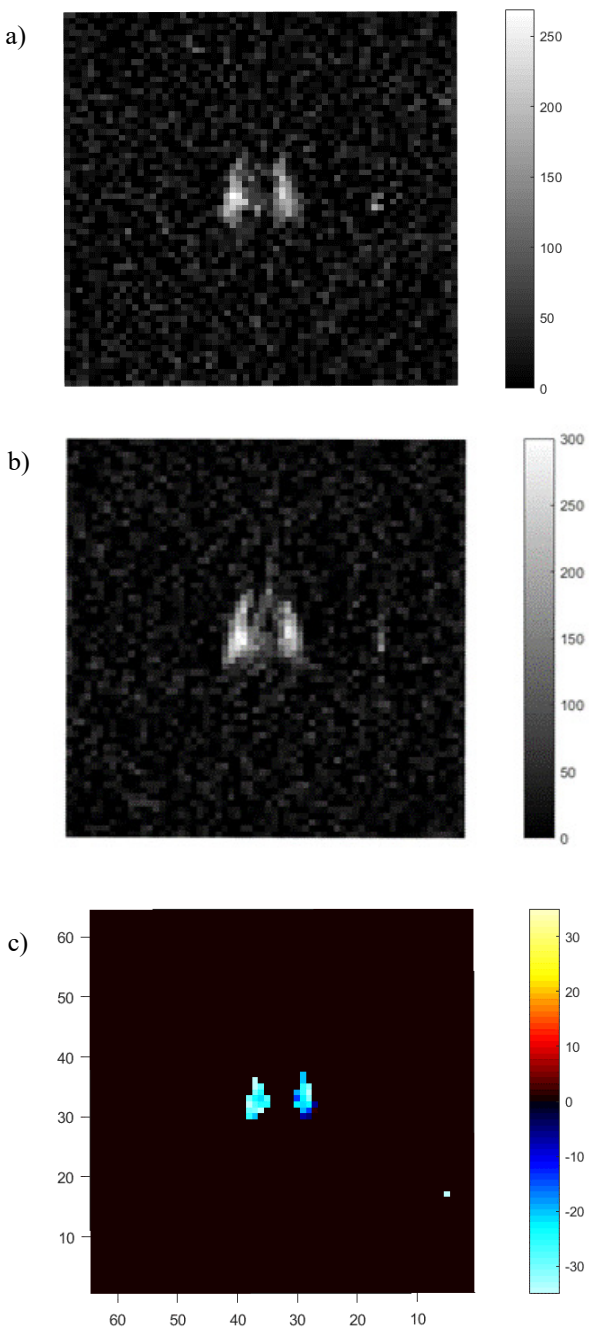

Figure B-1: a) Off-resonance image with SNR = 9; b) On-resonance image with SNR = 11. Both a) and b) were generated using the following parameters: a 16 x 30 3-lobe sinc pulse, TR = 5s, flip angle = 15°, and pulse angle = 140°. c) Saturation map of a) and b).

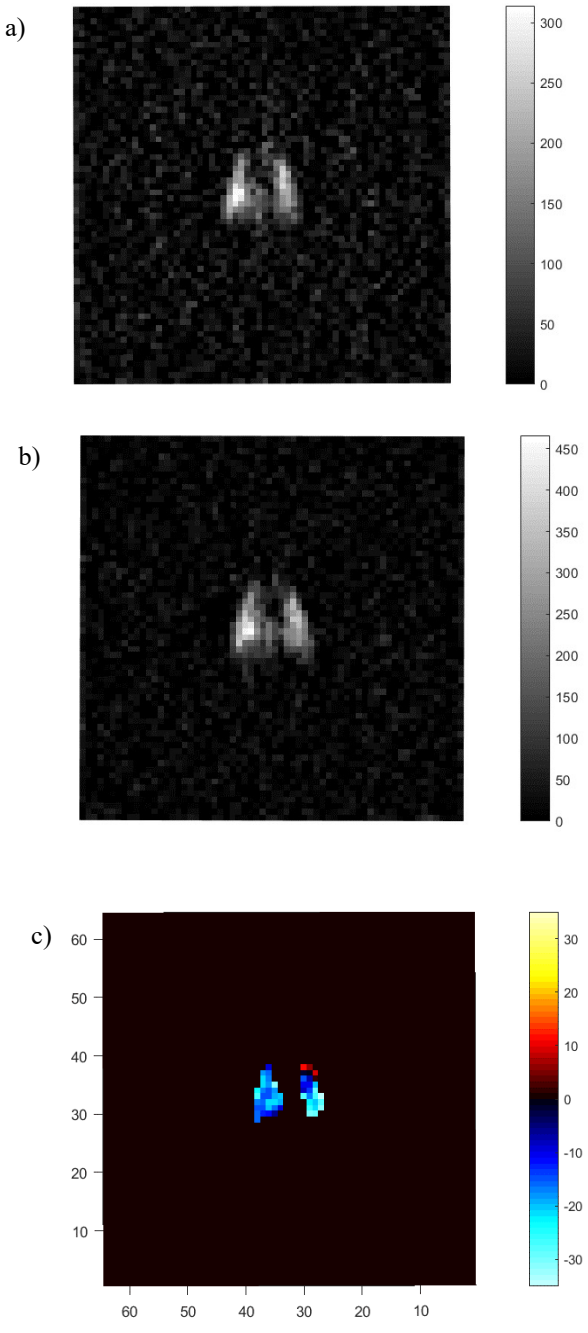

Figure B-2: a) Off-resonance image with SNR = 10; b) On-resonance image with SNR = 23. Both a) and b) were produced using a 16 x 30 3-lobe sinc pulse, TR = 5s, flip angle = 15°, and pulse angle = 140°. c) Saturation map of figure B-2 a) and b).

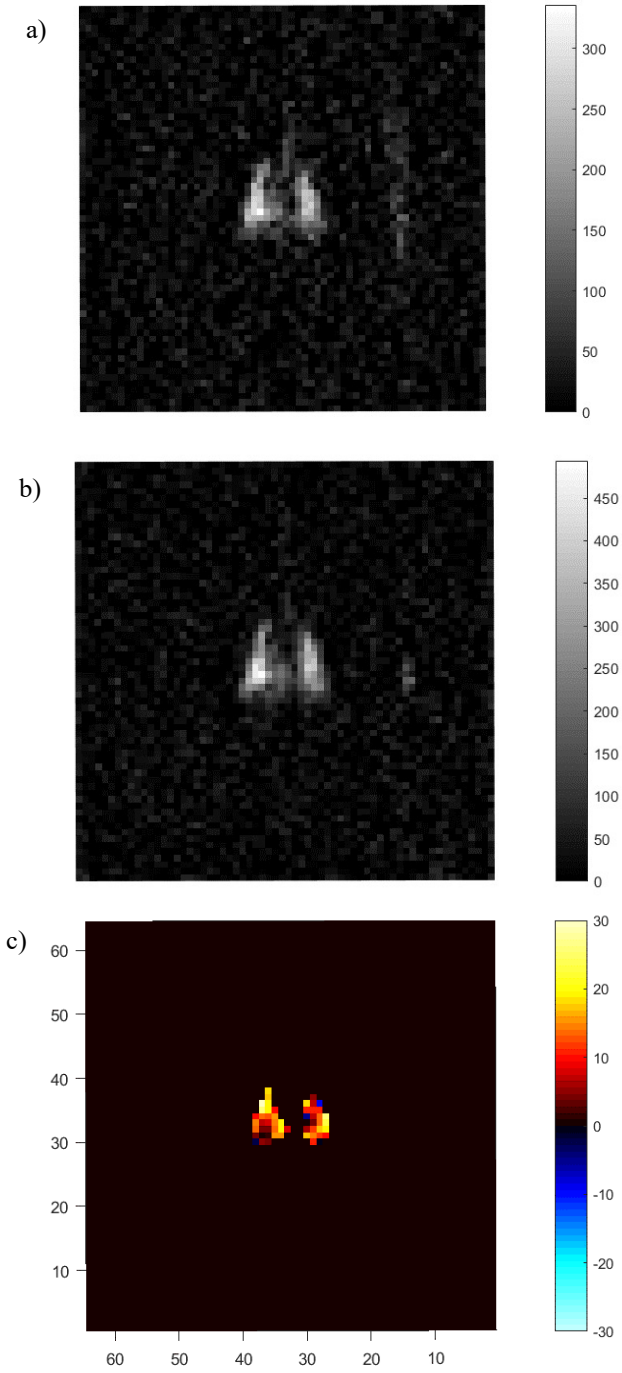

Figure B-3: a) Off-resonance image with SNR = 13; b) On-resonance image with SNR = 12; both a) and b) were produced using a 16 x 30 3-lobe sinc pulse, TR = 5s, flip angle = 15°, and pulse angle = 140°. c) Saturation map of figure B-3 a) and b).

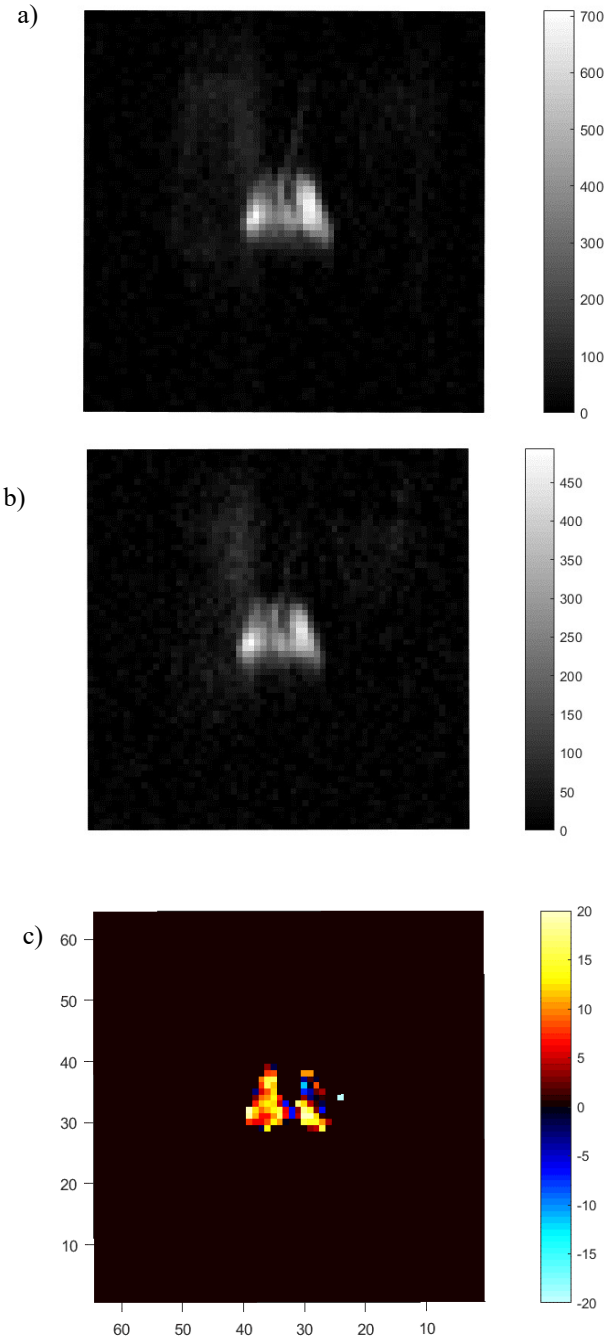

Figure B-4: a) Off-resonance image with SNR = 13; b) On-resonance image with SNR = 12. Both a) and b) were produced using a 16 x 30 3-lobe sinc pulse, TR = 5s, flip angle = 15°, and pulse angle = 140°. c) Saturation map of figure B-4 a) and b).

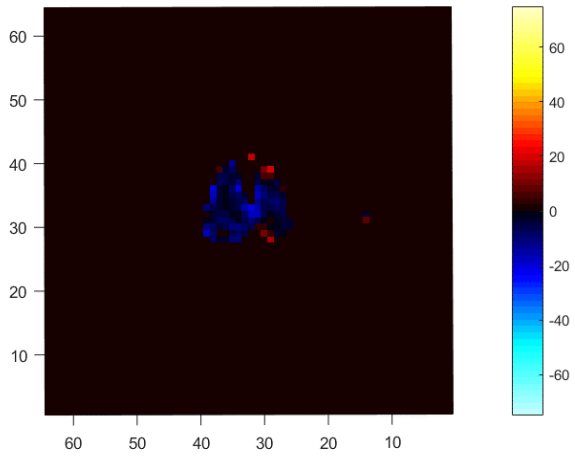

Figures B-5: Saturation amp with four off-resonance (panel a of figures B-1 to B-4) and four on-resonance images (panel b of figures B-1 to B-4).

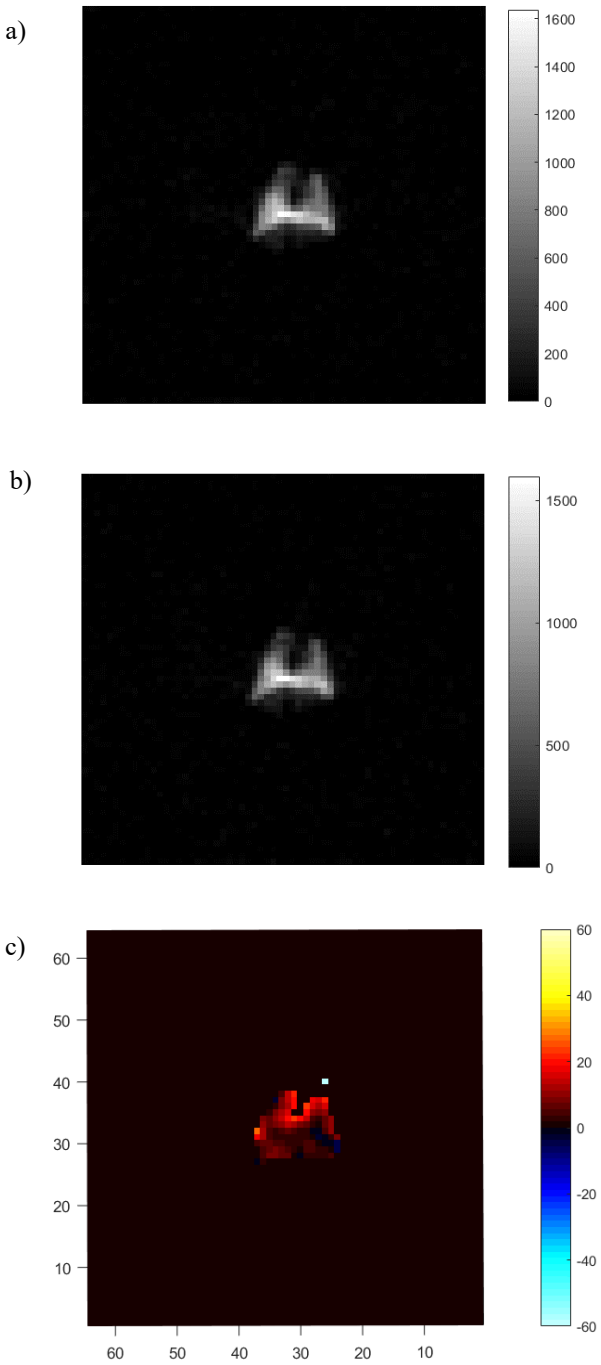

Figure B-6: a) Off-resonance image with SNR = 45.05; b) On-resonance image with SNR = 41.00. Both a) and b) were produced using a 16 x 30 3-lobe sinc pulse, TR = 5s, flip angle = 15°, and pulse angle =140°. Signal percent depletion is 9.0 %. c) Saturation map of figure B-6 a) and b).

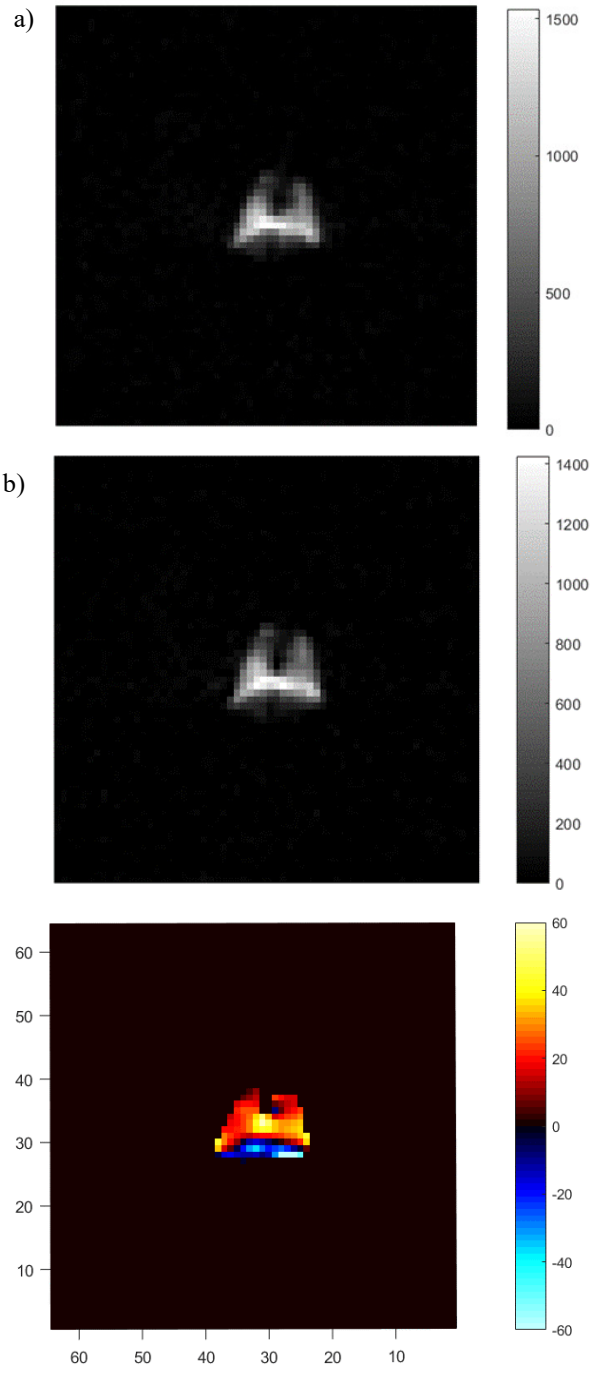

Figure B-7: a) Off-resonance image with SNR = 52.50; b) On-resonance image with SNR = 51.87. Both a) and b) were produced using a 16 x 30 3-lobe sinc pulse, TR = 5s, flip angle = 15°, and pulse angle =140°. Signal percent depletion is 1.20%. c) Saturation map of figure B-7 a) and b).

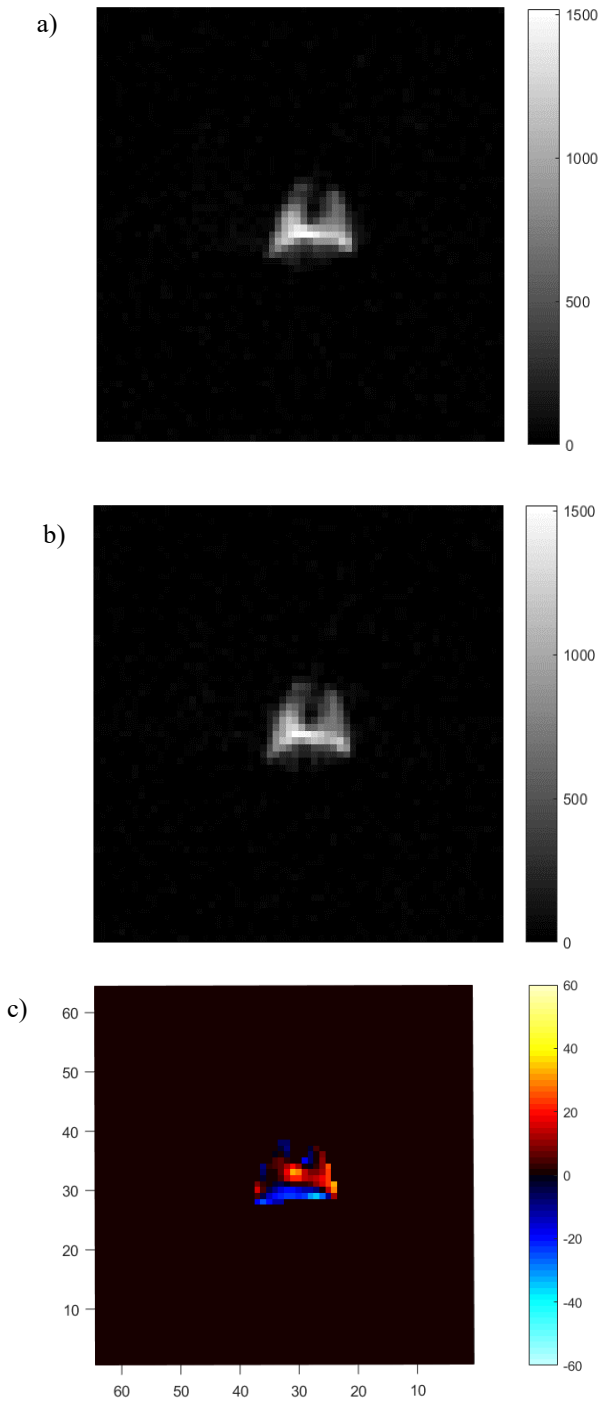

Figure B-8: a) Off-resonance image with SNR = 42.78; b) On-resonance image with SNR = 38.39; both a) and b) were produced using a 16 x 30 3-lobe sinc pulse, TR = 5s, flip angle = 15°, and pulse angle =140°. Signal percent depletion is 9.0 %.
c) Saturation map of figure B-8 a) and b).

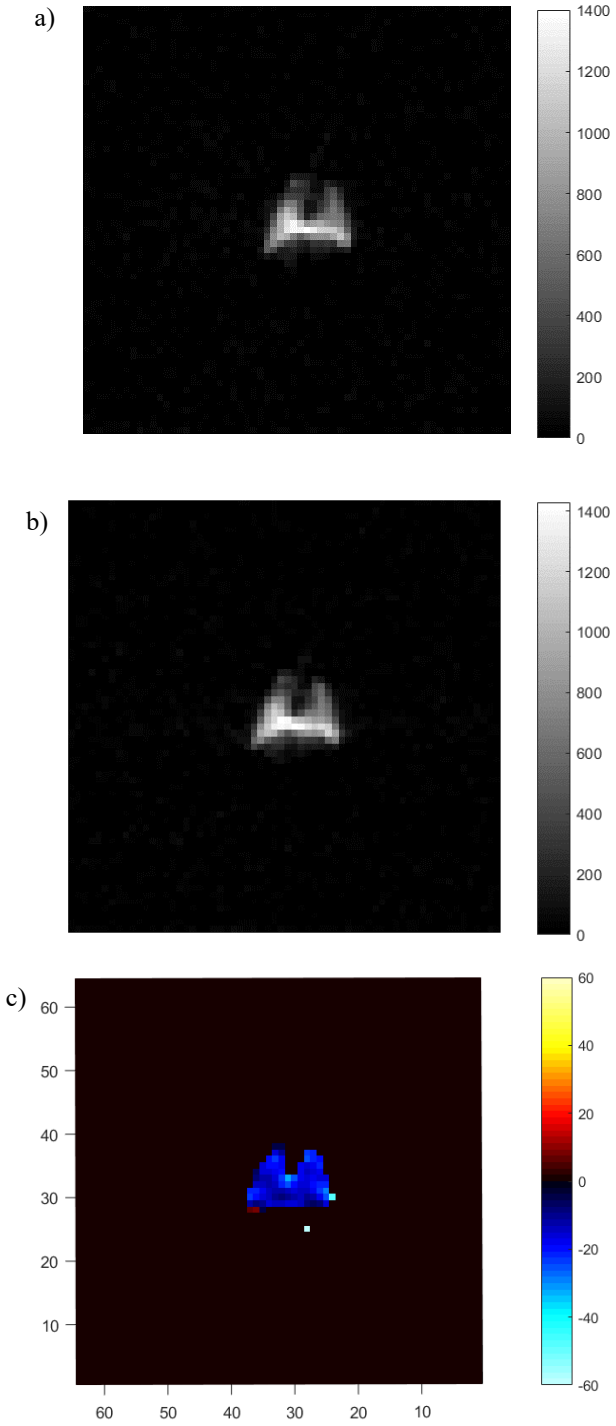

Figure B-9: a) Off-resonance image with SNR = 36.28; b) On-resonance image with SNR = 48.83; both a) and b) were produced using a 16 x 30 3-lobe sinc pulse, TR = 5s, flip angle = 15°, and pulse angle =140°. Signal percent depletion is -34.6 %. c) Saturation map of figure B-9 a) and b).

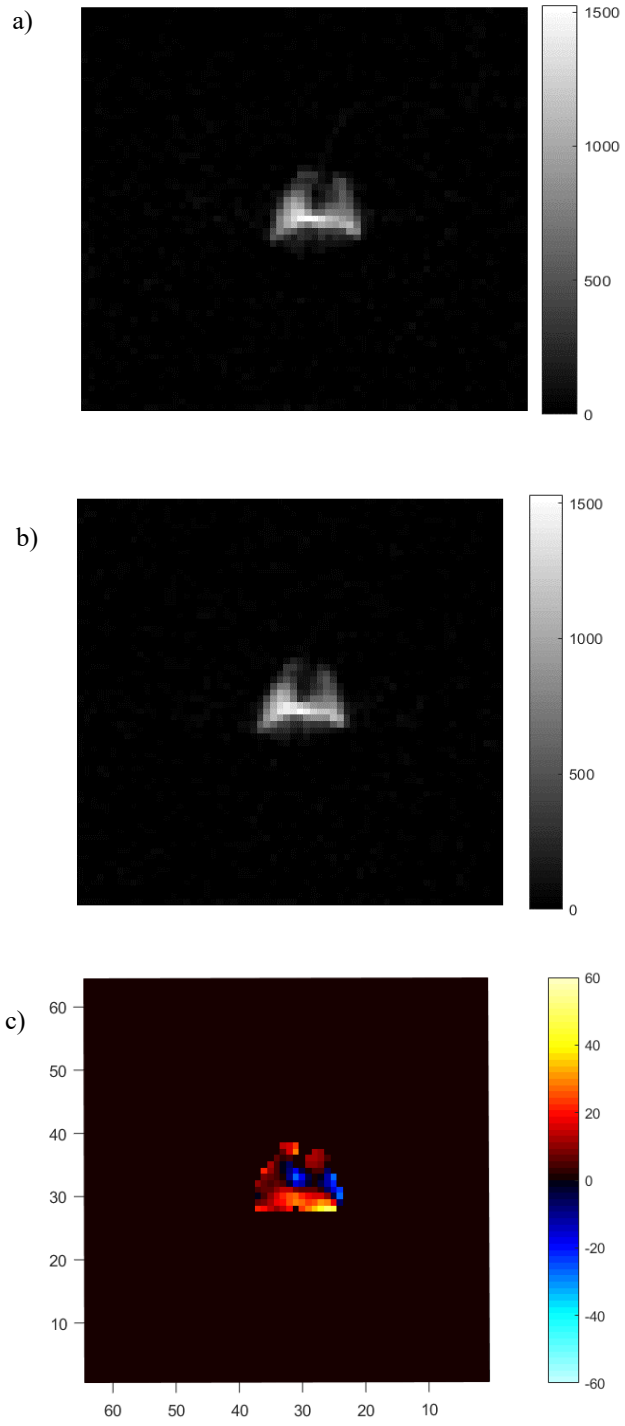

Figure B-10: a) Off-resonance image with SNR = 44.55; b) On-resonance image with SNR = 42.01. Both a) and b) were produced using a 16 x 30 3-lobe sinc pulse, TR = 5s, flip angle = 15°, and pulse angle =140°. Signal percent depletion is 5.70 %. c) Saturation map of figure B-10 a) and b).

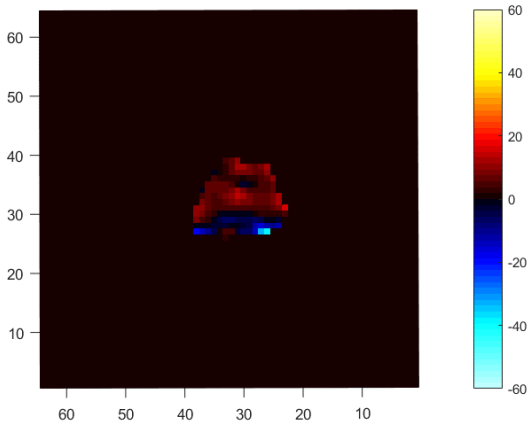

Figure B-11: Saturation map with five off-resonance (panel a of figures B-6 to B-10) and five on-resonance (panel b of figures B-6 to B-10) images.

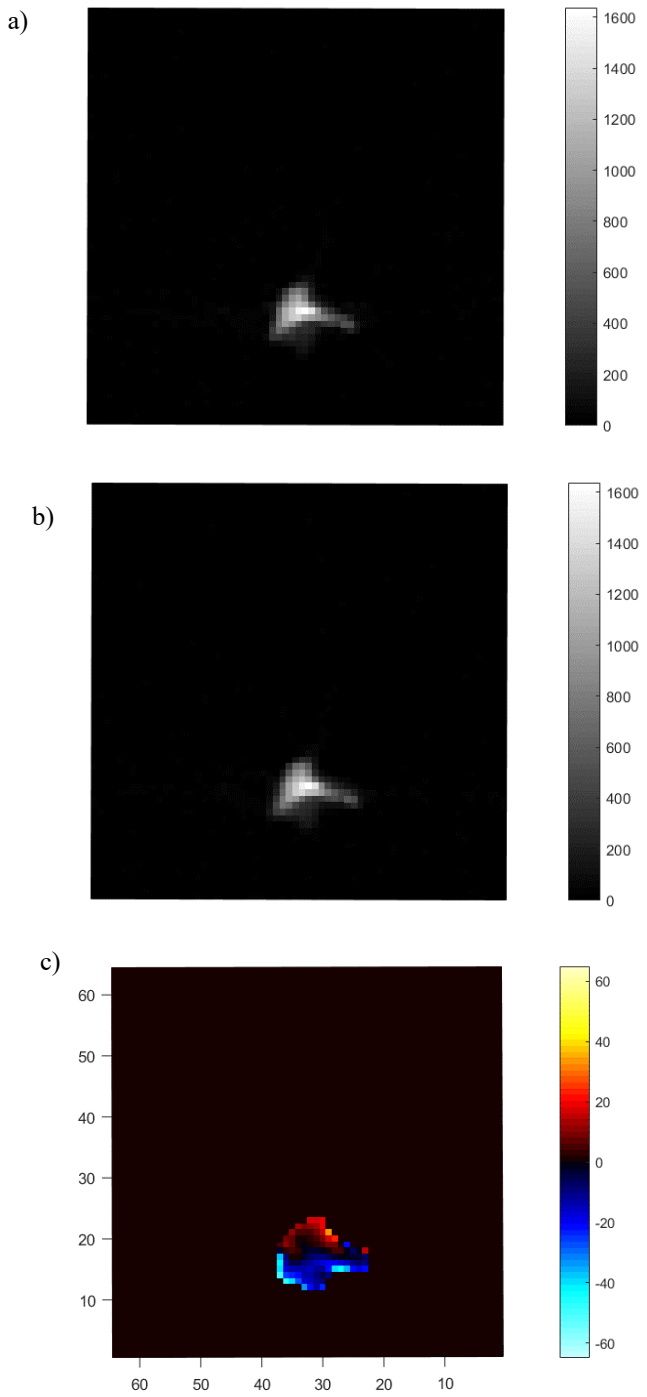

Figure B-12: a) Off-resonance image with SNR = 107; b) On-resonance image with SNR = 92. Both a) and b) were produced using a 16 x 30 3-lobe sinc pulse, TR = 5s, flip angle = 15°, and pulse angle =140°. Signal percent depletion is 14.0%. c) Saturation map of figure B-12 a) and b).

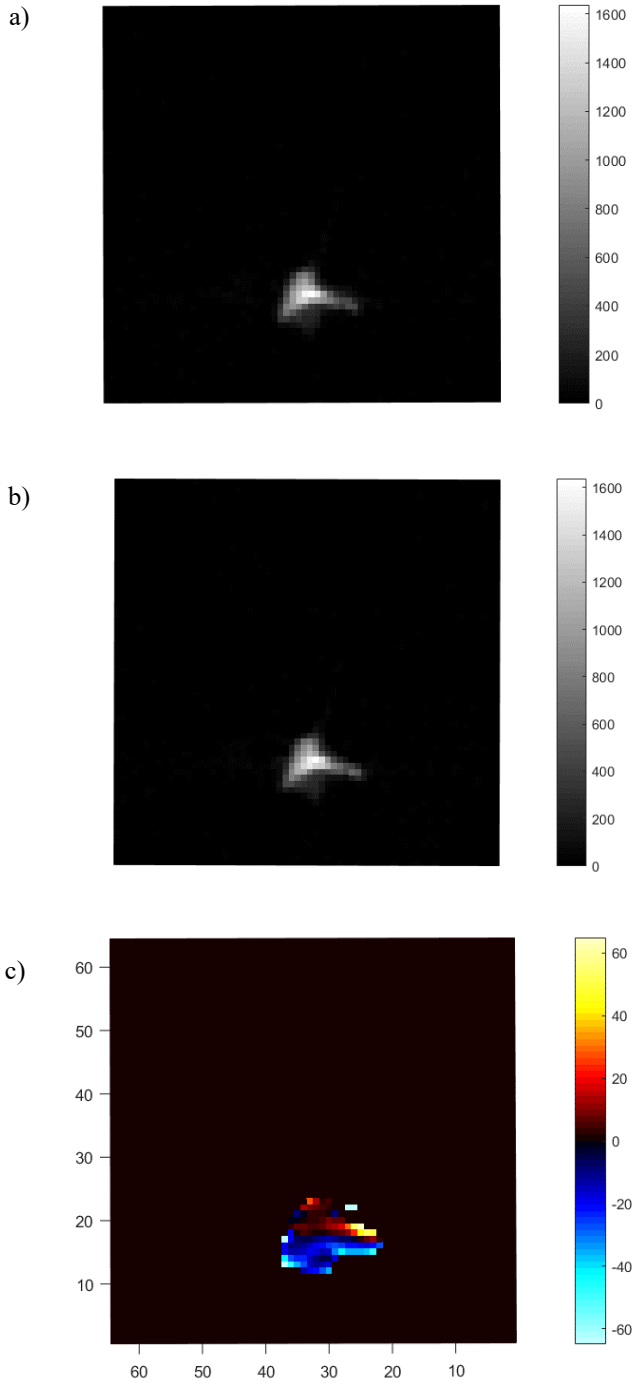

Figure B-13: a) Off-resonance image with SNR = 106; b) On-resonance image with SNR = 97. Both a) and b) were produced using a 16 x 30 3-lobe sinc pulse, TR = 5s, flip angle = 15°, and pulse angle =140°. Signal percent depletion is 8.49%. c) Saturation map of figure B-13 a) and b).

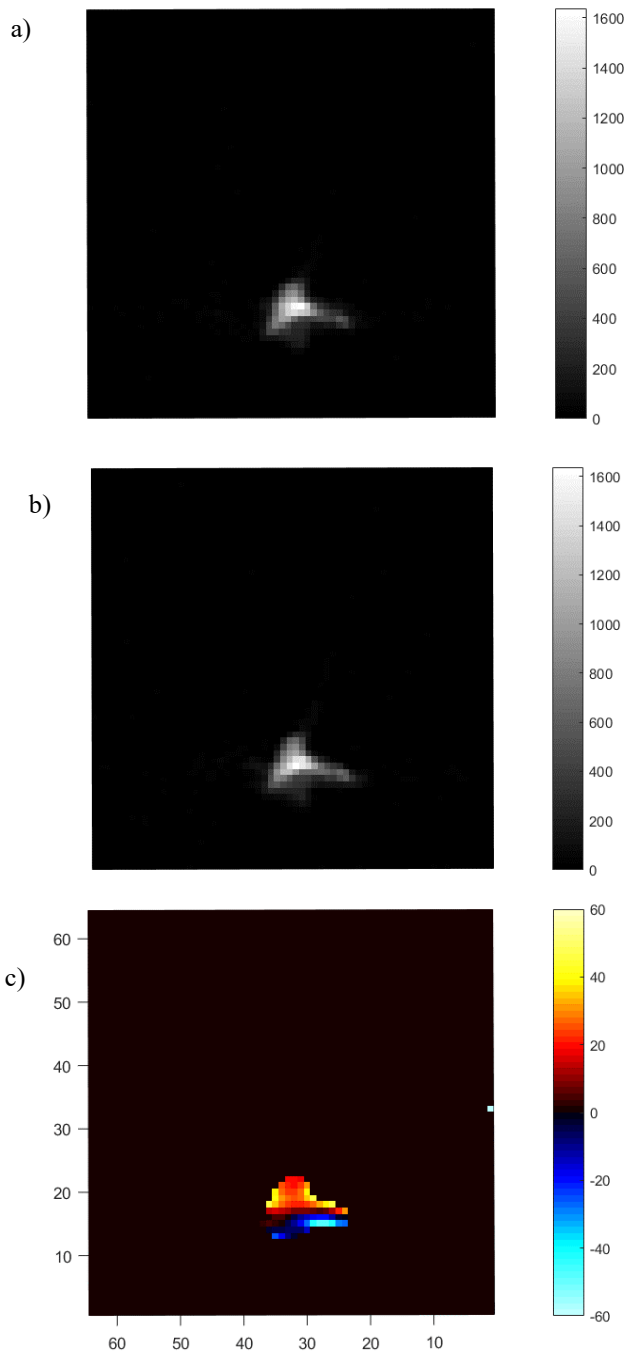

Figure B-14: a) Off-resonance image with SNR = 143; b) On-resonance image with SNR = 100. Both a) and b) were produced using a 16 x 30 3-lobe sinc pulse, TR = 5s, flip angle = 15°, and pulse angle =140°. Signal percent depletion is 30.1%. c) Saturation map of figure B-14 a) and b).

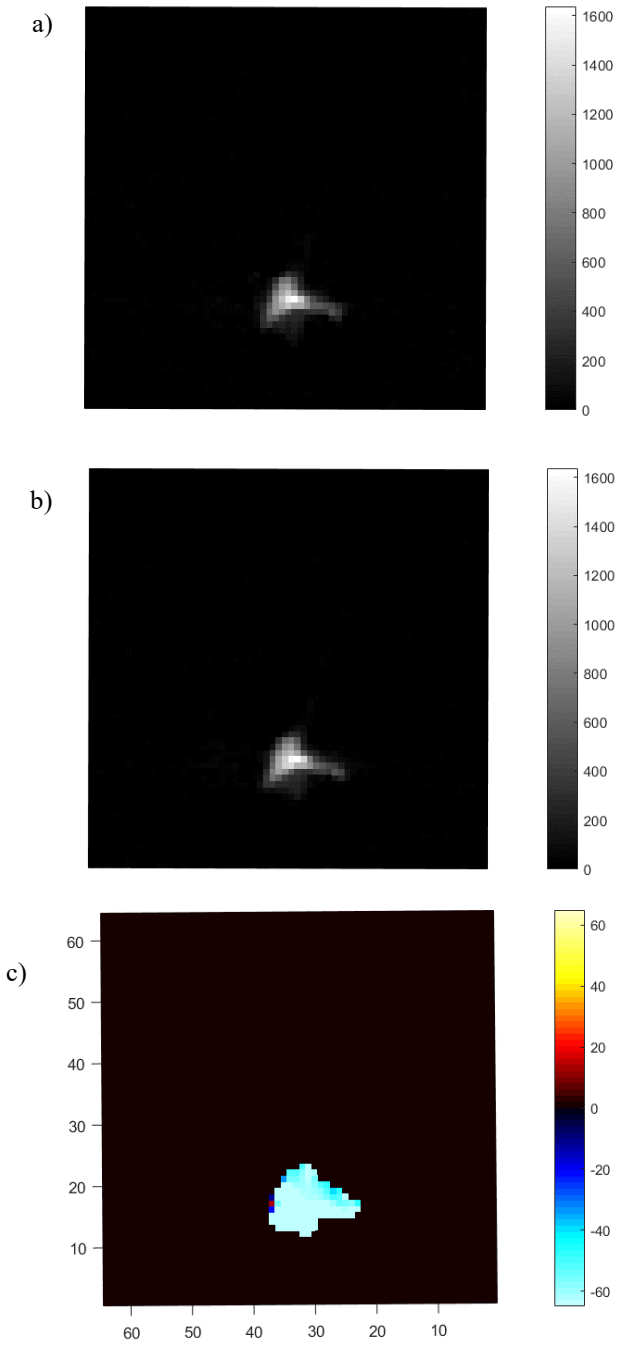

Figure B-15: a) Off-resonance image with SNR = 106; b) On-resonance image with SNR = 123. Both a) and b) were produced using a 16 x 30 3-lobe sinc pulse, TR = 5s, flip angle = 15°, and pulse angle =140°. Signal percent depletion is -23.0%. c) Saturation map of figure B-15 a) and b).

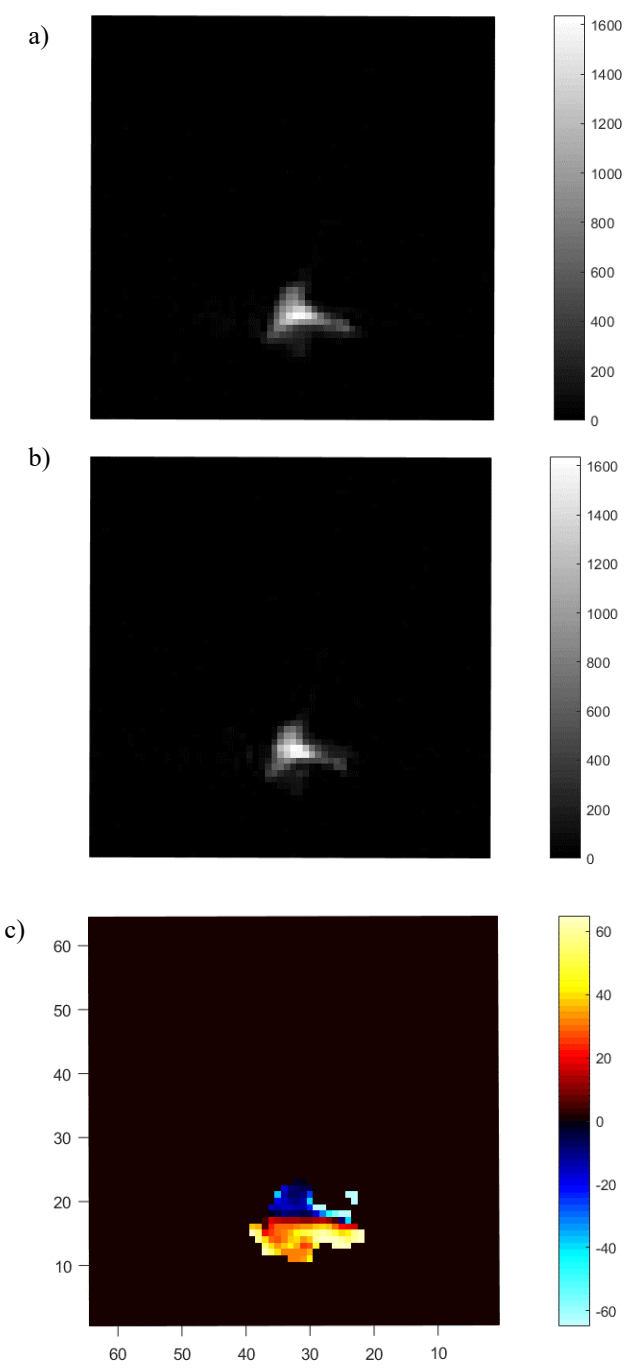

Figure B-16: a) Off-resonance image with SNR = 123; b) On-resonance image with SNR = 136. Both a) and b) were produced using a 16 x 30 3-lobe sinc pulse, TR = 5s, flip angle = 15°, and pulse angle =140°. Signal percent depletion is -10.6%. c) Saturation map of figure B-16 a) and b).

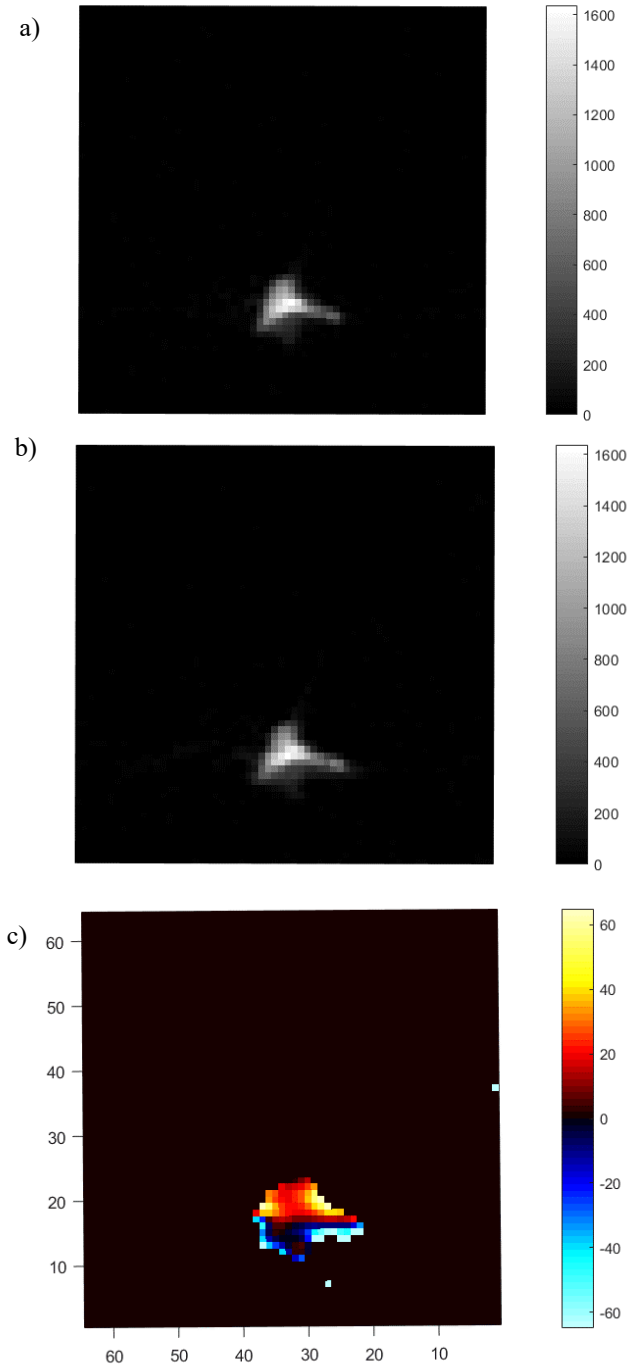

Figure B-17: a) Off-resonance image with SNR = 112; b) On-resonance image with SNR = 105. Both a) and b) were produced using a 16 x 30 3-lobe sinc pulse, TR = 5s, flip angle = 15°, and pulse angle =140°. Signal percent depletion is 6.25%. c) Saturation map of figure B-17 a) and b).

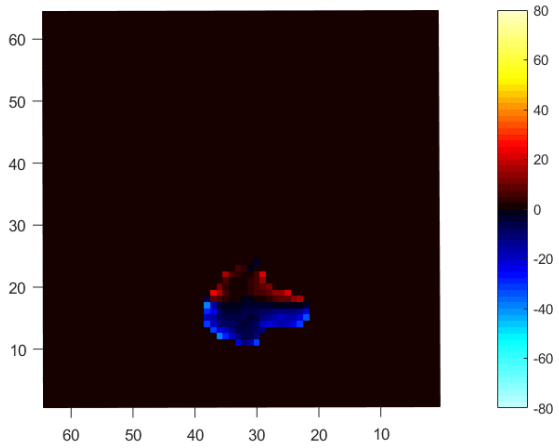

Figure B-18: Saturation map with six off-resonance images (panel a of figures B-12 to B-17) and six on-resonance images (panel b of figures B-12 to B-17).

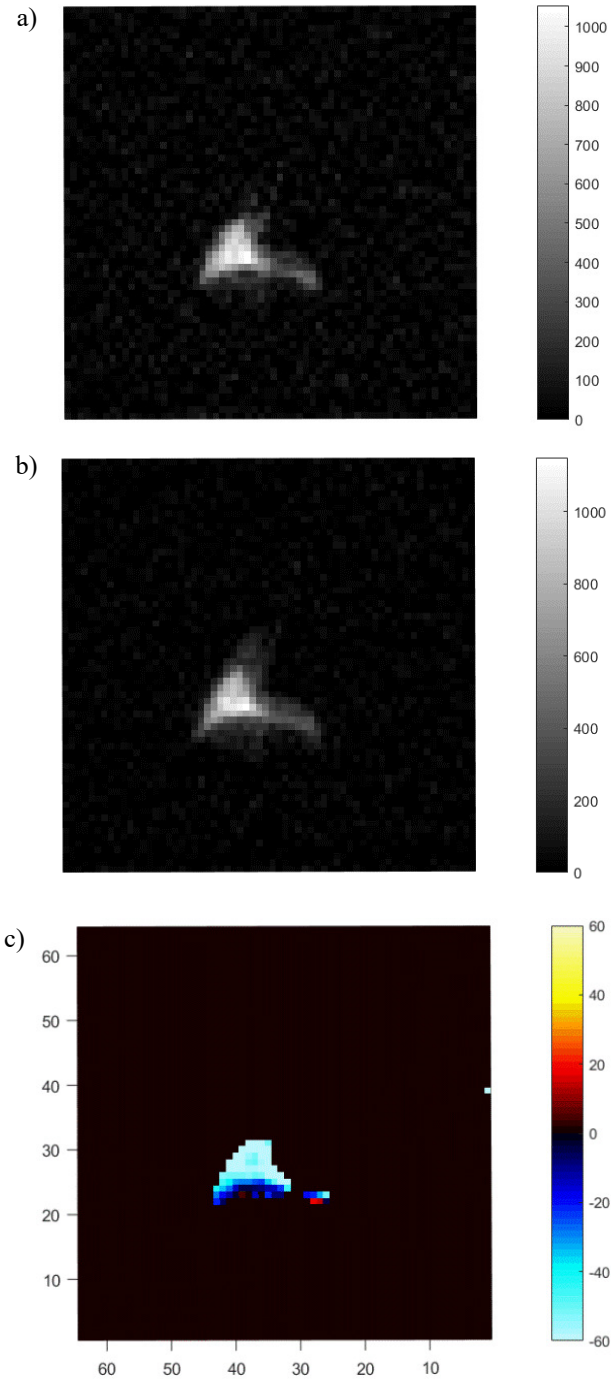

Figure B-18: a) Off-resonance image with SNR = 19.55; b) On-resonance image with SNR = 24.78. Both a) and b) were produced using a 16 x 30 3-lobe sinc pulse, TR = 5s, flip angle = 15°, and pulse angle =140°. c) Saturation map of figure B-18 a) and b).

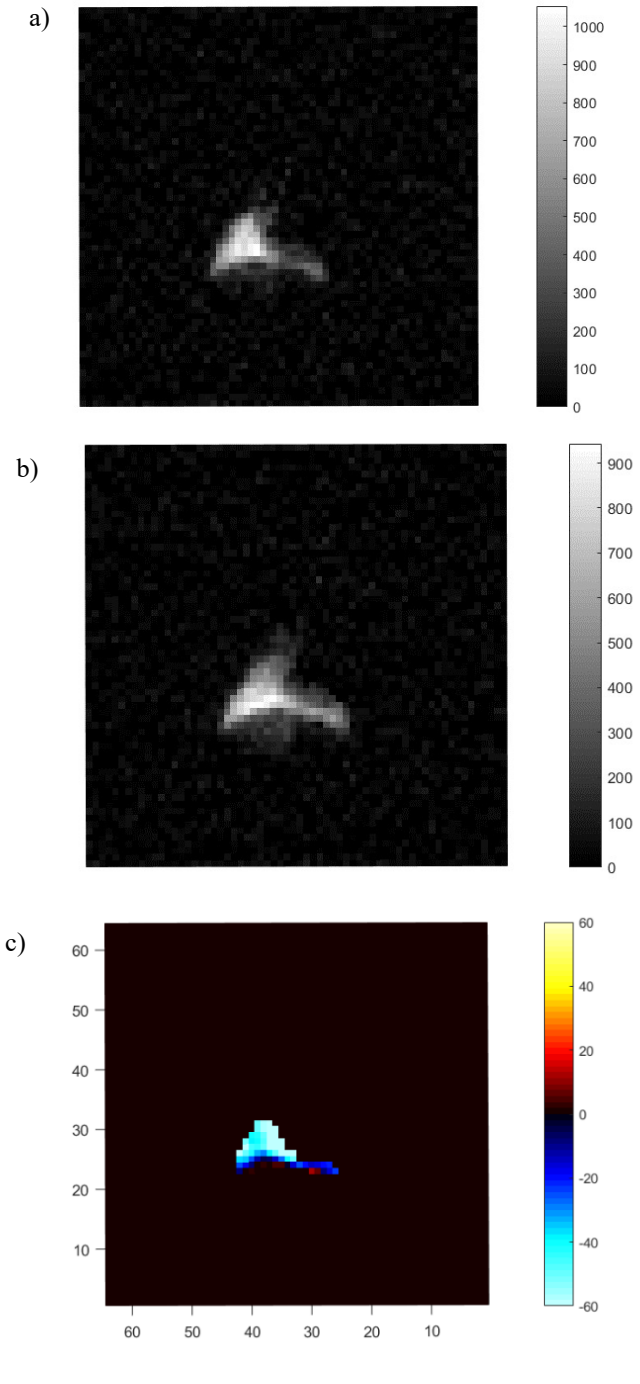

Figure B-19: a) Off-resonance image with SNR = 15.74; b) On-resonance image with SNR = 21.54. Both a) and b) were produced using a 16 x 30 3-lobe sinc pulse, TR = 5s, flip angle = 15°, and pulse angle =140°. Signal percent depletion is -26.75%. c) Saturation map of figure B-19 a) and b).

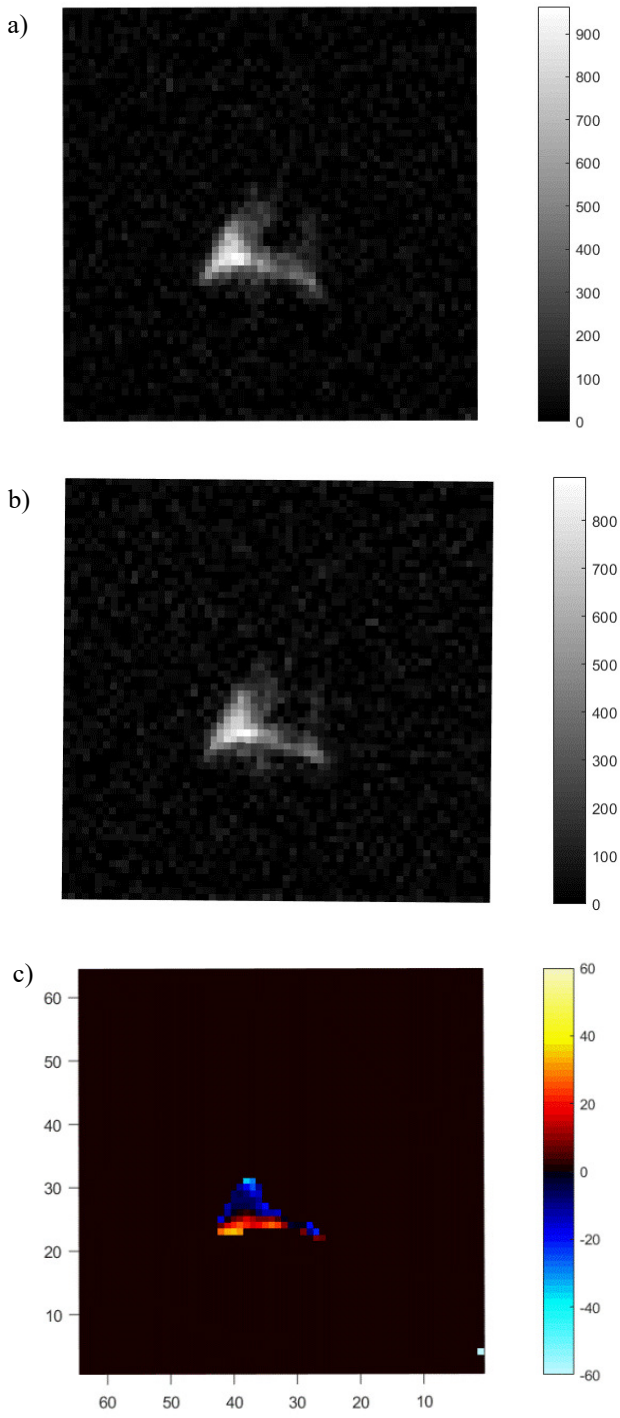

Figure B-20: a) Off-resonance image with SNR = 12.88; b) On-resonance image with SNR = 12.90. Both a) and b) were produced using a 16 x 30 3-lobe sinc pulse, TR = 5s, flip angle = 15°, and pulse angle =140°. Signal percent depletion is -0.155%. c) Saturation map of figure B-20 a) and b).

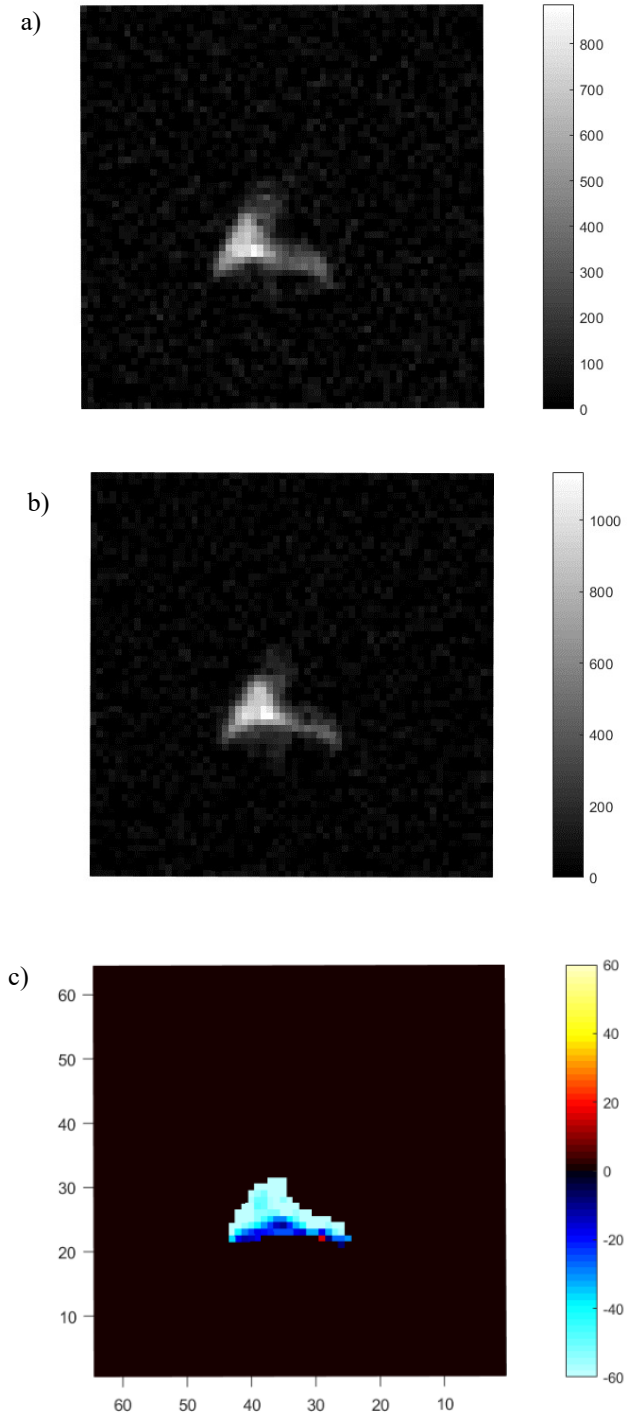

Figure B-21: a) Off-resonance image with SNR = 11.43; b) On-resonance image with SNR = 17.75. Both a) and b) were produced using a 16 x 30 3-lobe sinc pulse, TR = 5s, flip angle = 15°, and pulse angle =140°. Signal percent depletion is -55.3%. c) Saturation map of figure B-21 a) and b).

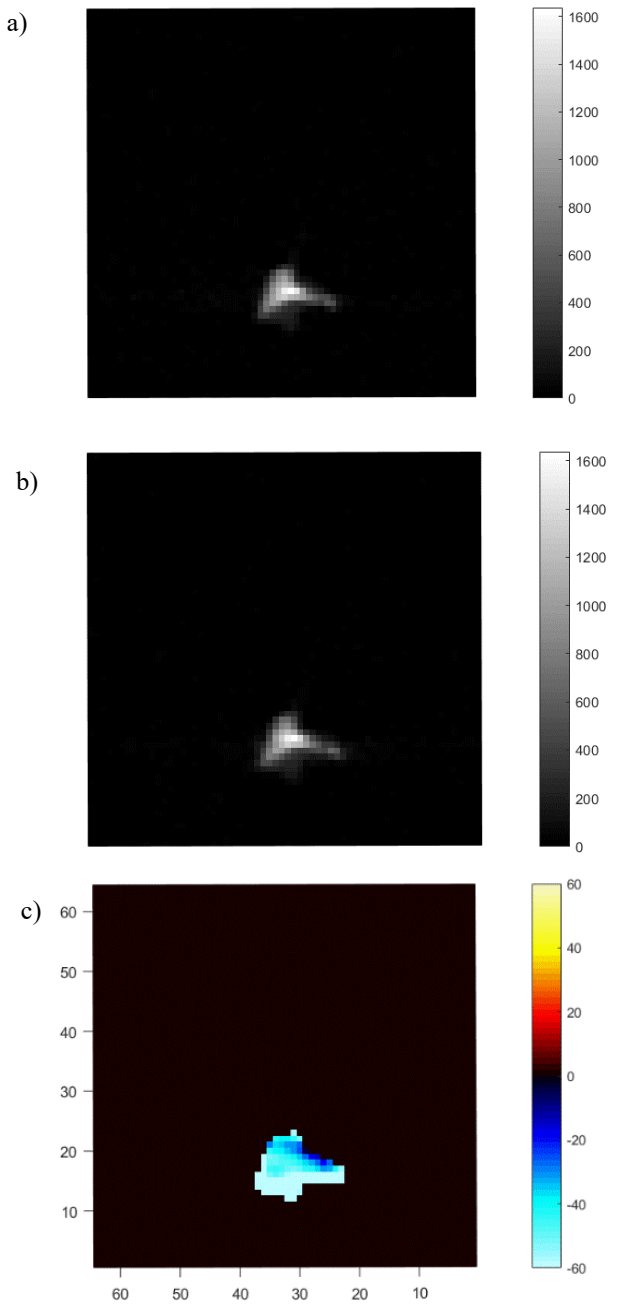

Figure B-22: a) Off-resonance image with SNR = 89.58; b) On-resonance image with SNR = 125.48. Both a) and b) were produced using a 16 x 30 3-lobe sinc pulse, TR = 6s, flip angle = 10°, and pulse angle =140°. c) Saturation map of figure B-22 a) and b).

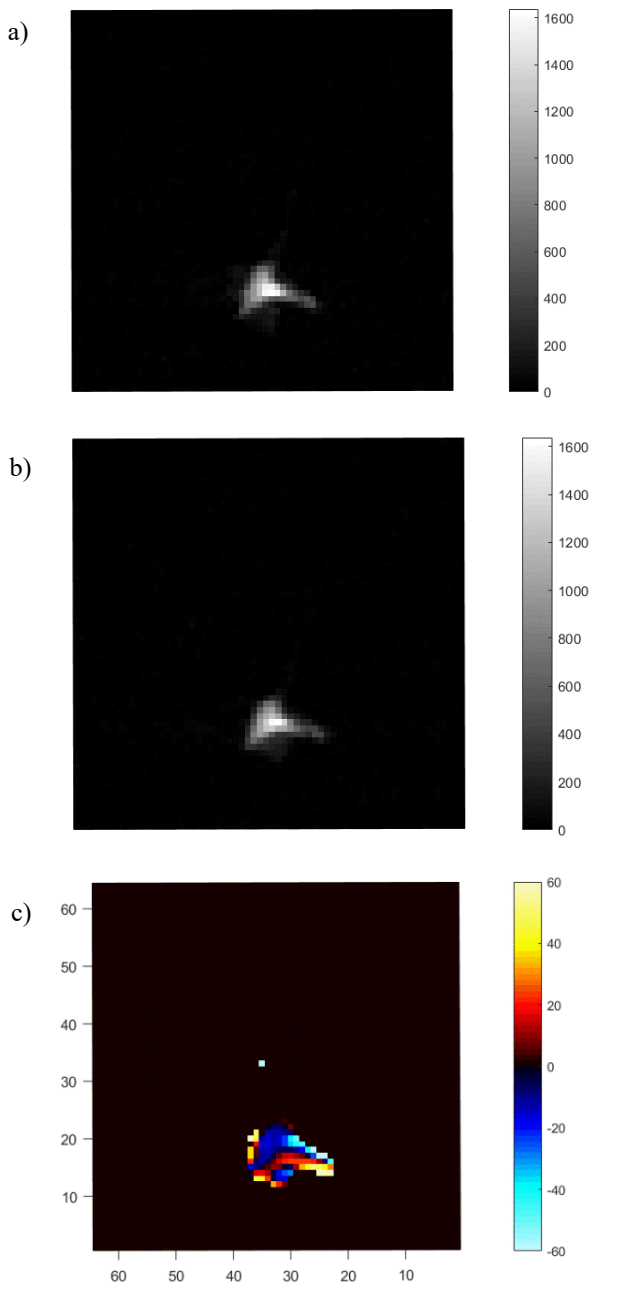

Figure B-23: a) Off-resonance image with SNR = 82.55; b) On-resonance image with SNR = 90.95. Both a) and b) were produced using a 16 x 30 3-lobe sinc pulse, TR = 6s, flip angle = 10°, and pulse angle =140°. c) Saturation map of figure B-23 a) and b).

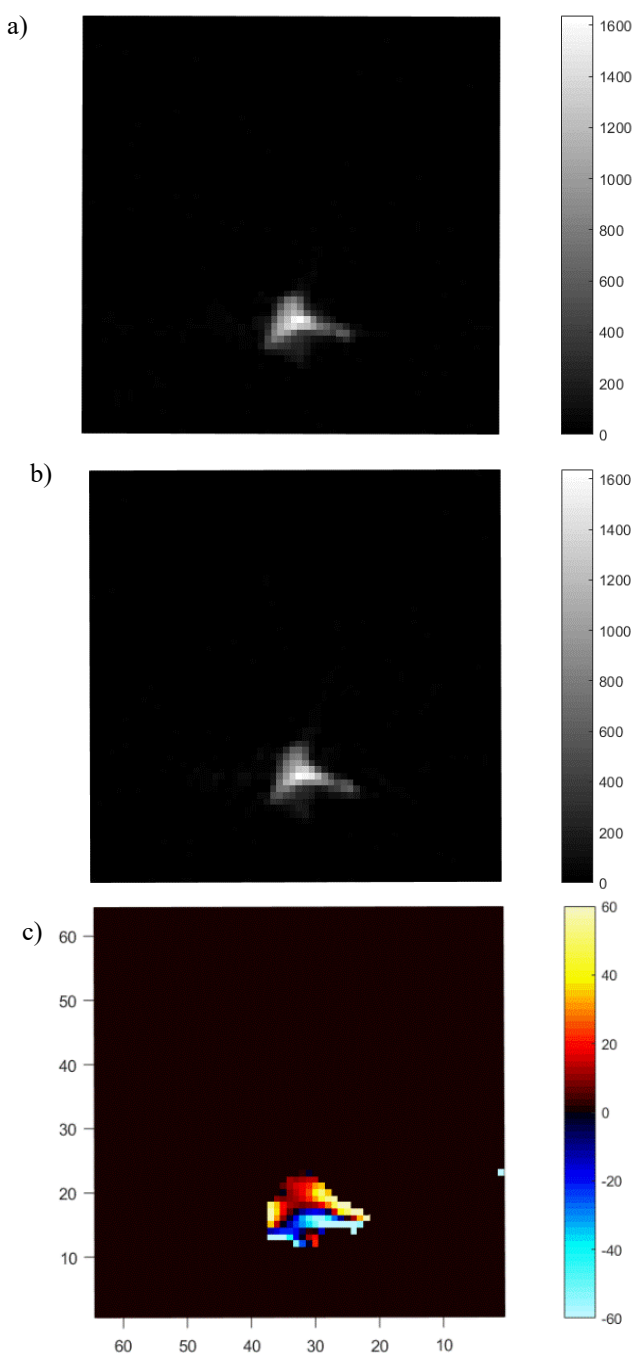

Figure B-24: a) Off-resonance image with SNR = 119.58; b) On-resonance image with SNR = 105.67. Both a) and b) were produced using a 16 x 30 3-lobe sinc pulse, TR = 6s, flip angle = 10°, and pulse angle =140°. c) Saturation map of figure B-24 a) and b).

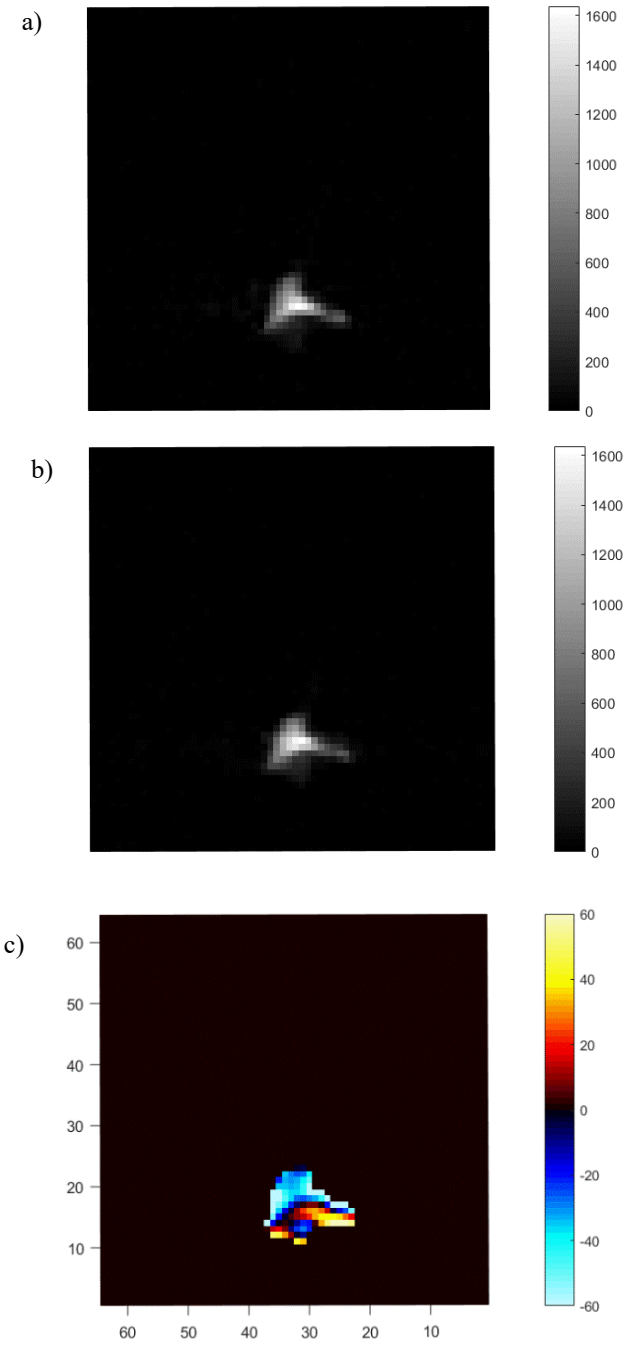

Figure B-25: a) Off-resonance image with SNR = 85.55; b) On-resonance image with SNR = 95.3. Both a) and b) were produced using a 16 x 30 3-lobe sinc pulse, TR = 6s, flip angle = 10°, and pulse angle =140°. c) Saturation map of figure B-25 a) and b).

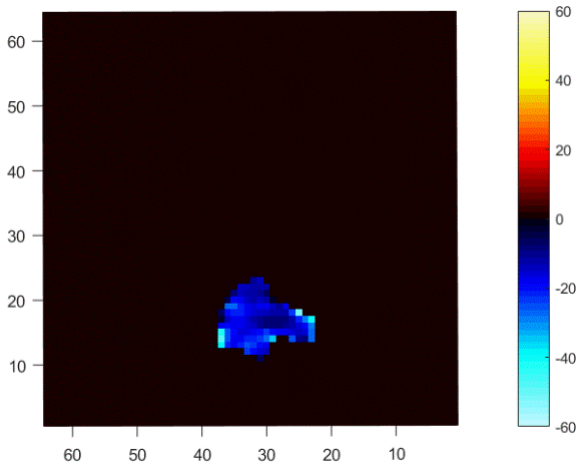

Figure B-26: Saturation map that consists of four off-resonance and four on-resonance images.

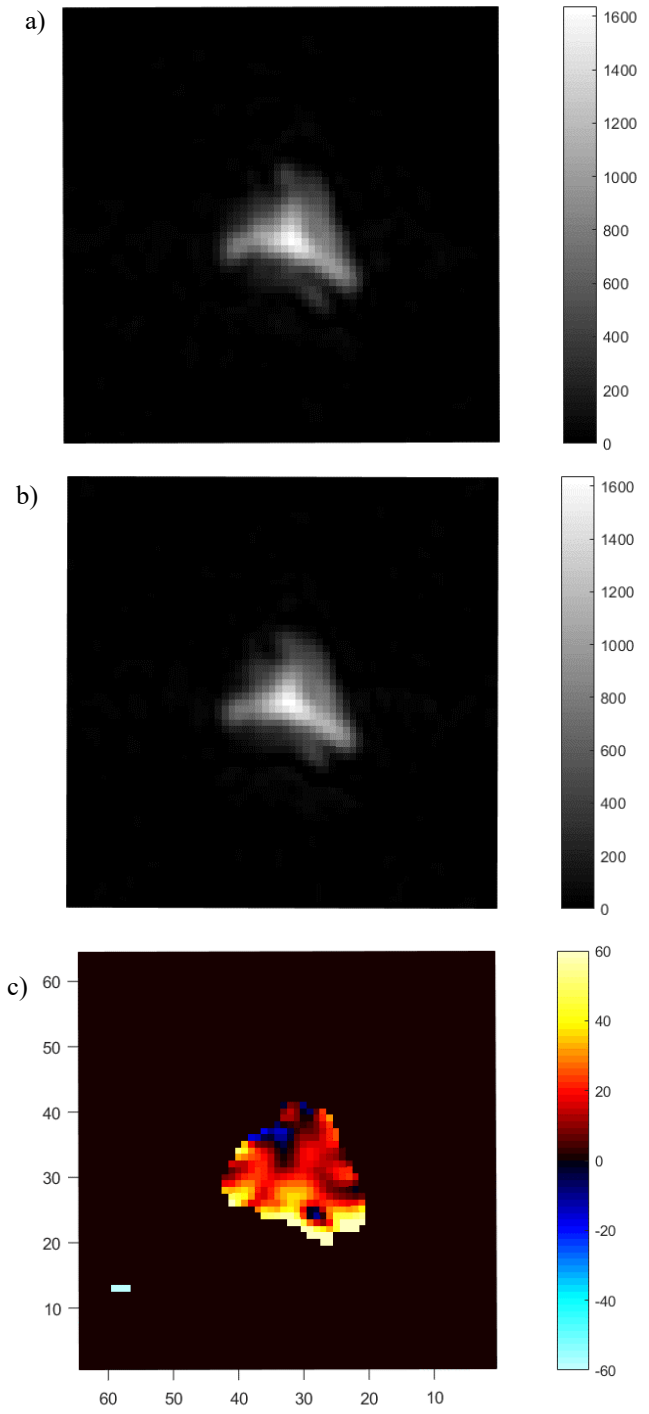

Figure B-27: a) Off-resonance image with SNR = 116.82; b) On-resonance image with SNR = 115.49. Both a) and b) were produced using a 32 x 32 3-lobe sinc pulse, TR = 5s, flip angle = 10°, and pulse angle =140°. c) Saturation map of figure B-27 a) and b).

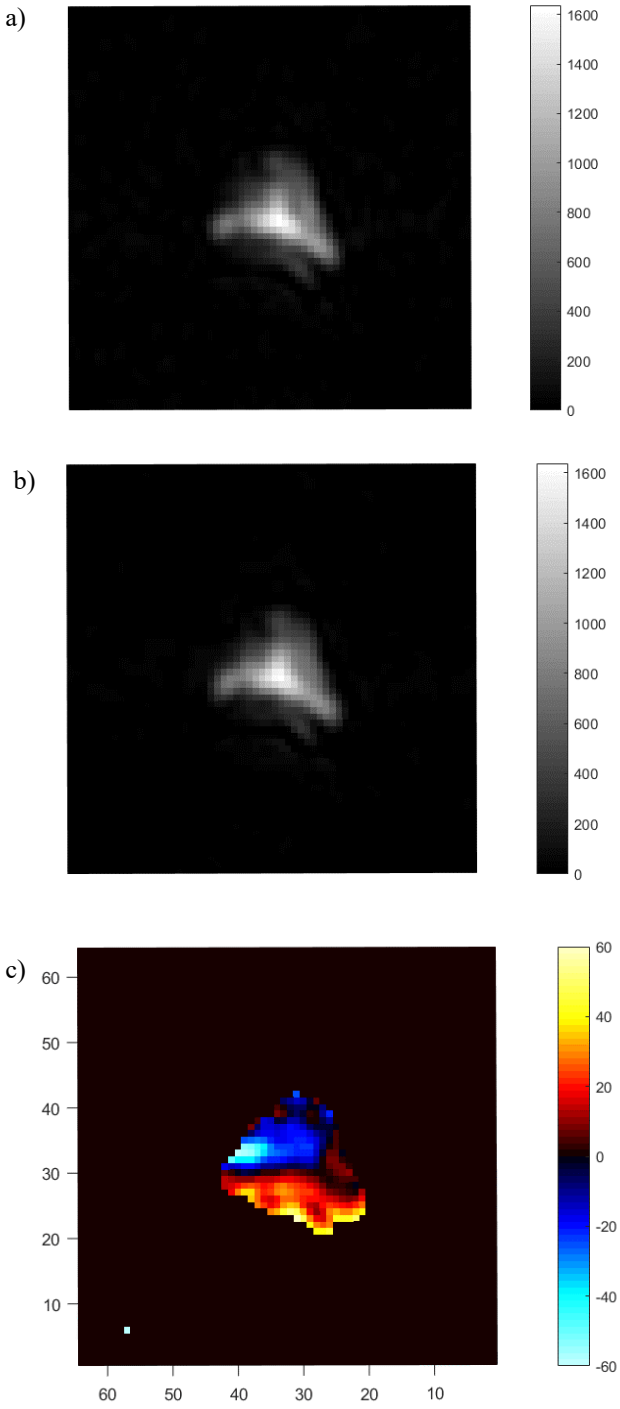

Figure B-28: a) Off-resonance image with SNR = 85.55; b) On-resonance image with SNR = 95.32; both a) and b) were produced using a 32 x 32 3-lobe sinc pulse, TR = 6s, flip angle = 10°, and pulse angle =140°. c) Saturation map of figure B-28 a) and b).

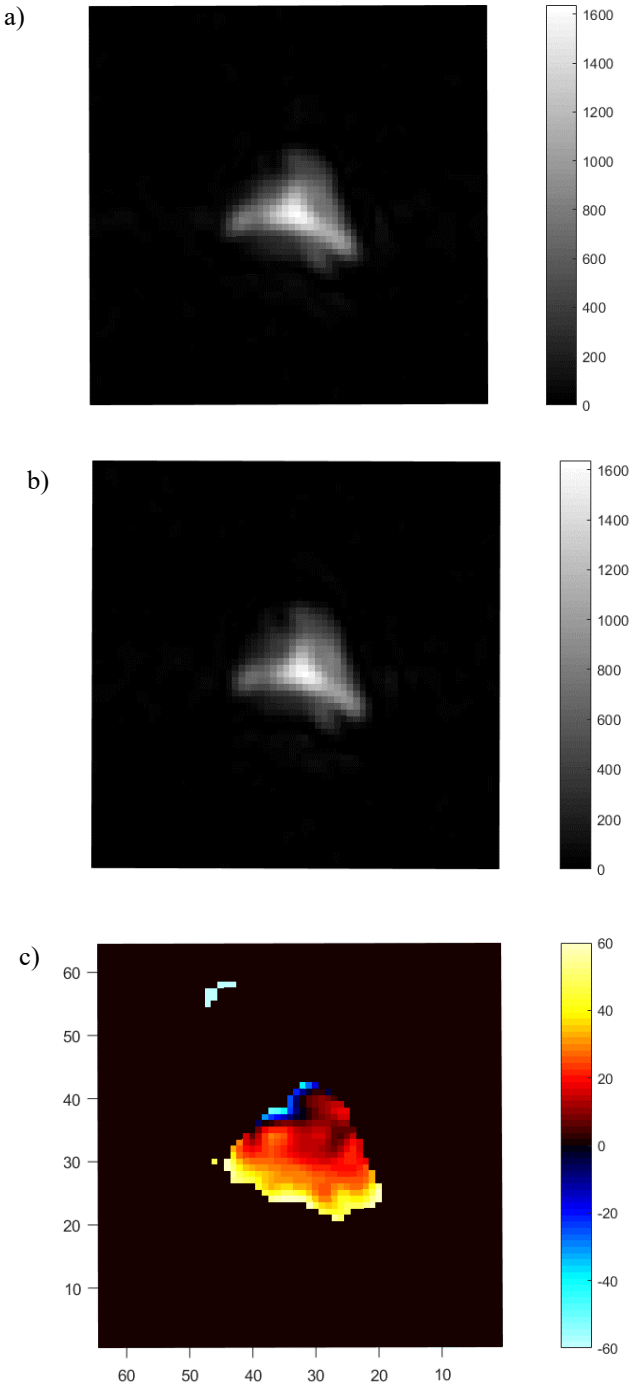

Figure B-29: a) Off-resonance image with SNR = 129.59; b) On-resonance image with SNR = 107.00; both a) and b) were produced using a 32 x 32 3-lobe sinc pulse, TR = 5s, flip angle = 10°, and pulse angle =140°. c) Saturation map of figure B-29 a) and b).

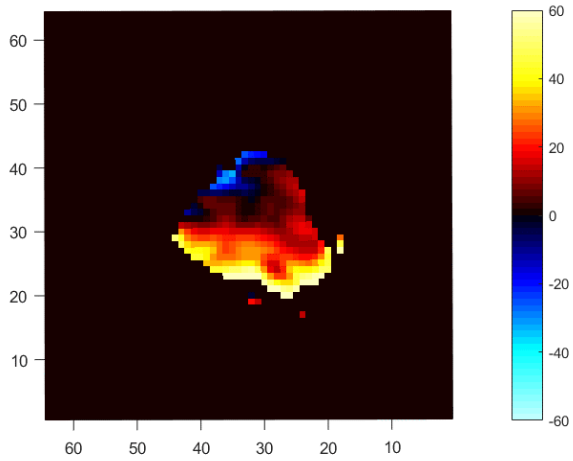

Figure B-30: Saturation map consisting of 3 off-resonance images (panel a of figures A-27, A-28, and A-29) and 3 on-resonance images (panel b of figures B-27, B-28, and B-29).

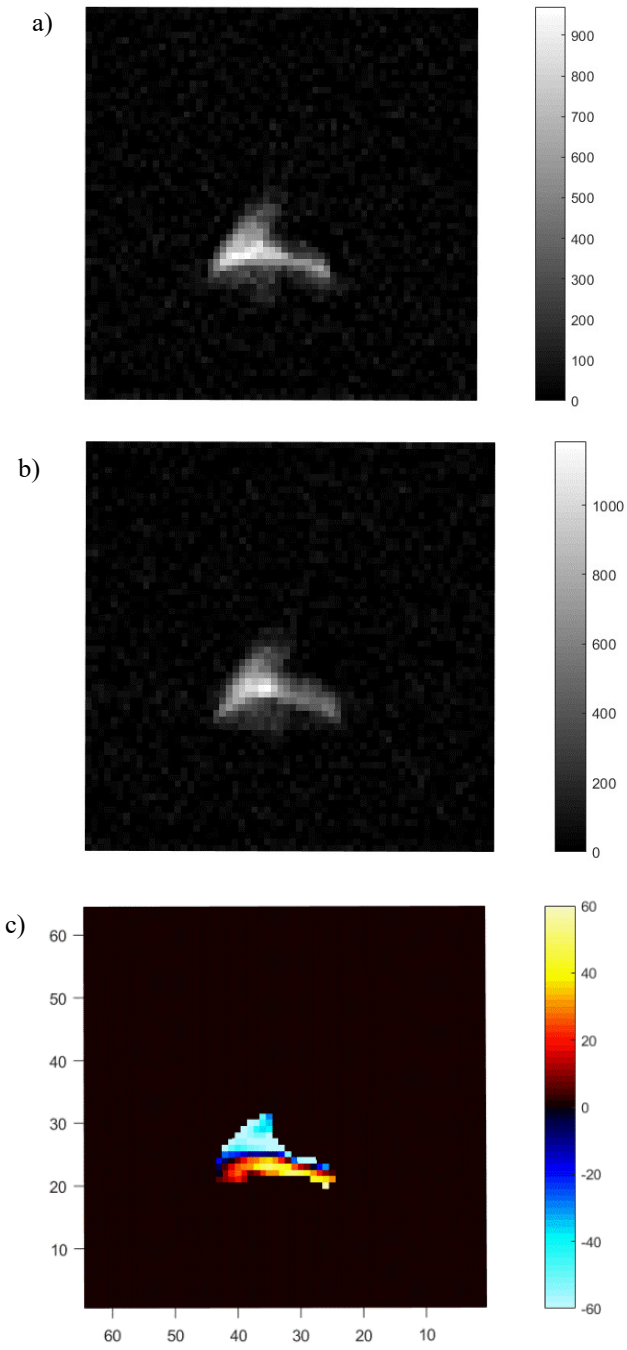

Figure B-31: a) Off-resonance image with SNR = 15.92; b) On-resonance image with SNR = 20.68. Both a) and b) were produced using a 16 x 30 3-lobe sinc pulse, TR = 5s, flip angle = 15°, and pulse angle =140°. Signal percent depletion is -29.9%. c) saturation map of figure B-31 a) and b).

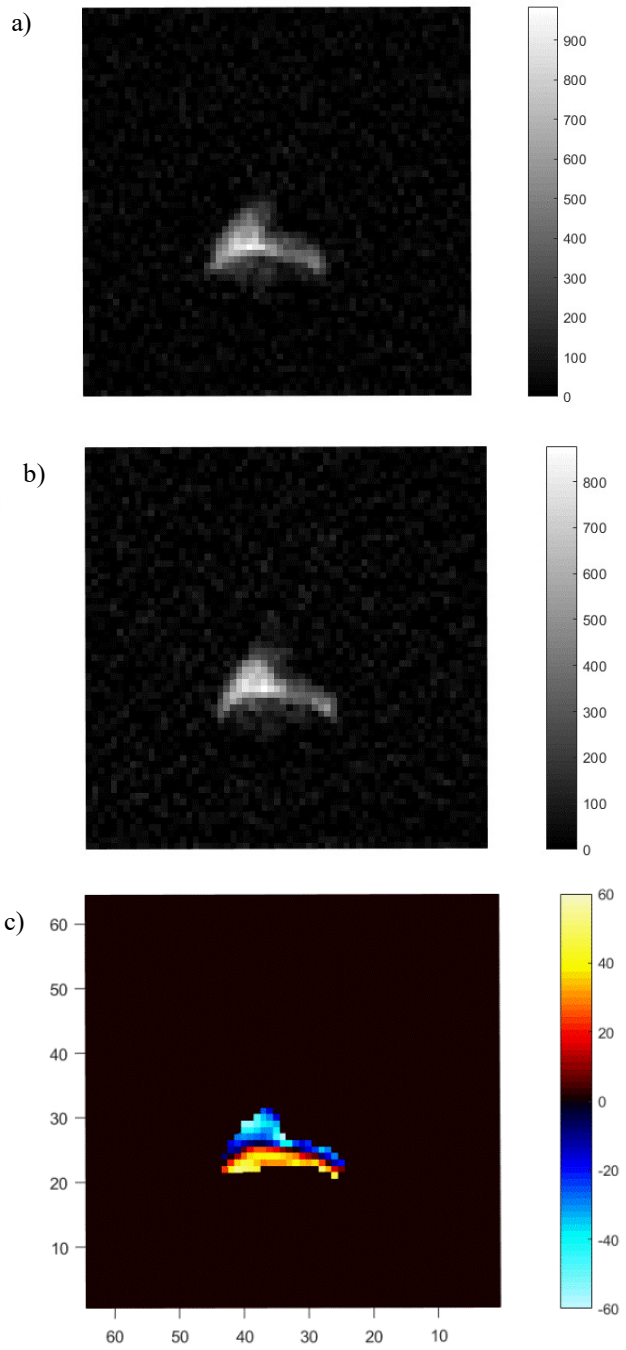

Figure B-32: a) Off-resonance image with SNR = 16.60; b) On-resonance image with SNR = 20.58. Both a) and b) were produced using a 16 x 30 3-lobe sinc pulse, TR = 5s, flip angle = 15°, and pulse angle =140°. c) Saturation map of figure B-32 a) and b).

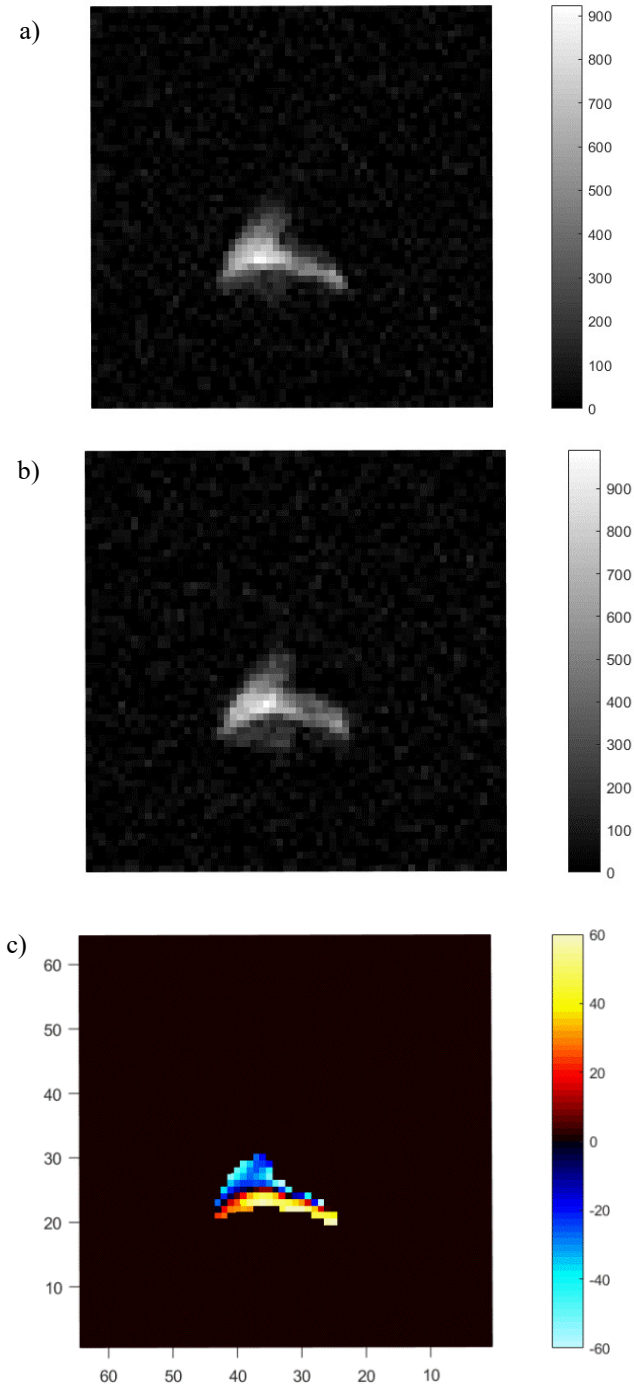

Figure B-33: a) Off-resonance image with SNR = 15.42; b) On-resonance image with SNR = 15.72. Both a) and b) were produced using a 16 x 30 3-lobe sinc pulse, TR = 5s, flip angle = 15°, and pulse angle =140°. c) Saturation map of figure B-33 a) and b).

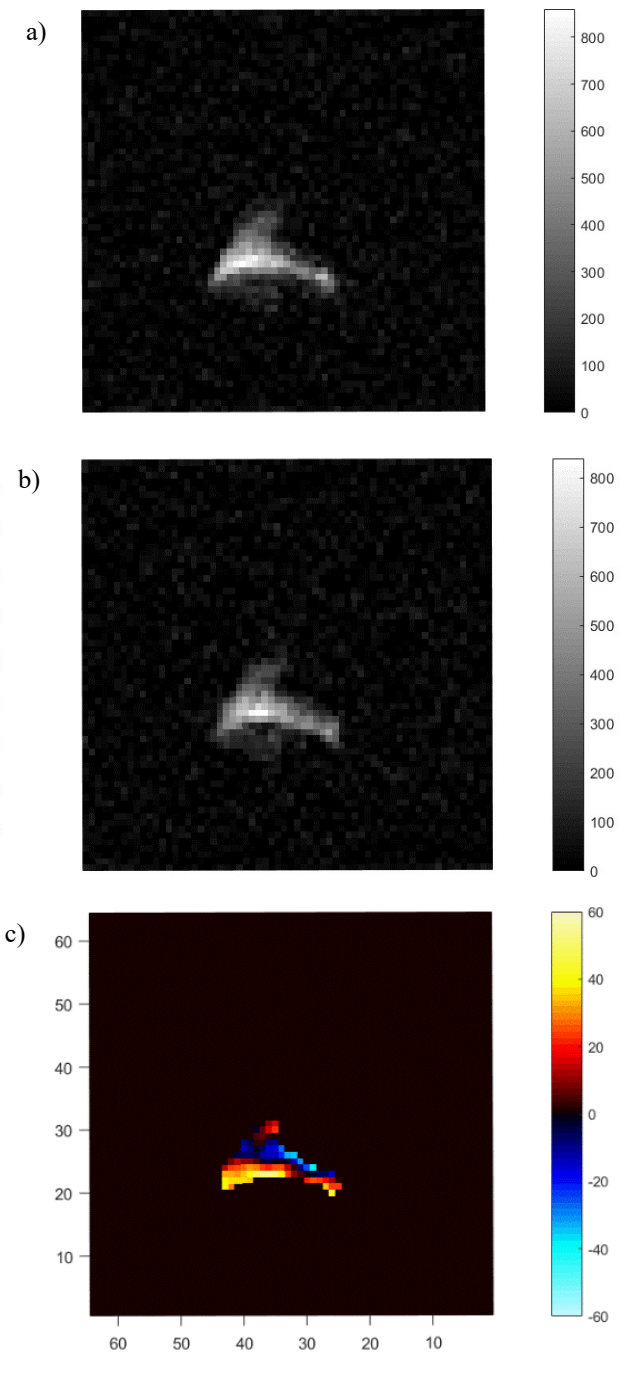

Figure B-34: a) Off-resonance image with SNR = 12.94; b) On-resonance image with SNR = 14.37. Both a) and b) were produced using a 16 x 30 3-lobe sinc pulse, TR = 5s, flip angle = 15°, and pulse angle =140°. c) Saturation map of figure B-34 a) and b).

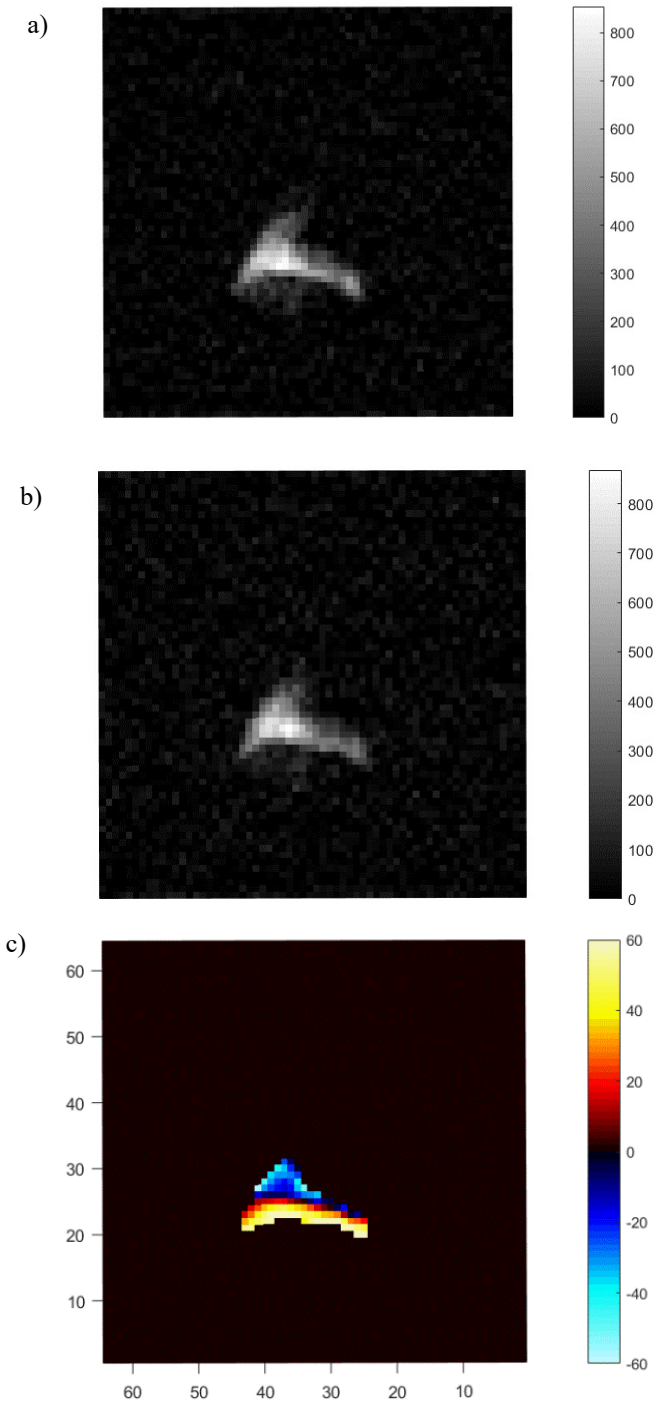

Figure B-35: a) Off-resonance image with SNR = 16.44; b) On-resonance image with SNR = 13.73. Both a) and b) were produced using a 16 x 30 3-lobe sinc pulse, TR = 5s, flip angle = 15°, and pulse angle =140°. c) Saturation map of figure B-35 a) and b).

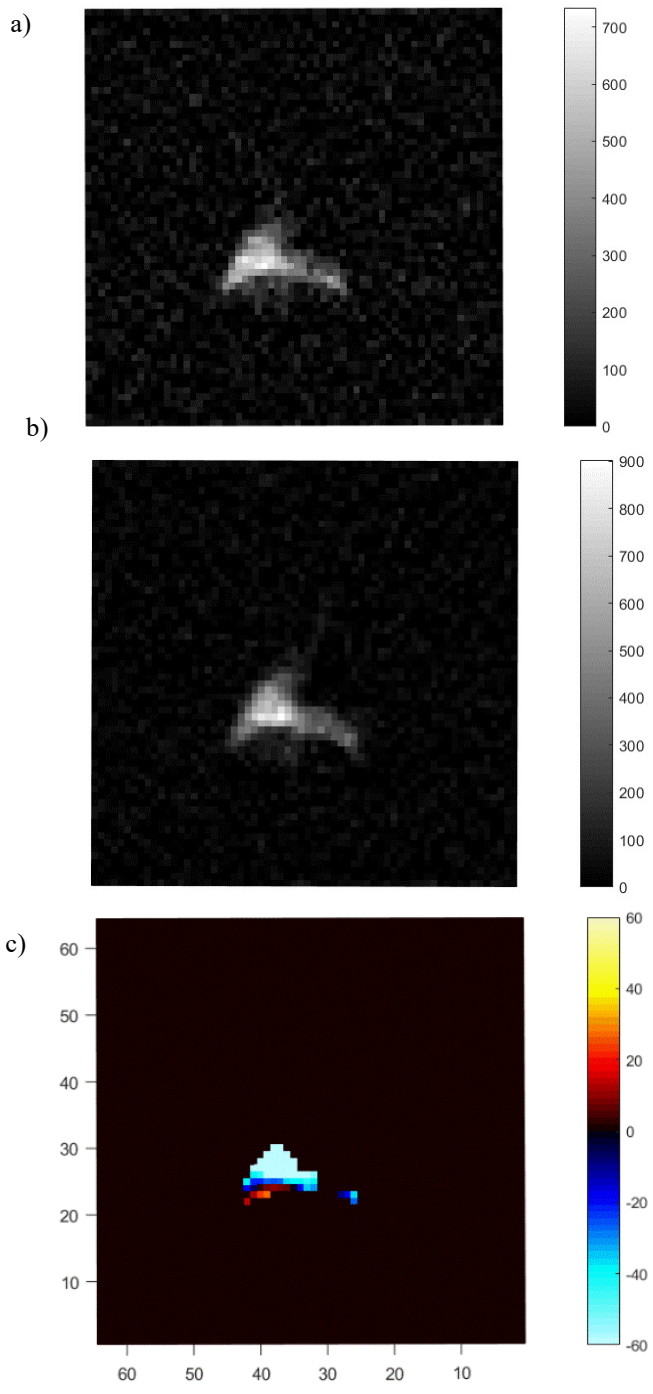

Figure B-36: a) Off-resonance image with SNR = 14.20; b) On-resonance image with SNR = 16.47. Both a) and b) were produced using a 16 x 30 3-lobe sinc pulse, TR = 5s, flip angle = 15°, and pulse angle =140°. c) Saturation map of figure B-36 a) and b).

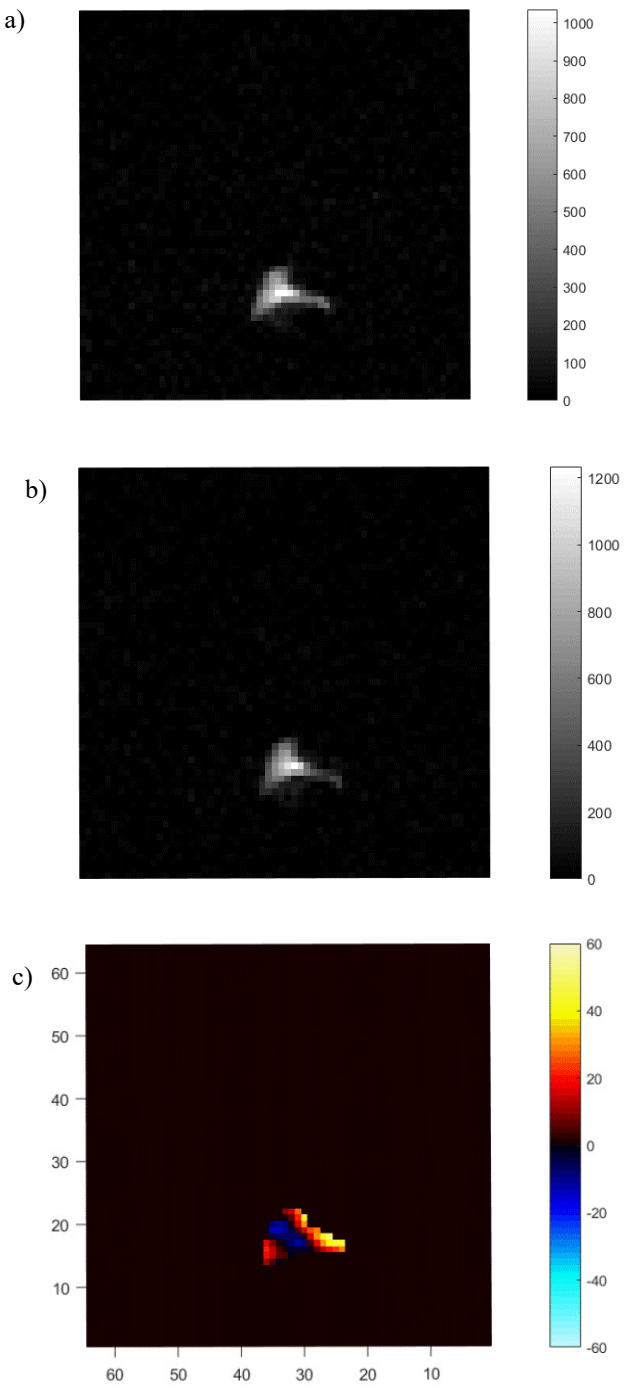

Figure B-37: a) Off-resonance image with SNR = 32.18; b) On-resonance image with SNR = 25.67. Both a) and b) were produced using a 32 x 30 3-lobe sinc pulse, TR = 5s, flip angle = 10°, and pulse angle =140°. c) Saturation map of figure B-37 a) and b).

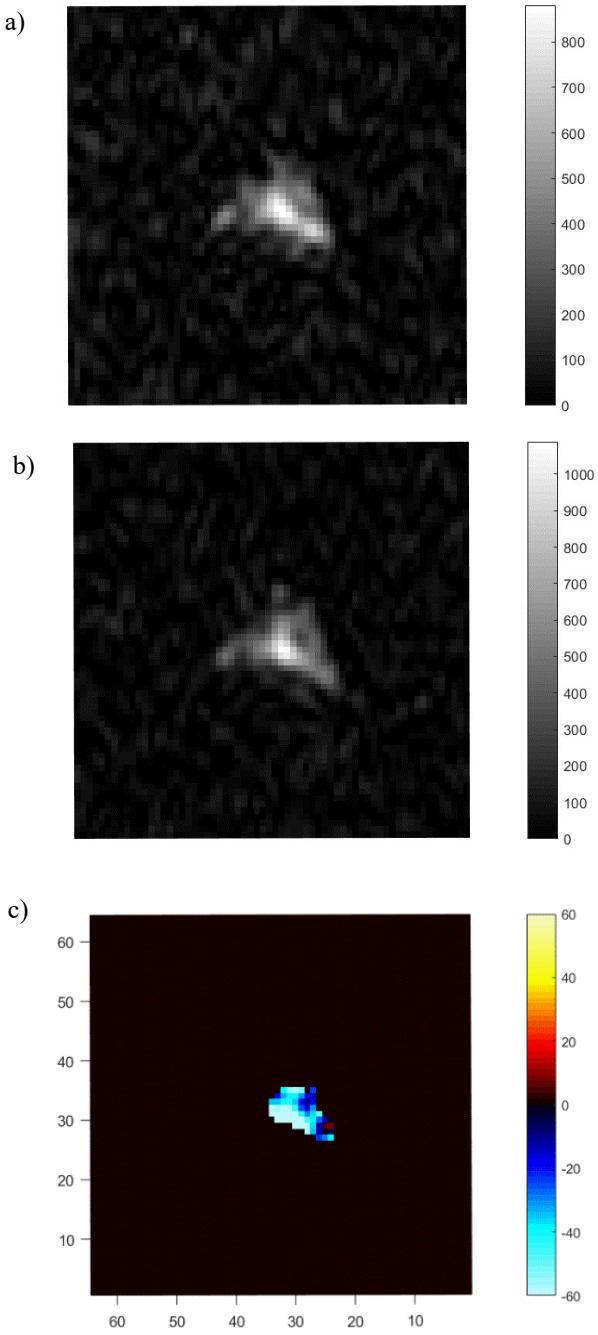

Figure B-38: a) Off-resonance image with SNR = 13.48; b) On-resonance image with SNR = 21.26. Both a) and b) were produced using a 16 x 30 3-lobe sinc pulse, TR = 6s, flip angle = 10°, and pulse angle =140°. c) Saturation map of figure B-38 a) and b).

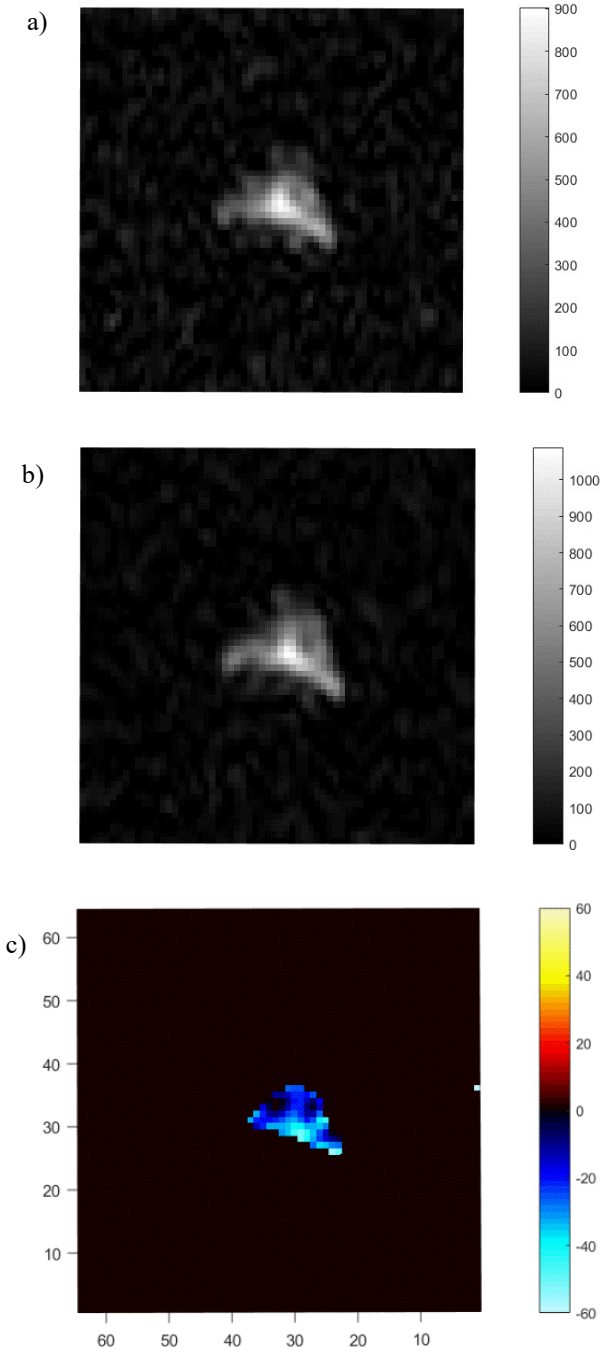

Figure B-39: a) Off-resonance image with SNR = 13.48; b) On-resonance image with SNR = 21.26. Both a) and b) were produced using a 16 x 30 3-lobe sinc pulse, TR = 6s, flip angle = 10°, and pulse angle =140°. c) Saturation map of figure B-39 a) and b).

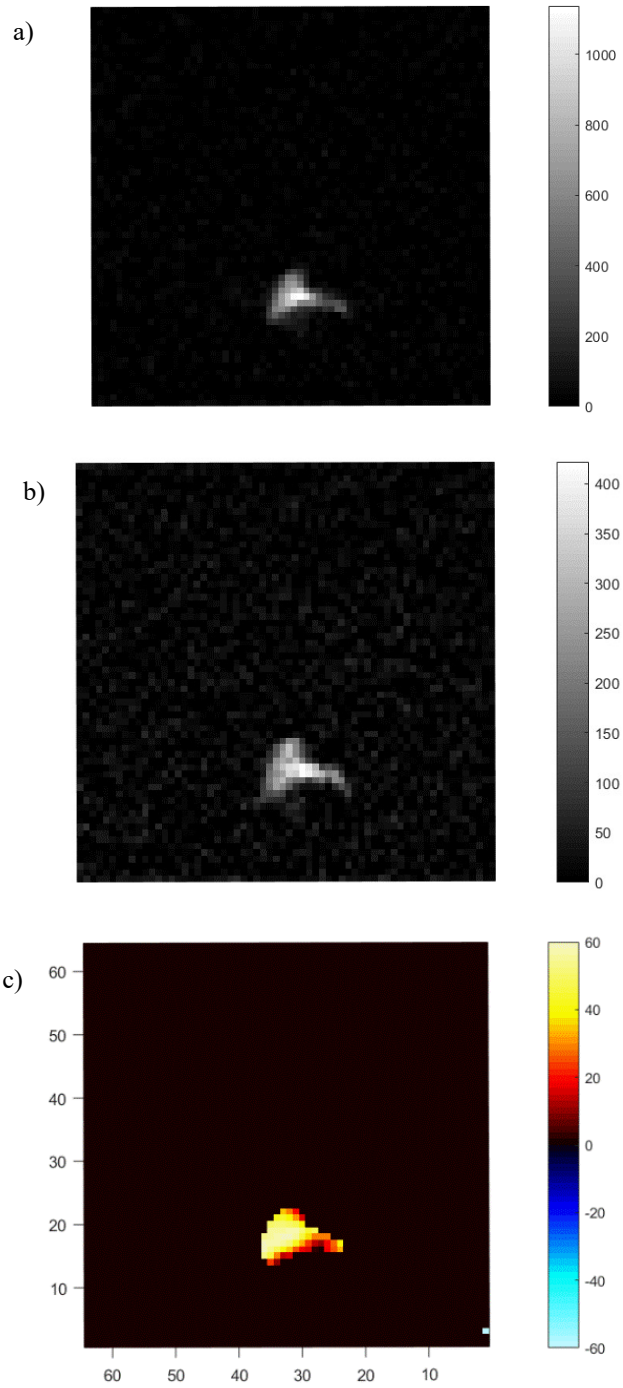

Figure B-40: a) Off-resonance image with SNR = 28.27; b) On-resonance image with SNR = 14.54. Both a) and b) were produced using a 32 x 30 3-lobe sinc pulse, TR = 5s, flip angle = 10°, and pulse angle =140°. Signal percent depletion is 48.6%. c) Saturation map of figure B-40 a) and b).

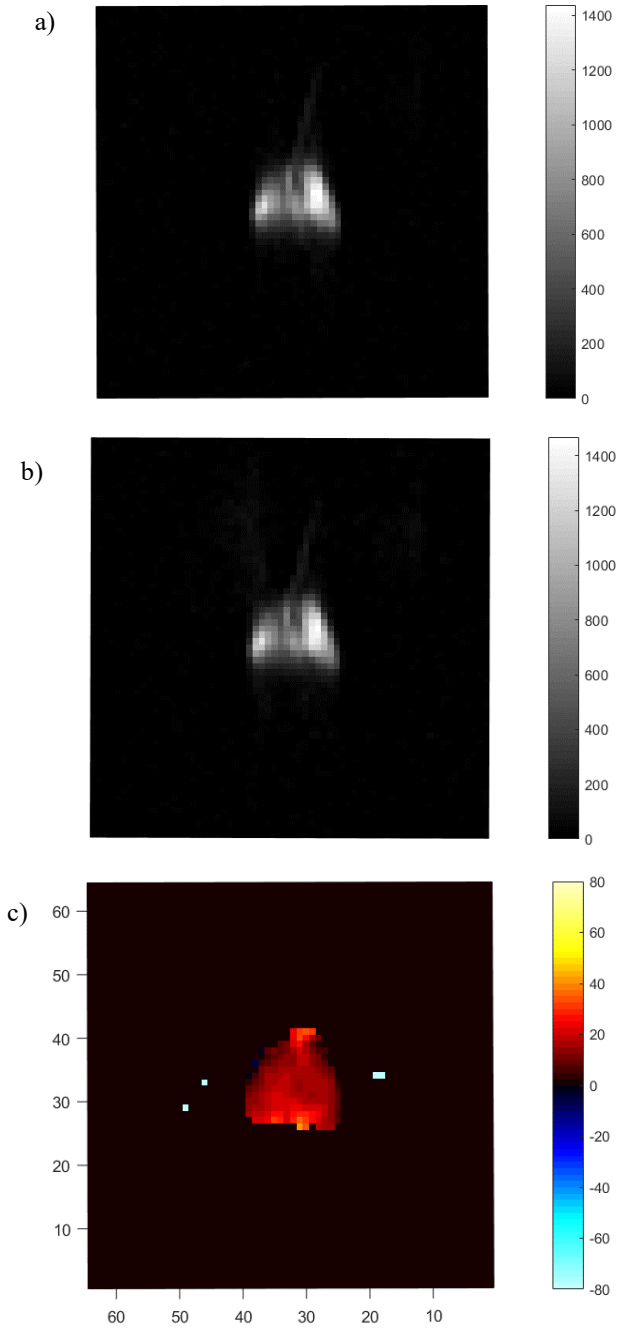

Figure B-41: a) Off-resonance image with SNR = 83.75; b) On-resonance image with SNR = 39.33. Both a) and b) were produced using a 16 x 30 3-lobe sinc pulse, TR = 5s, flip angle = 15°, and pulse angle =140°. Signal percent depletion is 53.0%. c) Saturation map of figure B-41 a) and b).

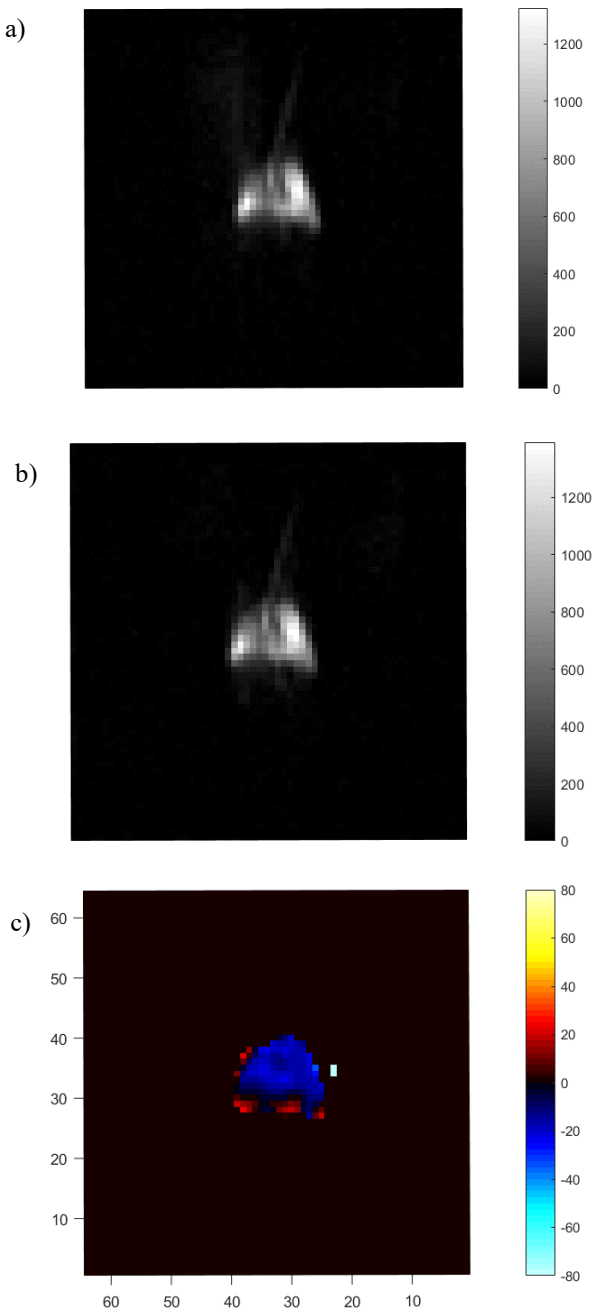

B-42: a) Off-resonance image with SNR = 75.88; b) On-resonance image with SNR = 74.73. Both a) and b) were produced using a 16 x 30 3-lobe sinc pulse, TR = 5s, flip angle = 15°, and pulse angle =140°. Signal percent depletion is 1.520%. c) Saturation map of figure B-42 a) and b).

Appendix C: Additional Proton BOLD fMRI Data

The ^{129}Xe fMRI data for the matching proton BOLD fMRI data within this appendix was unsuccessful, which did not show enhanced activity in the visual cortex. In addition, the ^{129}Xe fMRI data were omitted from this appendix because they were not part of my data analysis that I worked on. The ^{129}Xe fMRI was included in chapter 5 for completeness. The proton BOLD fMRI data in appendix C did not show stimulation within the visual cortex in the brains of healthy volunteers.

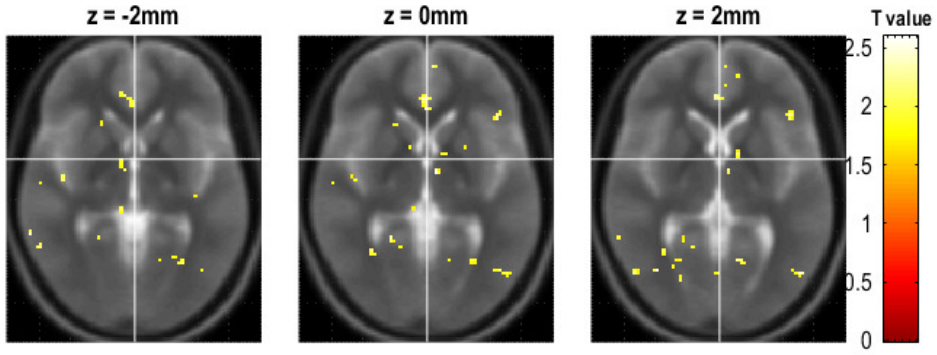

Figure C-1: Three proton, BOLD fMRI slices, which do not show signal enhancement in the visual cortex.

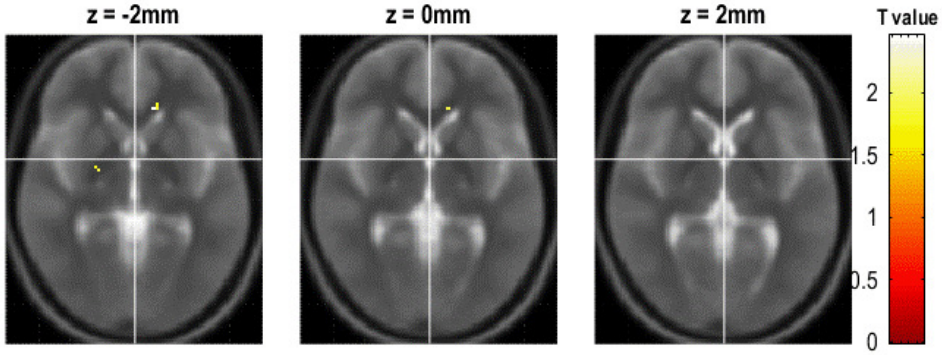

Figure C-2: Three proton, BOLD fMRI slices, which show no signal enhancement anywhere in the brain.

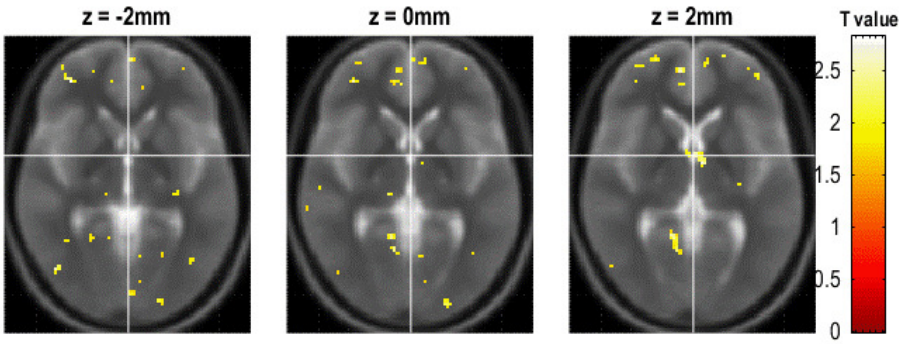

Figure C-3: Three proton, BOLD fMRI slices, which only show a very small amount of signal within the visual cortex of another healthy volunteer.

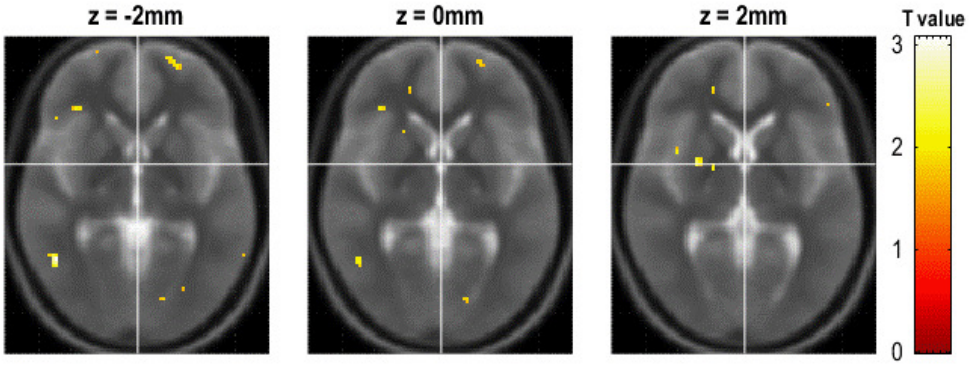

Figure C-4: Three proton, BOLD fMRI slices, which only show a very small amount of signal within the visual cortex of another healthy volunteer.

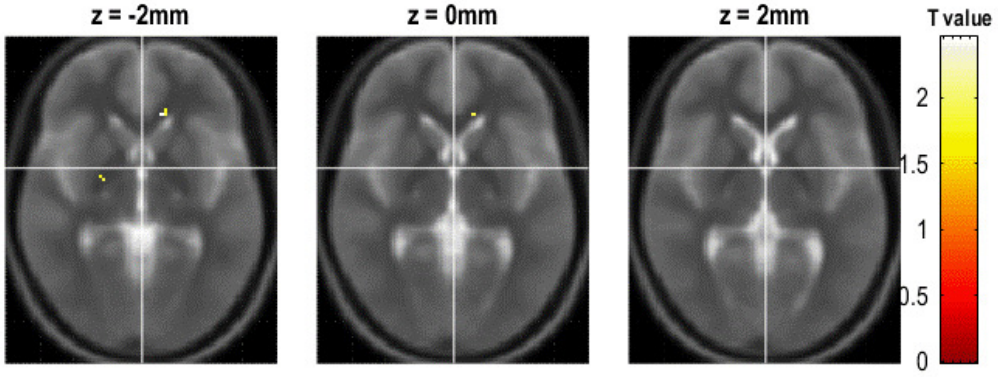

Figure C-5: Three proton, BOLD fMRI slices of a healthy volunteers, which show no signal enhancement anywhere in the brain.

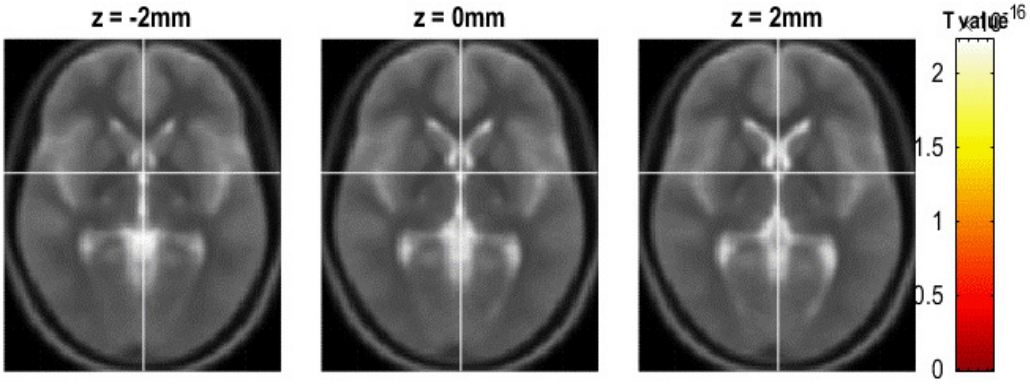

Figure C-6: Three proton, BOLD fMRI slices, which do not show signal enhancement anywhere in the brain.